NASA/TM—1998-206637

Design and Performance Calculations of a Propeller for Very High Altitude Flight

L. Danielle Koch
Lewis Research Center, Cleveland, Ohio

National Aeronautics and
Space Administration

Lewis Research Center

February 1998

Available from

NASA Center for Aerospace Information
800 Elkridge Landing Road
Linthicum Heights, MD 21090-2934
Price Code: A07

National Technical Information Service
5287 Port Royal Road
Springfield, VA 22100
Price Code: A07

DESIGN AND PERFORMANCE CALCULATIONS OF A PROPELLER FOR VERY HIGH ALTITUDE FLIGHT

by

L. DANIELLE KOCH

Submitted in partial fulfillment of the requirements

for the degree of Masters of Science in Engineering

Thesis Advisor: Dr. Eli Reshotko

Department of Mechanical and Aerospace Engineering

CASE WESTERN RESERVE UNIVERSITY

DESIGN AND PERFORMANCE CALCULATIONS OF A PROPELLER FOR VERH HIGH ALTITUDE FLIGHT

by

L. DANIELLE KOCH

ABSTRACT

Reported here is a design study of a propeller for a vehicle capable of subsonic flight in Earth's stratosphere. All propellers presented were required to absorb 63.4 kW (85 hp) at 25.9 km (85,000 ft) while aircraft cruise velocity was maintained at Mach 0.40. To produce the final design, classic momentum and blade-element theories were combined with two and three-dimensional results from the Advanced Ducted Propfan Analysis Code (ADPAC), a numerical Navier-Stokes analysis code.

The Eppler 387 airfoil was used for each of the constant section propeller designs compared. Experimental data from the Langley Low-Turbulence Pressure Tunnel was used in the strip theory design and analysis programs written. The experimental data was also used to validate ADPAC at a Reynolds numbers of 60,000 and a Mach number of 0.20. Experimental and calculated surface pressure coefficients are compared for a range of angles of attack.

Since low Reynolds number transonic experimental data was unavailable, ADPAC was used to generate two-dimensional section performance predictions for Reynolds numbers of 60,000 and 100,000 and Mach numbers ranging from 0.45 to

0.75. Surface pressure coefficients are presented for selected angles of attack, in addition to the variation of lift and drag coefficients at each flow condition.

A three-dimensional model of the final design was made which ADPAC used to calculated propeller performance. ADPAC performance predictions were compared with strip-theory calculations at design point. Propeller efficiency predicted by ADPAC was within 1.5% of that calculated by strip theory methods, although ADPAC predictions of thrust, power, and torque coefficients were approximately 5% lower than the strip theory results. Simplifying assumptions made in the strip theory account for the differences seen.

ACKNOWLEDGEMENTS

How fortunate I am to have so many blessings to count! For their patience and guidance, I would like to thank Dr. Eli Reshotko and Dr. Christopher Miller. It takes special skill to be a teacher, and I am sincerely grateful to have been able to learn by your examples.

For their unfailing enthusiasm, I would like to thank Dave Bents and Tony Colozza of the ERAST team. It has been a long and bumpy road, and your optimism has really made a difference.

For making financial support available, I would like to thank NASA, Jeff Haas, Wayne Thomas, and Chuck Mehalic. While slightly beyond the boundaries of my normal assigned duties, I believe that I am a better engineer because of the experience gained through this thesis work.

CONTENTS

NOMENCLATURE

a	=	speed of sound
c	=	chord
Cd	=	drag coefficient = D/(qS)
Cl	=	lift coefficient = L/(qS)
Cp	=	pressure coefficient= $\frac{2}{(\gamma)M_\infty{}^2}\left(\left(\frac{2+(\gamma-1)M_\infty{}^2}{2+(\gamma-1)M^2}\right)^{\frac{\gamma}{(\gamma-1)}}-1\right)$
CP	=	power coefficient = $P/(\rho n^3 d^5)$
CQ	=	torque coefficient = $Q/(\rho n^2 d^5)$
CT	=	thrust coefficient = $T/(\rho n^2 d^4)$
d	=	diameter
D	=	drag
e	=	specific stored energy
J	=	advance ratio = V/(nd)
L	=	lift
M	=	Mach number = V/a
n	=	rotational speed
P	=	power
q	=	dynamic pressure = $0.5\rho V^2$
Q	=	torque

r	=	radius
Rtip	=	tip radius
S	=	wing area
T	=	thrust
u	=	x component of velocity
v	=	y component of velocity
V	=	freestream velocity
w	=	z component of velocity
x	=	chordwise distance
y	=	distance from airfoil surface
y^+	=	dimensionless distance = $(y/\nu)(\tau_{wall}/\rho)^{0.5}$
α	=	angle of attack
β	=	twist angle
η	=	efficiency = (CT*J)/CP
μ	=	dynamic viscosity
ν	=	kinematic viscosity
ρ	=	density
τ_{wall}	=	shear stress at the wall

CHAPTER 1--INTRODUCTION

Background

Concern for the environment and determination to overcome a new challenge can make very high altitude subsonic flight possible. Driven by the needs of the atmospheric research community, a remotely piloted vehicle capable of flying subsonically in the stratosphere is being developed by a consortium of federal, industrial, and academic partners under NASA's Environmental Research Aircraft and Sensor Technology (ERAST) program.

In-situ measurements at altitudes between 24.4 km (80,000 ft) and 30.5 km (100,000 ft) are needed to further our understanding of the dynamics and chemistry of Earth's atmosphere. These measurements would augment laboratory research, data from samples of the lower stratosphere taken by the ER-2 aircraft, and measurements from satellites and balloons. A better fundamental understanding of the atmosphere can help us to make more responsible decisions in the way we choose to live, work, and travel.

Undeniably, development of a suitable propulsion system is the most formidable challenge. Currently, there are no existing propulsion systems capable of meeting either the program's near term altitude goal of 25.3 km (83,000 ft) or ultimate goal of 30.5 km (100,000 ft). Studies summarized by the ERAST program's Leadership Team (Ref. 1) suggest that the near term goal may be met by either a modified gas turbine power plant or a turbocharged reciprocating combustion engine.

Non-airbreathing or hybrid systems are the most likely candidates for propelling an aircraft to the ultimate altitude goal.

For many of the conceptual aircraft being considered, power produced is transferred to thrust by a propeller. Presented here is an aerodynamic design study of a propeller to meet the near term ERAST vehicle requirements using the most readily available computational tools, design and analysis methods, and experimental data. Strip-theory design and analysis methods are used with two and three-dimensional results from the Advanced Ducted Propfan Analysis Code-Version 7 (ADPAC), a numerical Navier-Stokes analysis code, to develop a propeller design.

Propeller Requirements

Design is an iterative process. It begins with a carefully chosen set of requirements that are based on the best results of any conceptual or experimental studies done. The propeller requirements in Table 1 have been derived from the Near-Term ERAST mission requirements shown in Table 2 and the expected propulsion system performance (Ref. 1).

Table 1. Propeller Requirements

Altitude	25.9 km (85,000 ft)
Power	63.4 kW (85 hp)
Maximum Relative Mach Number	0.80
Cruise Mach Number	0.40

Table 2. ERAST Mission Requirements

Mission	**Near-Term Goal (1998 - 2000)**	**Long-Term Goal (2000 +)**
Mission altitude	25.3 km (83,000 ft)	30.5 km (100,000 ft)
Operational Radius	1000 km (539 nmi)	4000 km (2160 nmi)
Payload weight	150 kg (330 lbm)	225 kg (496 lbm)
Payload accommodations	Access to undisturbed free stream	
Airspeed range	$0.40 < M < 0.85$	
Operational Constraints	Can operate in moderate turbulence Operation in ambient air temperatures to -100° C	
Crosswind Capability	Takeoff and landing in moderate crosswinds (minimum 15 knots)	
Deployment	To remote base of operations at airfields worldwide	

Overview of the Design and Analysis Methods Used

Having a firm set of requirements, the designer must then decide upon a method to meet them. The steps taken to arrive at the final design presented in this thesis are briefly described below. Each step will be discussed in depth in the chapters to follow.

Step 1. The Eppler 387 airfoil was chosen for the constant section propeller blade. While this airfoil was considerably thicker than those typically used for propeller sections, it was selected because it was known to have good performance at low Reynolds numbers. Experimental lift and drag data that could be used in the strip-theory programs, as well as the surface static pressure data that could be used to validate ADPAC was available for this airfoil.

Step 2. A grid study was conducted to determine an acceptable computational mesh density for the two-dimensional ADPAC performance calculations of the Eppler 387 airfoil. Having identified an appropriate mesh, ADPAC was validated by comparing calculated surface pressure coefficients to experimental pressure coefficients for a range of angles of attack.

Step 3. A strip-theory design program was written based on the procedures described by Adkins and Liebeck (Ref. 2). The low Reynolds number, low Mach number

experimental data from the Eppler 387 were incorporated into the program and a series of propellers were designed.

Step 4. The ADPAC code was used to calculate two-dimensional airfoil section performance for higher Mach numbers since no experimental data were found for this regime. The Reynolds number-Mach number combinations were identified by the results of Step 3.

Step 5. The results from Step 4 were incorporated into the strip-theory design and analysis codes. Another set of propellers was designed, examined and compared to arrive at the final geometry. Off design performance calculations were made for the final propeller design with the strip-theory analysis program.

Step 6. A three-dimensional computational mesh for the final propeller design was made, and ADPAC was used to make a three-dimensional performance prediction. The ADPAC result was compared to the strip-theory result at the design point.

CHAPTER 2

Selection of Airfoil and Airfoil Performance Data

The propeller designer's most critical decisions lie in the selection of blade airfoil sections and airfoil performance data. Accuracy of a propeller design or analysis conducted using strip theory methods will be compromised if any variation of airfoil performance with Reynolds number and Mach number is not taken into account. While the designer may be aided by modern numerical design and analysis programs, results cannot be used with any confidence until calculated performance is in good agreement with experimental data.

With the renewed interest in high altitude remotely piloted vehicles, sailplanes, and wind energy conversion, much research has been done to gain a better understanding of the behavior of steady and unsteady, two and three dimensional subsonic flows at low Reynolds numbers. Low Reynolds numbers are those below 10^6, as defined by Mueller in Reference 3, since the unpredictiblity of the boundary layer and the effects of laminar separation and reattachment play an important role in this regime. Results of this research has led to the development of many computational tools to design and analyze airfoils in this regime. Even so, behavior of the laminar boundary layer is still not completely understood and measurement and modelling of the boundary layer over airfoils at low Reynolds numbers still presents a challenge (Ref. 3).

For subsonic flows, the laminar boundary layer over an airfoil at low Reynolds number has been observed to behave in three different patterns as reported in Reference 3. The laminar boundary layer may either transition naturally to a turbulent boundary layer, may fully separate from the airfoil surface, or may separate and reattach to the airfoil surface forming a laminar separation bubble.

Performance is best if the laminar boundary layer naturally transitions to a turbulent boundary layer before reaching the adverse pressure gradient. With increased energy, the turbulent boundary layer is able to withstand the adverse pressure gradient and the flow will be able to stay attached to the airfoil surface much longer yielding good lift and drag characteristics.

Full separation results in a severe performance degradation. The airfoil will stall at high angles of attack when the laminar boundary layer completely separates from the airfoil surface near the leading edge. Full separation can also occur at lower angles of attack if the laminar boundary layer is unable to overcome an adverse pressure gradient.

A separation bubble is formed when the laminar boundary layer, unable to overcome an adverse pressure gradient, separates but then reattaches to the airfoil surface after transitioning to turbulent. Typically, the laminar shear layer will begin transitioning immediately downstream of the separation point. The separated turbulent shear layer will then grow quickly entraining flow from the free stream until it reattaches to the airfoil surface. Within the bubble is a region of slow moving

reversed flow with the center of the vortex lying near the reattachment point. The airfoil surface pressure remains nearly constant across the bubble region and increases rapidly near the point where the flow reattaches.

The length of the separation bubble depends upon how rapidly the laminar shear layer is able to transition. Generally, separation bubbles will lengthen as chord Reynolds number is decreased. While not always clearly seen, increasing free stream turbulence levels, airfoil surface roughness, and employing boundary layer tripping devices have usually been effective in shortening the laminar separation bubble and improving airfoil performance (Ref. 3). Increasing the adverse pressure gradient has also been seen to reduce the length of the separation bubble by reducing the time needed for transition (Ref. 4).

Preliminary studies showed that at an altitude of 25.9 km (85,000 ft) propeller blade Reynolds numbers could vary from 50,000 to 200,000 while relative free-stream Mach numbers could range from 0.40 to the design limit of 0.80. No experimental data was found for this transonic low Reynolds number regime. Experimental results were found for an Eppler 387 airfoil that had been tested at the Langley Low-Turbulence Pressure Tunnel (LTPT) at Reynolds numbers of 60,000 to 460,000 and a Mach number range of 0.03 to 0.13 (Ref. 5). Because of the high quality of the experimental data, and the availability of airfoil surface pressure, lift, and drag coefficients at each angle of attack, the Eppler 387 airfoil was chosen over other airfoils with known good performance at low Reynolds numbers for the

constant section propeller. This section is much thicker than the transonic airfoils normally chosen for propellers tip sections. The simplification of one airfoil for the entire blade was made for academic purposes only, simplifying programming and modelling.

The variation of the lift and drag coefficients for the Eppler 387 measured at the Langley LTPT for Reynolds numbers of 60,000, 100,000 and 200,000 are shown in Figures 1 and 2. At a Reynolds number of 60,000, laminar separation was not always observed to be followed by turbulent reattachment. This phenomenon can be seen in Figure 1, as the airfoil stalls around $\alpha = 3.00°$ and the boundary layer did not reattach until an angle of attack of 7.50°. In fact, both phenomena, separation with and without reattachment, were observed at an angle of attack of 4.00°. The measurement techniques used were not able to resolve the unsteady nature of the flow at this Reynolds number. This behavior may result from short separation bubbles bursting, although further experimentation would be needed to prove this. McGhee, Walker, and Millard observed no hysteresis loops for this airfoil in the Langley LTPT in a set of experiments designed to study hysteresis effects for Reynolds numbers from 60,000 to 300,000.

Figures 3 through 5 show the variation of pressure coefficients on the airfoil surface for Reynolds numbers ranging from 60,000 to 200,000 for an angle of attack of 8.00°. From these figures and others reported in Reference 5, surface pressure measurements and oil flow visualization techniques showed that the length of the

separation bubble decreased as Reynolds number was increased. Oil flow visualization indicated that the boundary layer naturally transitioned for a Reynolds number of 200,000 and $\alpha = 8.00°$.

The Eppler 387 has been tested in several other facilities and the data from the Langley Low-Turbulence Pressure Tunnel have been used to validate numerous airfoil design and analysis codes. Comparisons of these results shed light on the many challenges still faced. Reference 5 presents experimental results from tests of two dimensional models of the Eppler 387 in the Low Turbulence Wind Tunnel at Delft and the Model Wind Tunnel at Stuttgart. As reported in Reference 5 and seen again in Figures 6 through 11 , observations at Langley for a Reynolds number of 60,000 were confirmed in tests of an Eppler 387 section in the Low Turbulence Wind Tunnel at Delft, but not by tests in the Model Wind Tunnel at Stuttgart. Reasons for these discrepancies are still unknown but have been associated with differences in tunnel turbulence levels, model quality, model mounting configurations, and force measurement methods.

The Eppler-Somers code (Ref. 5) and Drela's XFOIL and ISES codes (Ref. 6, 7) are among the design and analysis codes that have been validated with the Eppler 387 data taken at Langley. The XFOIL and ISES codes use an inviscid/viscous interaction technique while the Eppler-Somers code couples complex mapping, potential flow and boundary layer techniques together to solve for the flow field around an airfoil. General agreement between the calculated and experimental

results was good for each of these codes, although agreement degraded as Reynolds number decreased. This degradation is inherent to the technique used since as Reynolds number decreases and the boundary layer thickens the interaction between the inviscid and viscous region gets stronger and the boundary layer approximations become less accurate (Ref. 8). At Reynolds numbers above 100,000 these codes are practical design tools because they can solve for an airfoil's performance quickly.

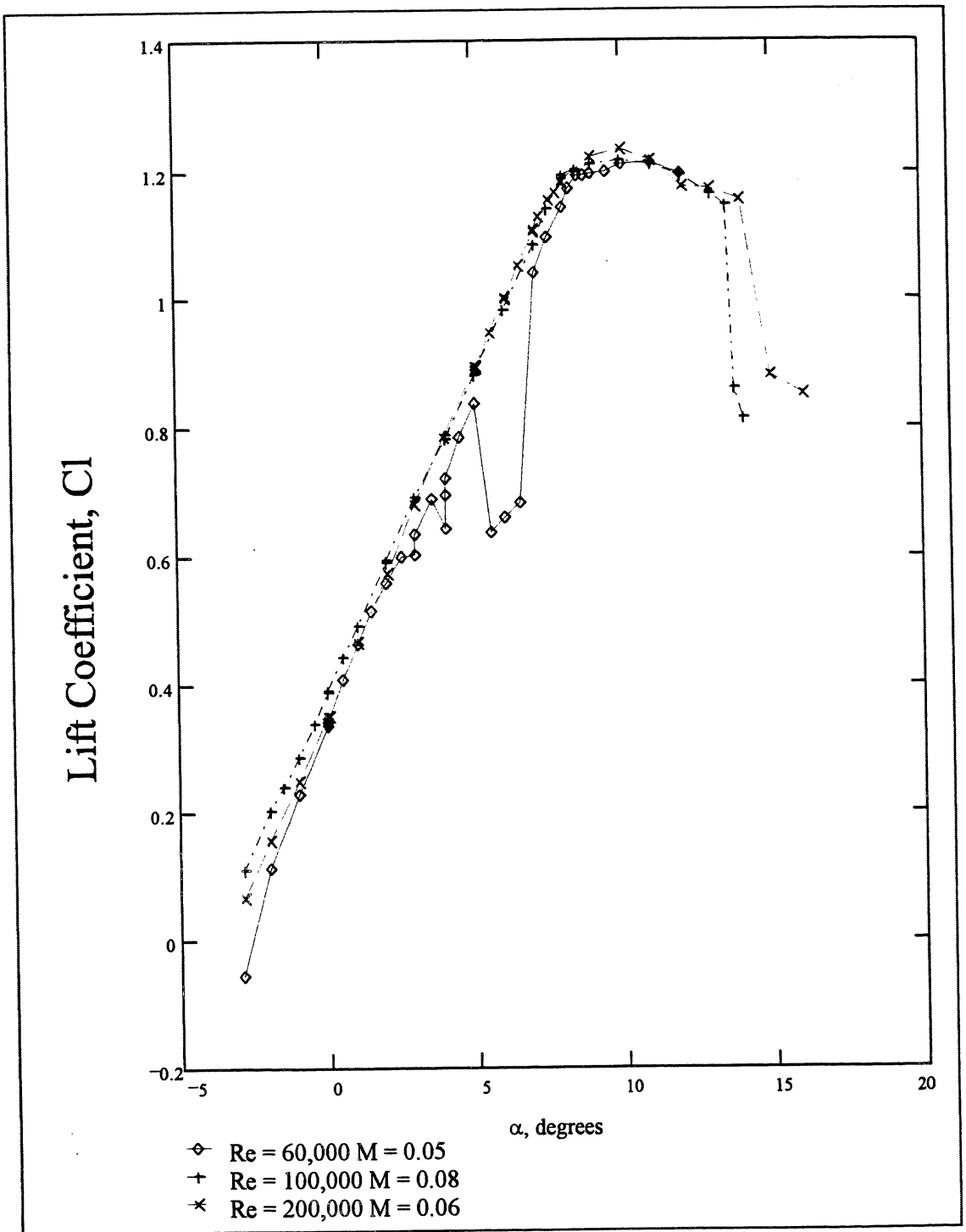

Figure 1: Variation of Lift Coefficient with Reynolds Number as Measured at the Langley Low-Turbulence Pressure Tunnel

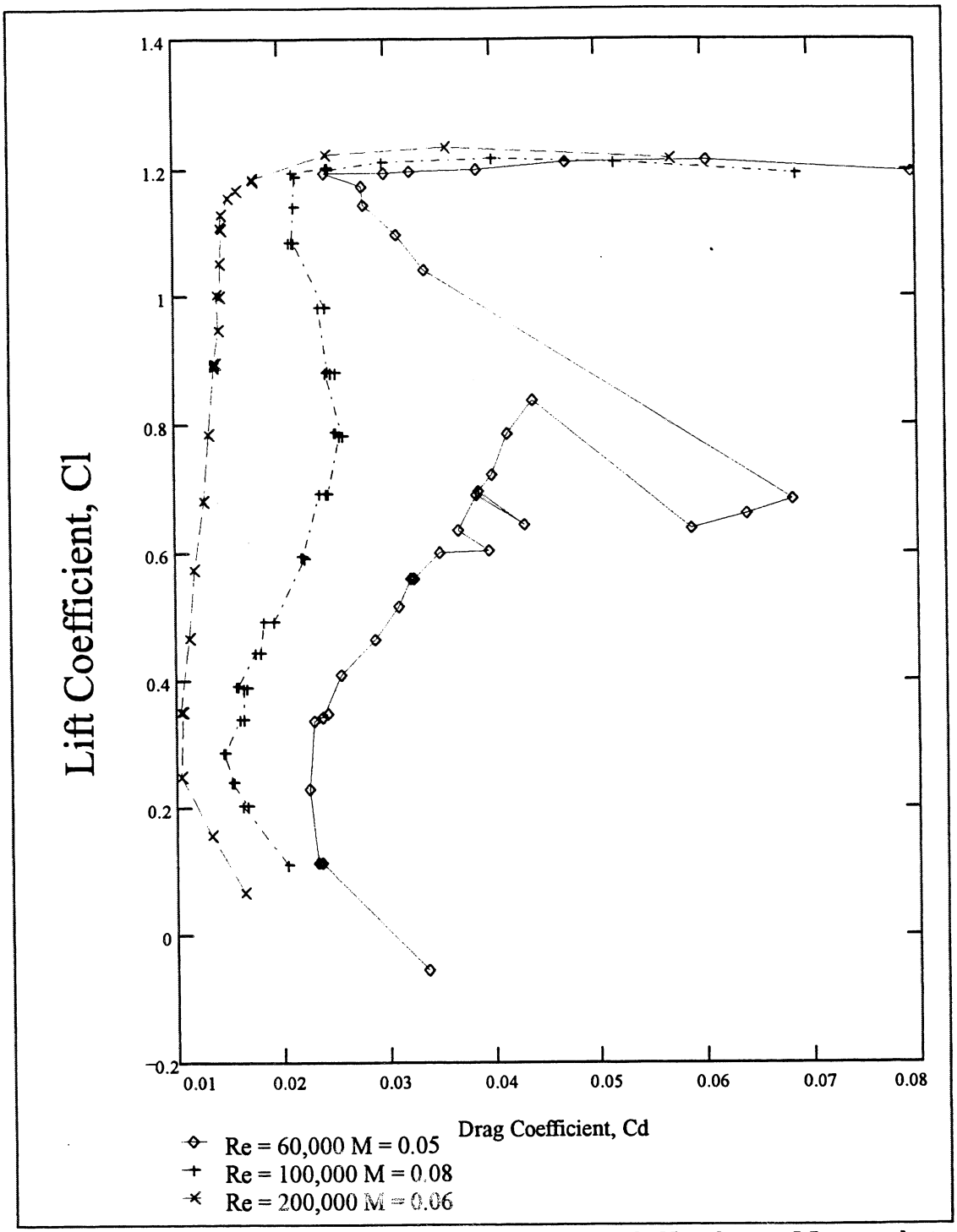

Figure 2: Variation of Drag Coefficient with Reynolds Number as Measured at the Langley Low-Turbulence Pressure Tunnel

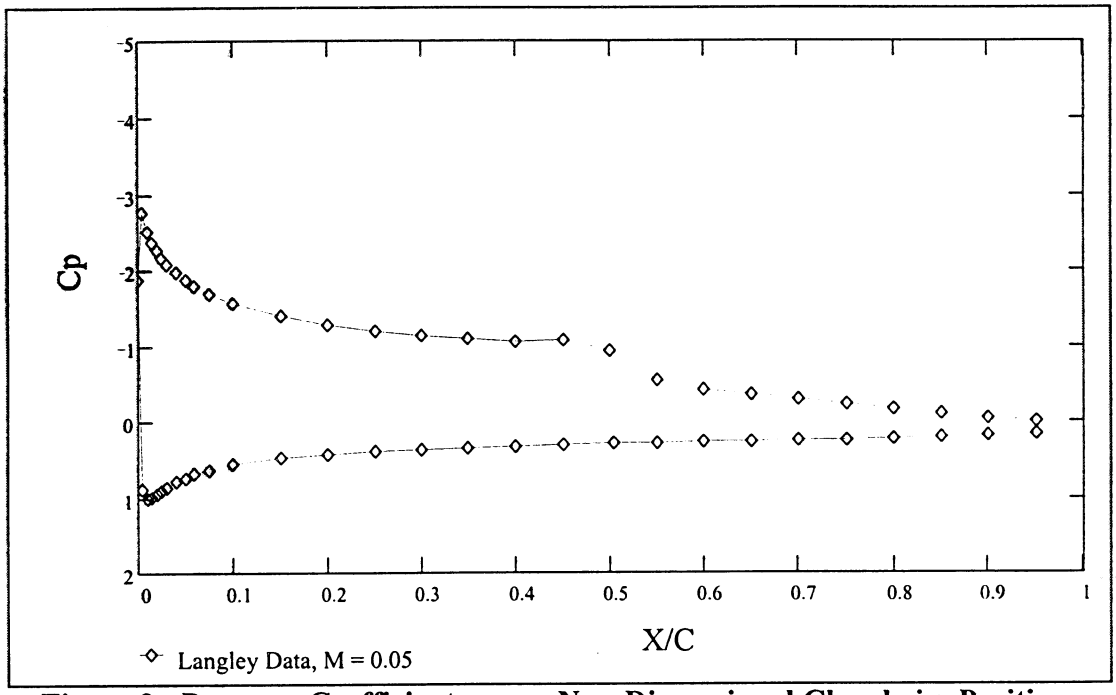

Figure 3: Pressure Coefficient versus Non-Dimensional Chordwise Position, Re = 60,000 and $\alpha = 8.01°$

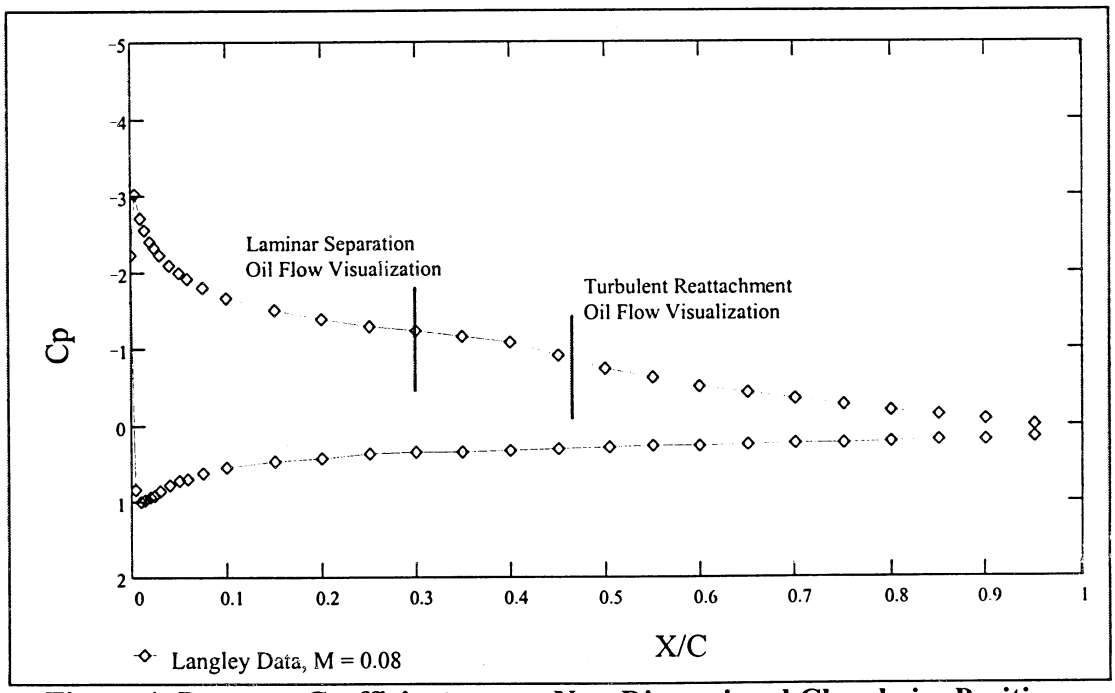

Figure 4: Pressure Coefficient versus Non-Dimensional Chordwise Position, Re = 100,000 and $\alpha = 8.00°$

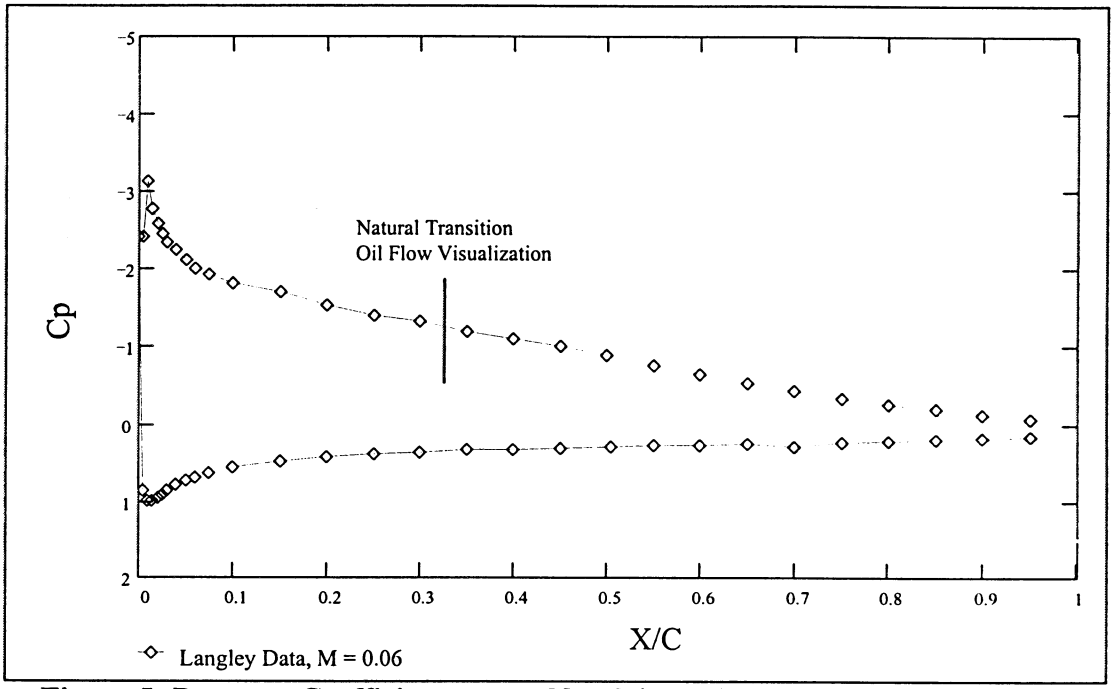

Figure 5: Pressure Coefficient versus Non-Dimensional Chordwise Position, Re = 200,000 and $\alpha = 8.00°$

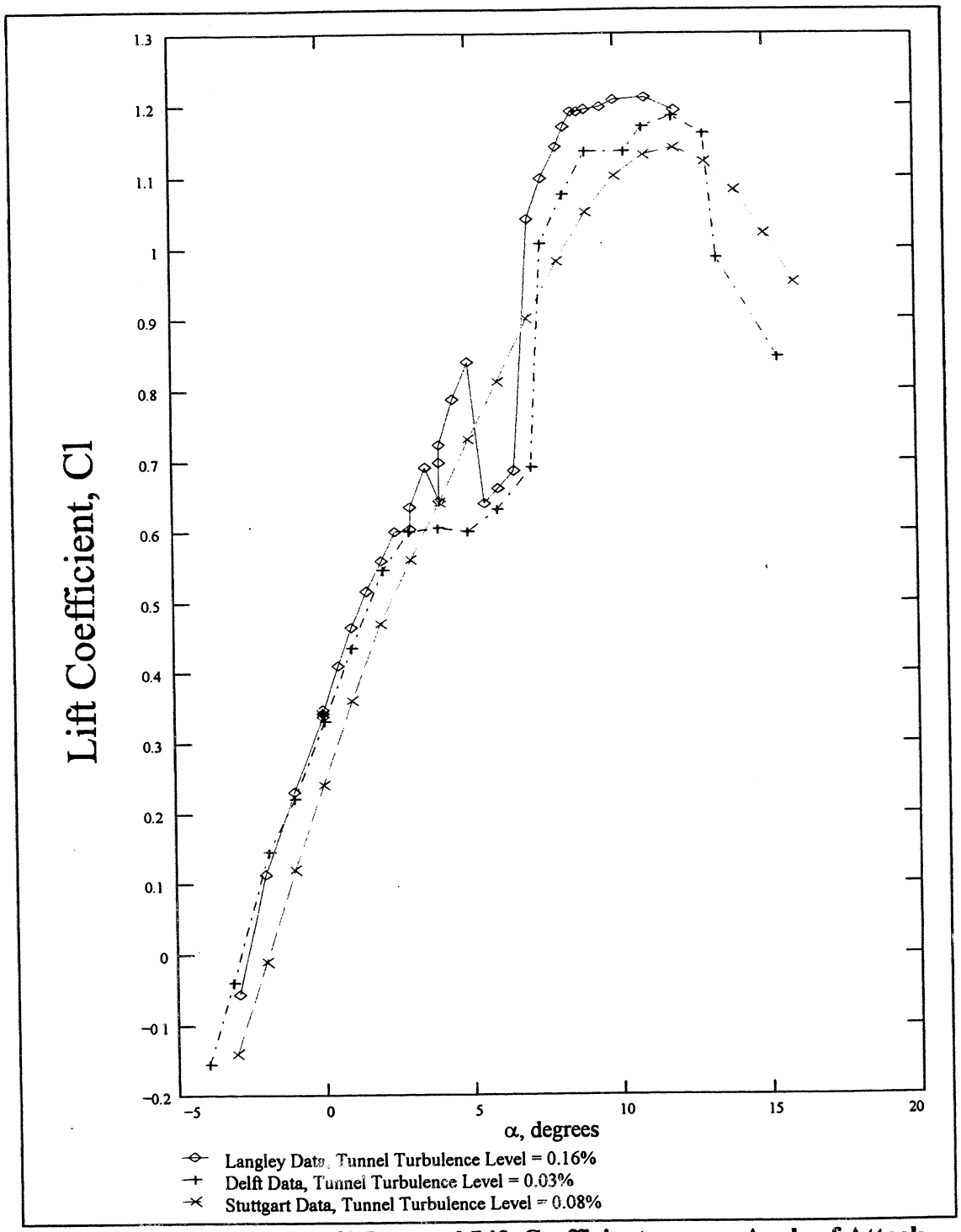

Figure 6: Comparison of Measured Lift Coefficients versus Angle of Attack from Tests at Langley, Delft, and Stuttgart at Re = 60,000

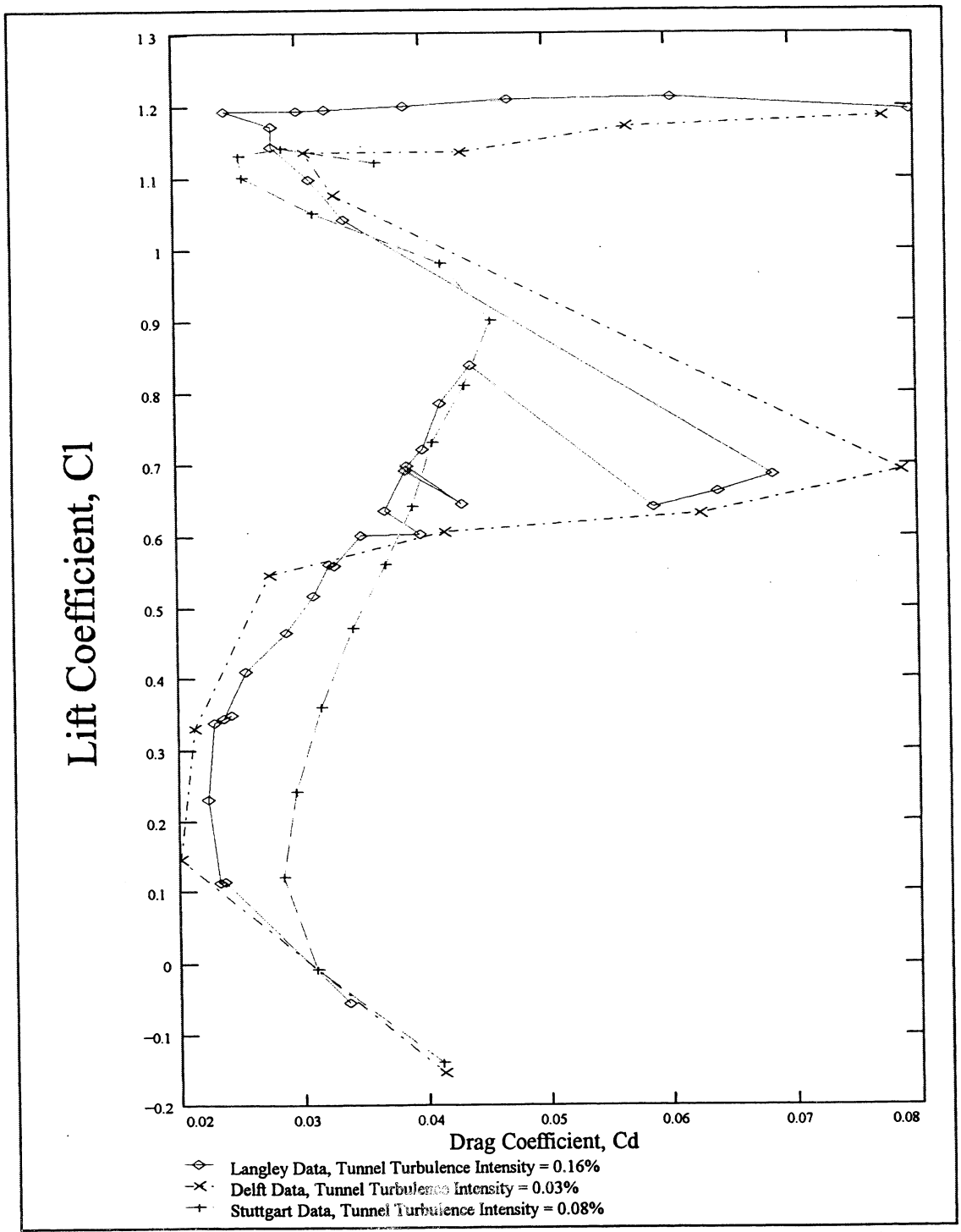

Figure 7: Comparison of Measured Lift Coefficients versus Drag Coefficients Tests at Langley, Delft, and Stuttgart at Re = 60,000

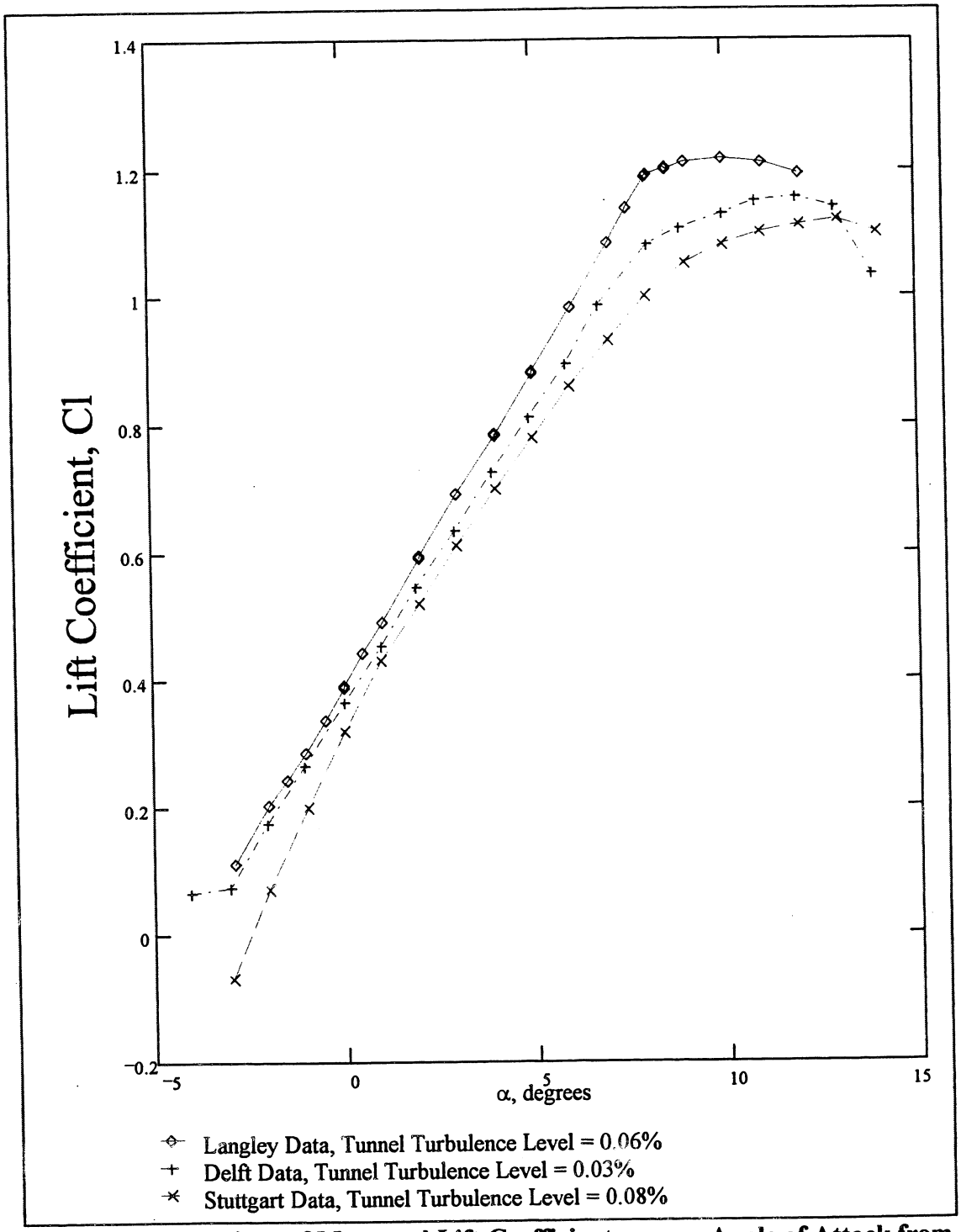

Figure 8: Comparison of Measured Lift Coefficients versus Angle of Attack from Tests at Langley, Delft, and Stuttgart at Re = 100,000

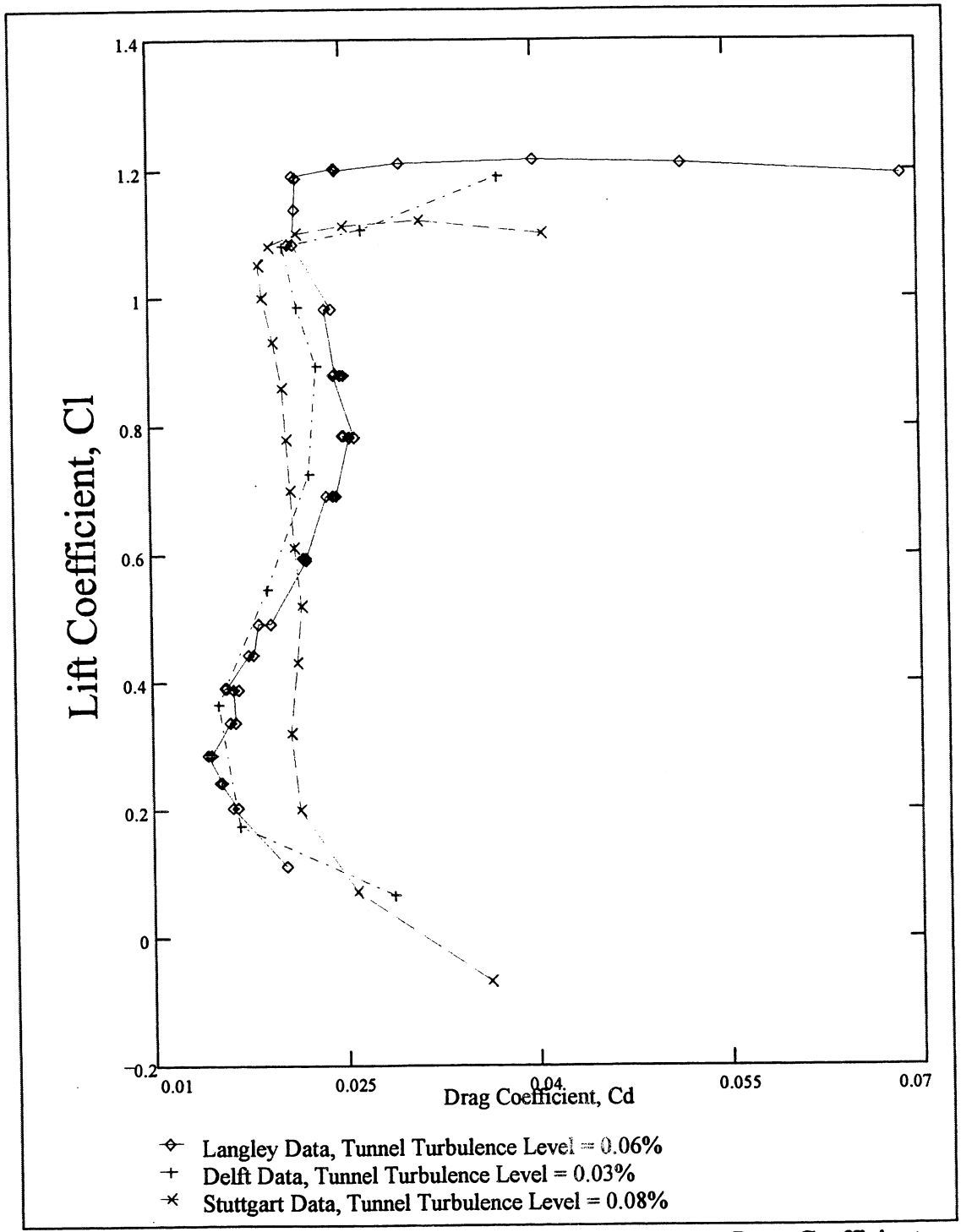

Figure 9: Comparison of Measured Lift Coefficients versus Drag Coefficients Tests at Langley, Delft, and Stuttgart at Re = 100,000

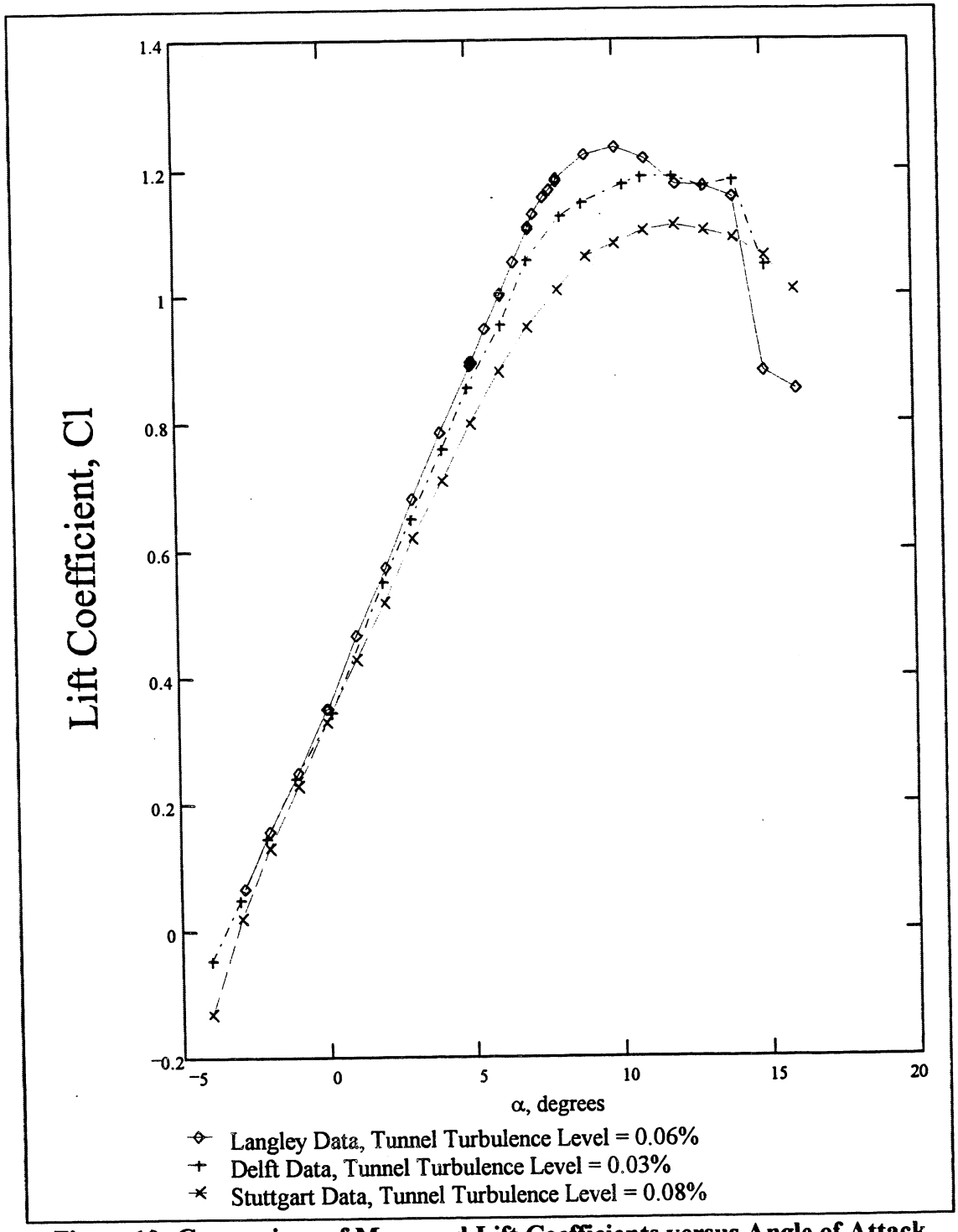

Figure 10: Comparison of Measured Lift Coefficients versus Angle of Attack from Tests at Langley, Delft, and Stuttgart at Re = 200,000

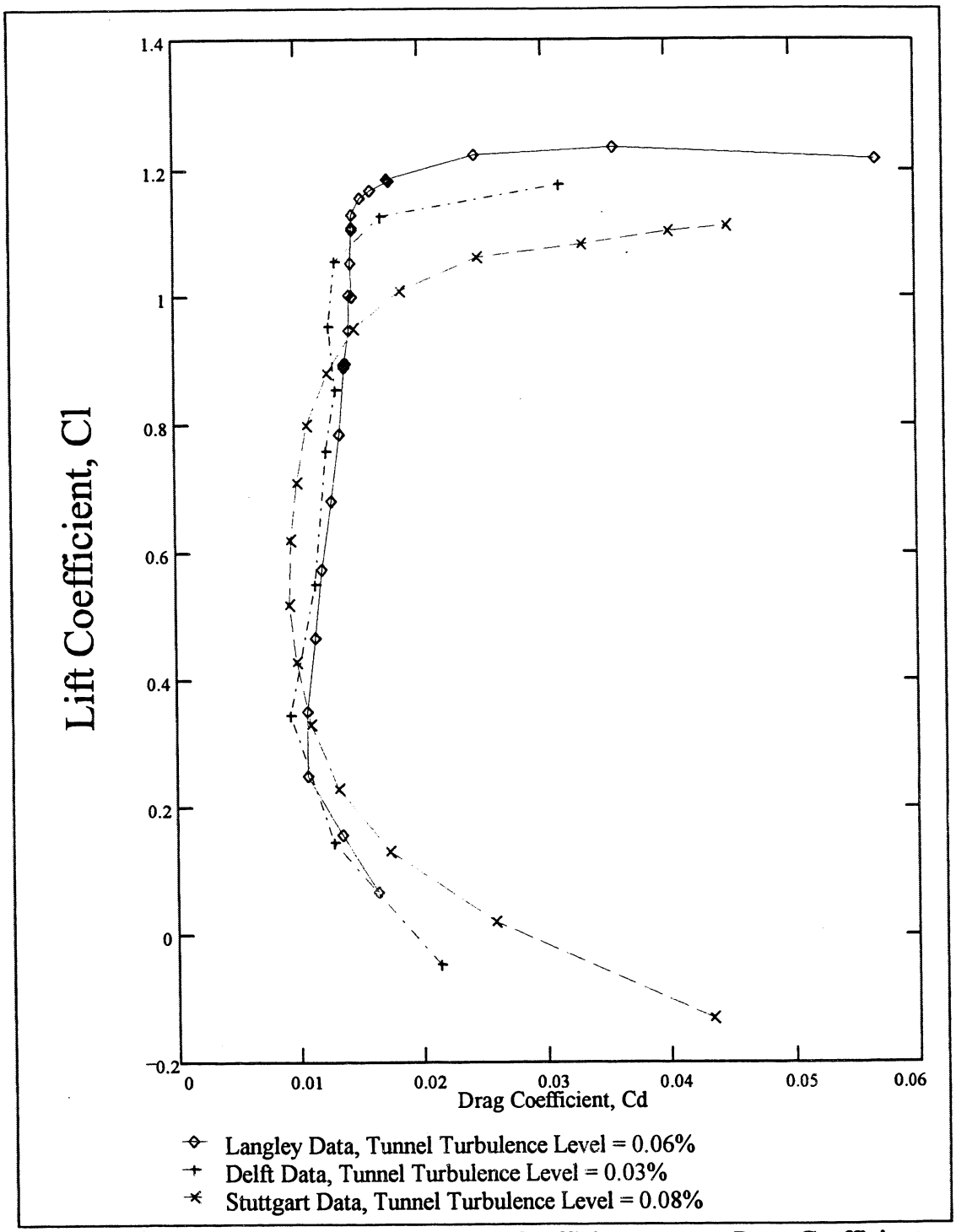

Figure 11: Comparison of Measured Lift Coefficients versus Drag Coefficients Tests at Langley, Delft, and Stuttgart at Re = 200,000

CHAPTER 3

Grid Study and ADPAC Validation

ADPAC is a three-dimensional time-marching Euler/Navier-Stokes analysis code that was originally developed to enable researchers to study the effects of compressor casing and endwall treatments (Ref. 9). The code is flexible enough to allow it to be used for analysis applications other than compressors. ADPAC gains much of its flexibility from the use of a multiple-block grid system. This feature is helpful when studying complicated geometries where it may not be possible to create a single structured grid of the flowfield. The multiple-block grid system allows one to create different grids for different areas of the flowfield. Special commands are provided to allow the different blocks to communicate with each other.

While the code had been validated for several turbomachinery and non-turbomachinery applications, ADPAC was unvalidated in the regime of interest for the ERAST propeller. The two-dimensional Eppler 387 experimental data from the Langley LTPT were used for this validation.

The first task at hand was to conduct a grid study. The purpose of the grid study is to identify the minimum computational mesh density for which a solution is independent of the number of grid points. For subsonic low Reynolds number flows, the grid must be sufficiently dense to resolve the boundary layer and any separation bubbles formed. Several 'C' grids of the flow field around the Eppler 387 geometry were created. Measured coordinates from the Langley pressure model of the airfoil

"Level 3" grid had 23,409 points, and the "Level 2" grid had 5,945 points. Each grid extended ten chordlengths upstream, downstream, above, and below the blade. The minimum acceptable number of points is desired to reduce computational time. Increasing the number of grid points past that of the Level 4 mesh was considered prohibitive. Views of the entire computational domain for the three two-dimensional grids can be found in Figures 12 through 14. Figures 15 through 17 show the portion of each mesh close to the airfoil surface and display the packing of grid points in the boundary layer region.

Two other files are required by ADPAC in order to run a calculation, an input file and a boundary data file. The input file contains parameters that allow one to scale the non-dimensional grid. In the boundary data file, one can specify the angle of attack and how the boundaries of the grid are to be treated. A combination of parameters within the input and boundary data files set the flow conditions. For all the two-dimensional airfoil performance calculations, the freestream Mach number was fixed on the horizontal straight sections of the outer boundary of the computational grid. Total temperature and total pressure were fixed on the inlet curved section of the outer boundary, and static pressure was fixed at the straight vertical exit plane. A no-slip condition was imposed on the blade surface, forcing the velocity at the blade to be zero. Because ADPAC is a compressible code, a freestream Mach number of 0.20 was set. The Mach numbers for the experimental data were generally below 0.10.

Each grid was used to calculate the flow at Reynolds numbers of 60,000, 100,000 and 200,000 while angle of attack was nominally 8.00°. Angle of attack was set to match that given by the experiment. Figures 18 through 20 show the calculated airfoil surface pressure coefficients plotted against the non-dimensionalized chordwise position and compared to the experimental data. Good agreement between the computations with the Level 4 grid and the experimental data was seen even at a Reynolds number of 60,000 which would have the longest separation bubble of all three cases.

Figure 21 shows a comparison of the calculated value of the lift coefficient as a function of the inverse number of mesh points for each Reynolds number. As Reynolds number increases, more grid lines must be packed towards the airfoil surface to resolve the thinner boundary layer. The dimensionless distance of the grid line away from the wall, y^+, is defined by Schlichting in Reference 10 as:

$$y^+ = \frac{y\sqrt{\frac{\tau_{wall}}{\rho}}}{\nu}$$

where y is the dimensional distance of the grid line away from the airfoil surface, τ_{wall} is the shear stress at the wall, ρ is the fluid density, and ν is the fluid kinematic viscosity. The values of y^+ for the first grid line of the Level 4 mesh at the quarter chord point are 0.0624, 0.0915, and 0.1537 for Reynolds numbers of 60,000, 100,000, and 200,000, respectively.

Accompanying each solution is a set of convergence plots. Figures 22 through 24 contain two convergence plots for each solution: the Root Mean Square (RMS) Error, and the Number of Separated points at each iteration. The Root Mean Square Error was defined to be the sum of the squares of the residuals of all the cells in the mesh, the residual being the sum of the changes of the five conservative variables, ρ, ρu, ρv, ρw, and ρe. The ADPAC definition of a separated point was a cell whose value for v_x was negative. Generally, for the low Mach number cases, the calculation was run until the number of separated points seemed to be constant and the residuals were reduced by at least three orders of magnitude.

The Level 4 grid was then used for a series of calculations at a Reynolds number of 60,000 and angles of attack ranging from -2.94° to 12.00°. The Level 4 grid was chosen because of the good agreement between the surface pressures calculated by ADPAC and the experimental data at a Reynolds number of 60,000 (Fig. 18). Lift coefficients were calculated for each angle of attack and can be seen compared to the Langley results in Figure 25. Pressure coefficient distributions are presented in Figures 26 through 31 for each of the colored points in Figure 25. Figures 32 through 37 are the corresponding convergence histories for each of the selected ADPAC calculations. Since the viscous drag result was unavailable from ADPAC, it was estimated by calculating skin friction drag on both sides of a flat plate drag (Ref. 10):

$$Cd = \frac{1.328}{\sqrt{\mathrm{Re}}}$$

The total of the viscous plus pressure drag coefficients were then plotted against the Langley data and are shown in Figure 38.

There was generally good agreement between the ADPAC calculated values and the experimental values. Examination of the plots shows that ADPAC, like many other numerical analysis codes, was unable to predict the laminar stall that was measured at Langley at angles of attack from 3.00° to 7.50°. The marked increase in measured drag in this region was also unpredicted by this version of ADPAC. For angles of attack less than 8.01° there is not good agreement between the calculated and experimental data near the trailing edge with ADPAC predicting recompression farther upstream than was seen in experiments in the Langley LTPT (Fig. 26 - 29). Agreement between the ADPAC prediction and the experimental results at the trailing edge improves at angles of attack of 8.01° and greater (Fig. 30 - 31).

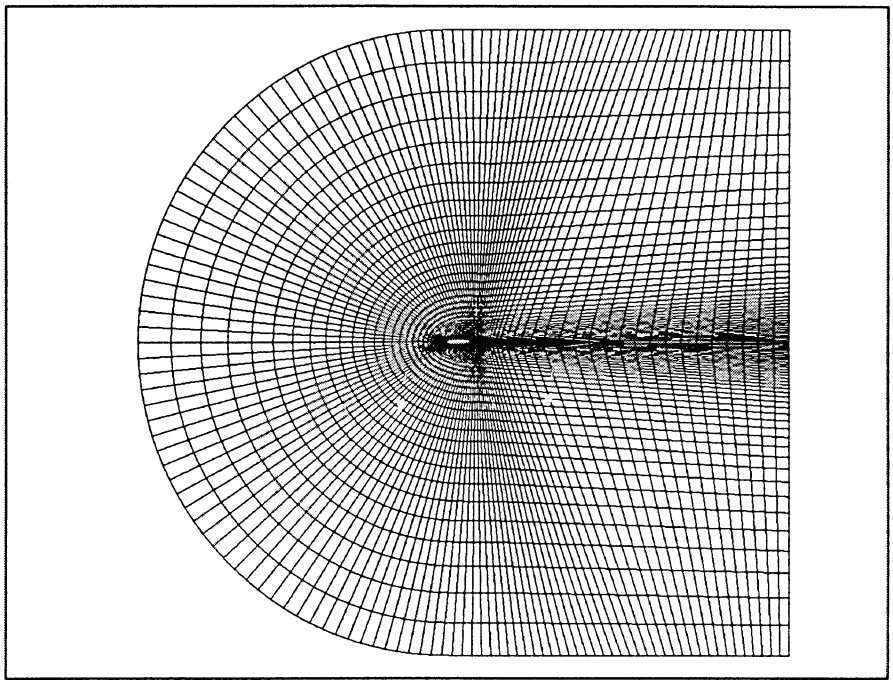

Figure 12: Entire Level 2 Computational Mesh of the Eppler 387 Airfoil

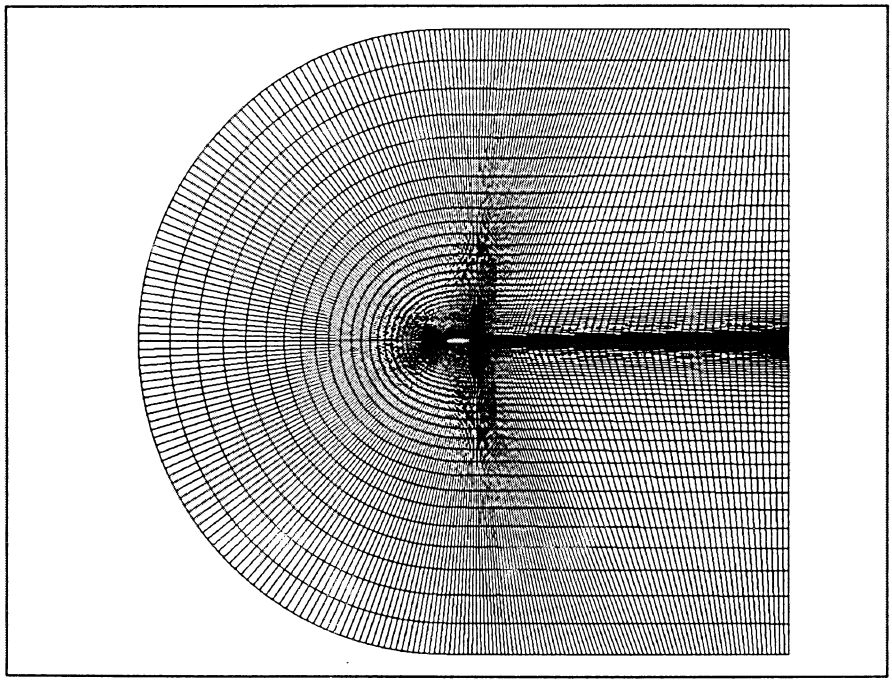

Figure 13: Entire Level 3 Computational Mesh for the Eppler 387 Airfoil

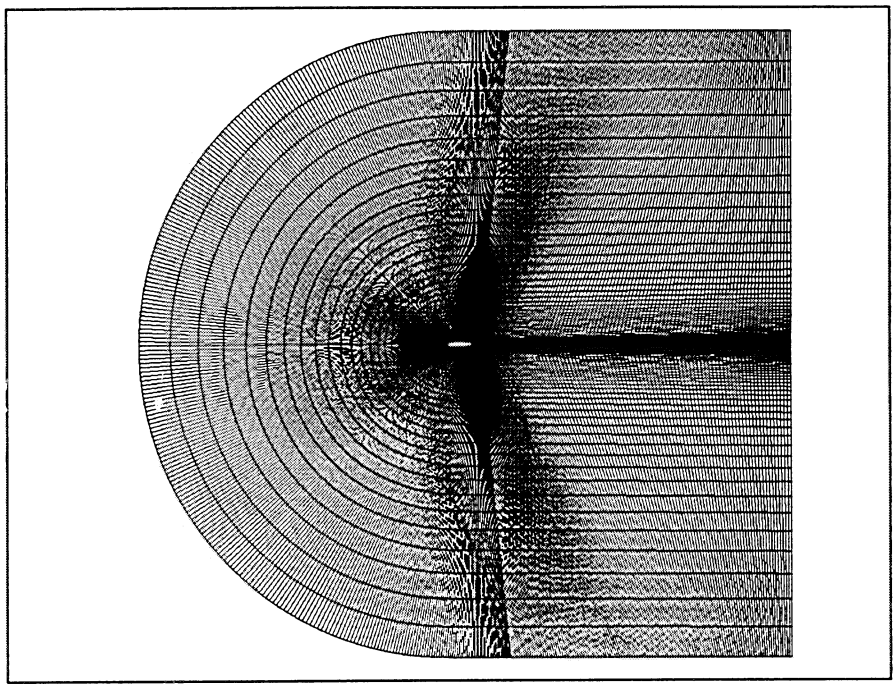

Figure 14: Entire Level 4 Computational Mesh for the Eppler 387 Airfoil

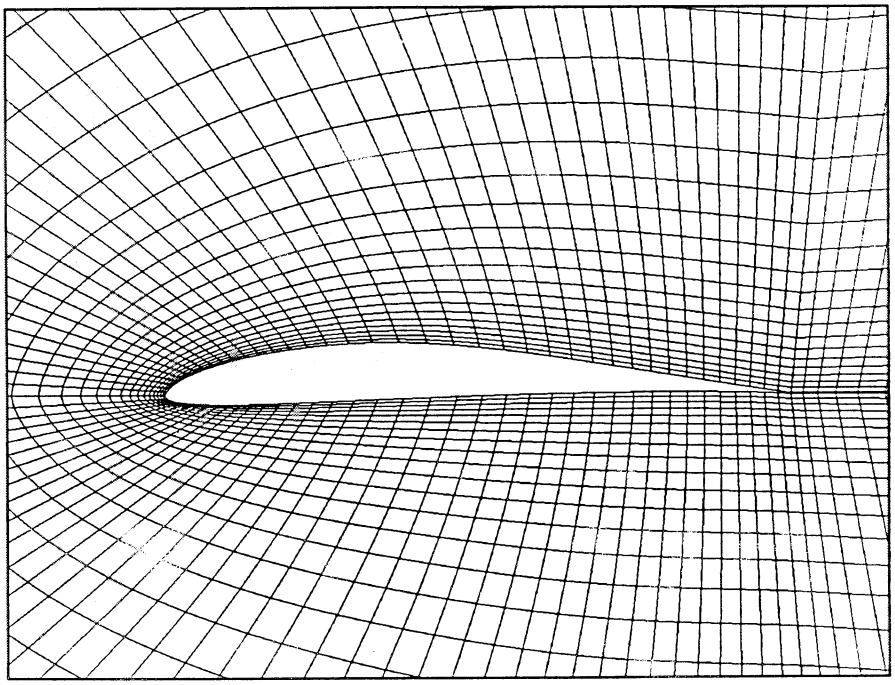

Figure 15: Portion of Level 2 Mesh Close to the Airfoil Surface

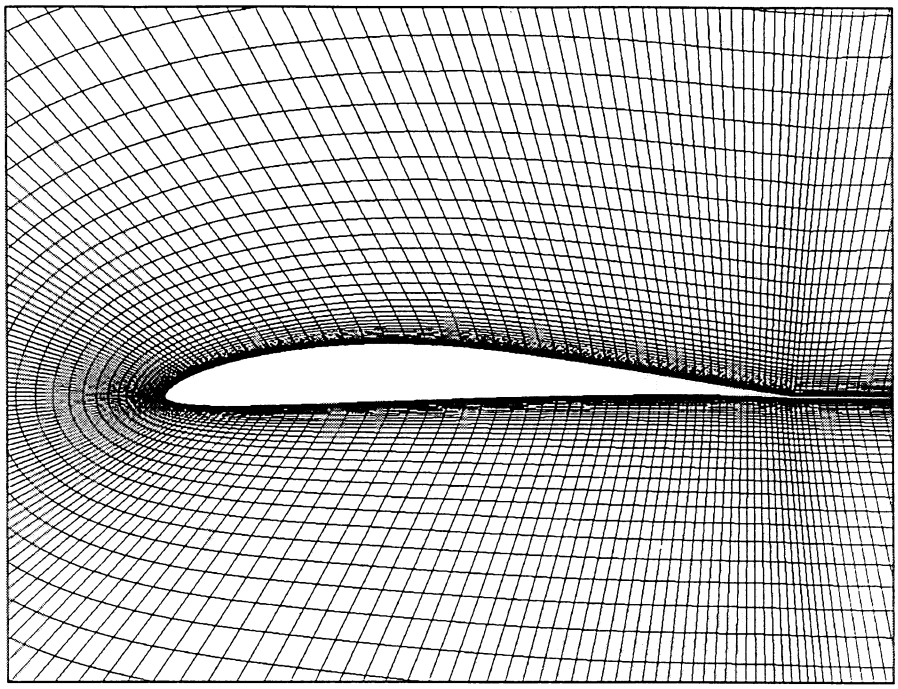

Figure 16: Portion of Level 3 Mesh Close to the Airfoil Surface

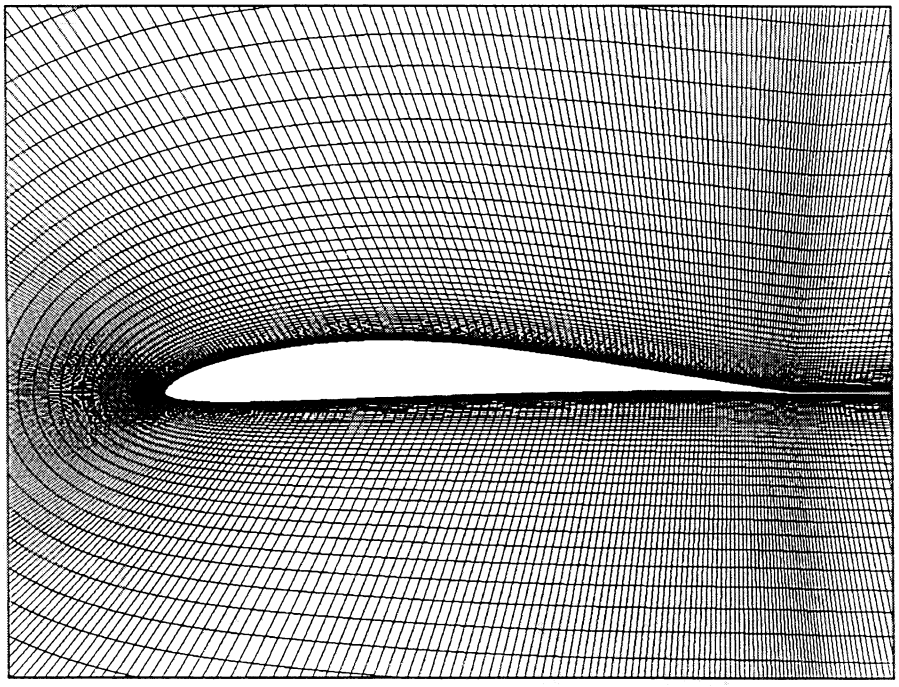

Figure 17: Portion of Level 4 Computational Mesh Close to the Airfoil Surface

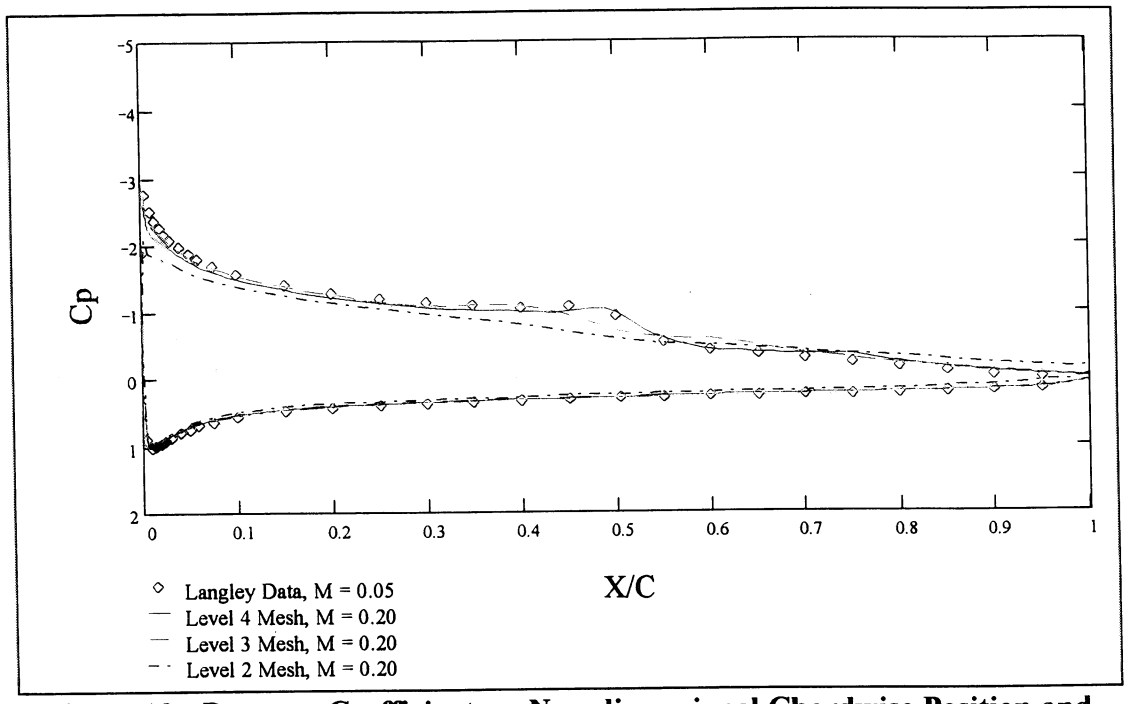

Figure 18: Pressure Coefficient vs. Non-dimensional Chordwise Position and Different Computational Mesh Densities, Re = 60,000 and α = 8.01°

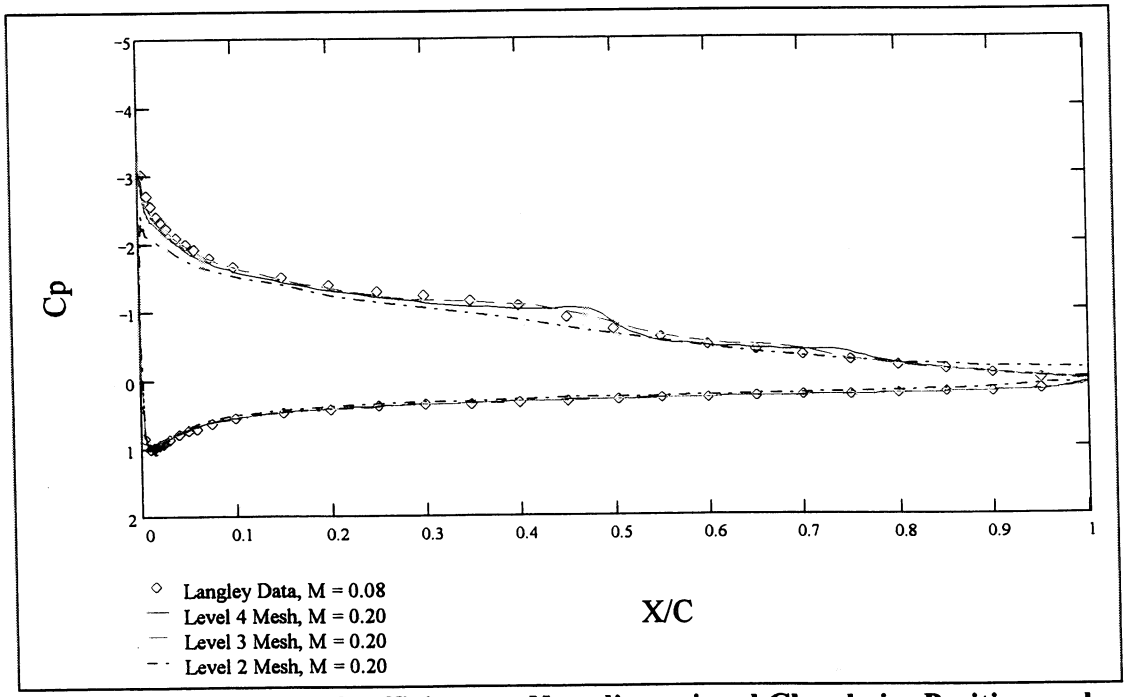

Figure 19: Pressure Coefficient vs. Non-dimensional Chordwise Position and Different Computational Mesh Densities, Re = 100,000 and α = 8.00°

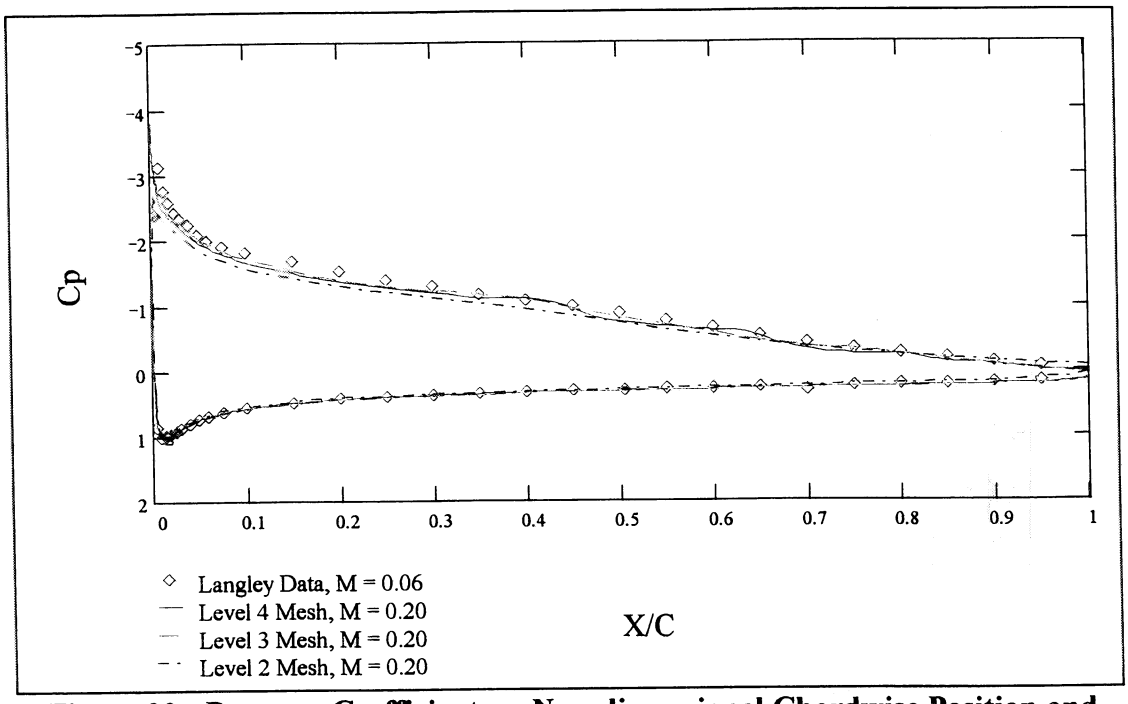

Figure 20: Pressure Coefficient vs. Non-dimensional Chordwise Position and Different Computational Mesh Densities, Re = 200,000 and α= 8.00°

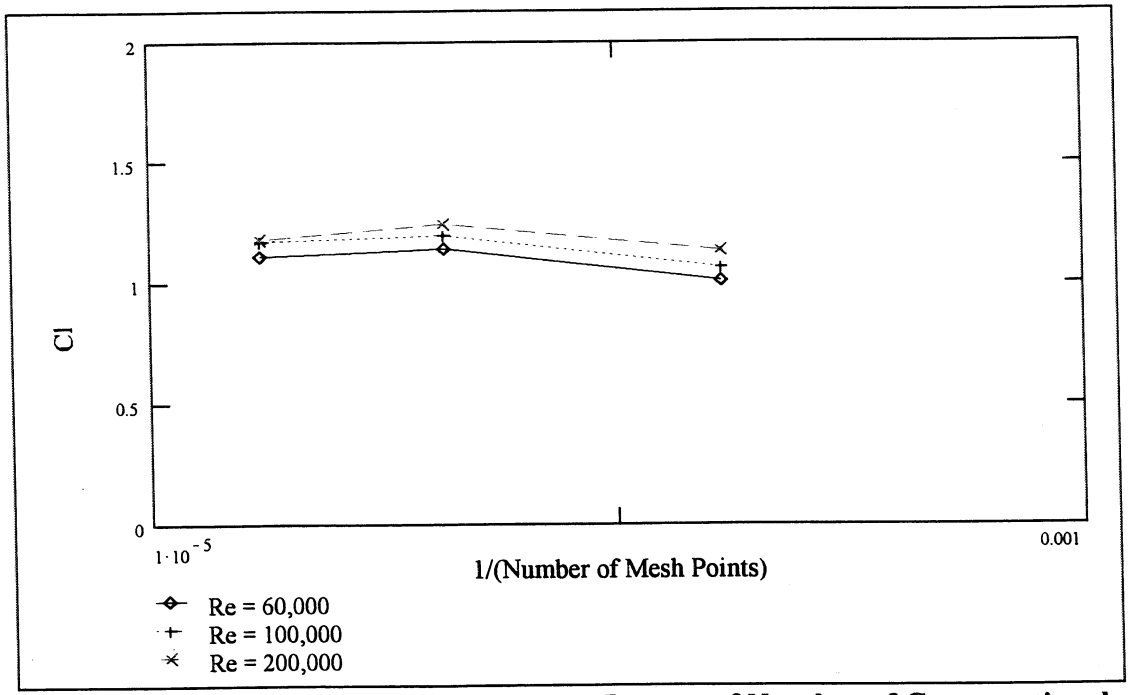

Figure 21: Calculated Lift Coefficient vs. Inverse of Number of Computational Mesh Points at α = 8.01°

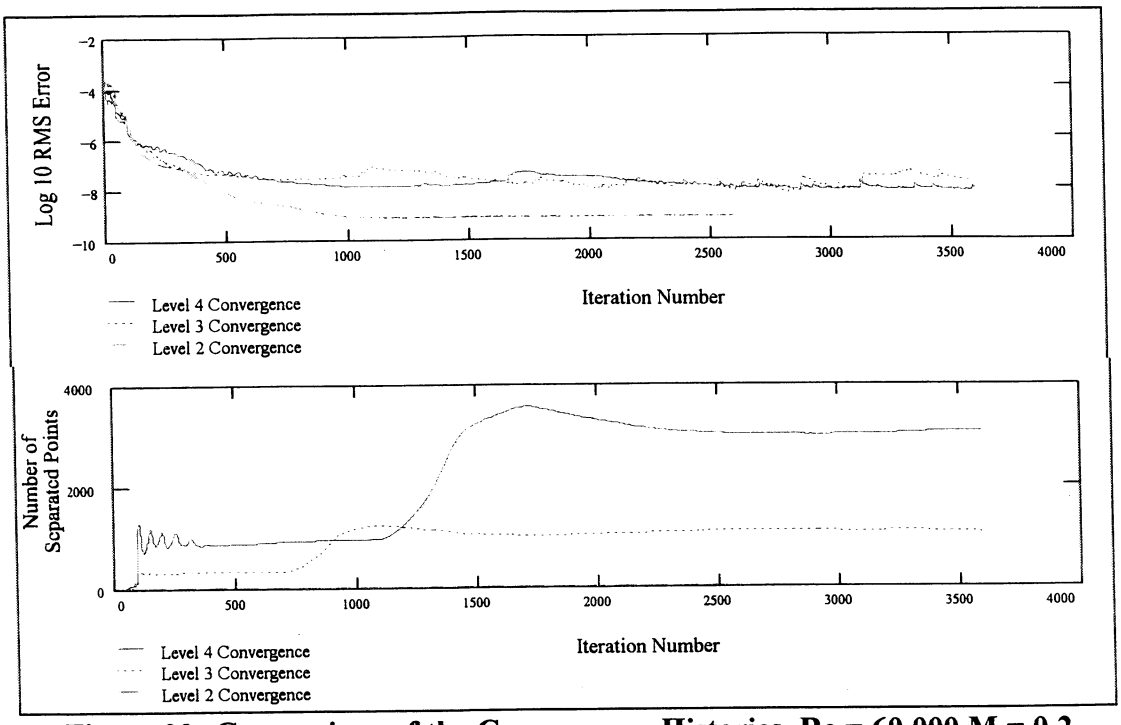

Figure 22: Comparison of the Convergence Histories, Re = 60,000 M = 0.2

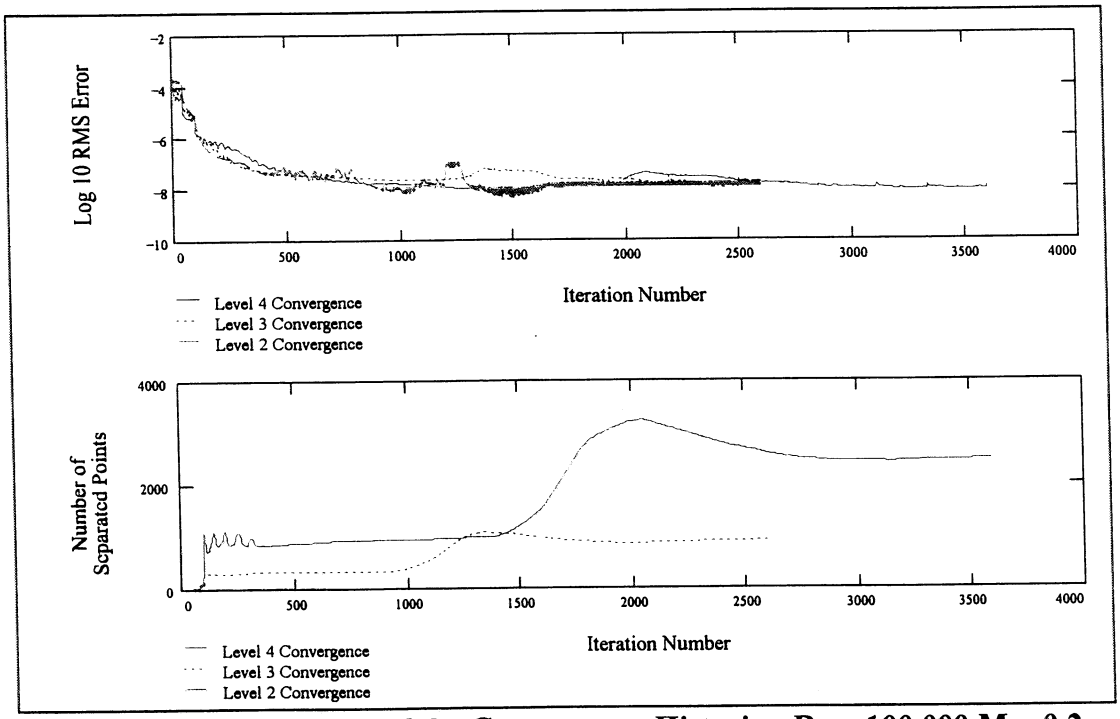

Figure 23: Comparison of the Convergence Histories, Re = 100,000 M = 0.2

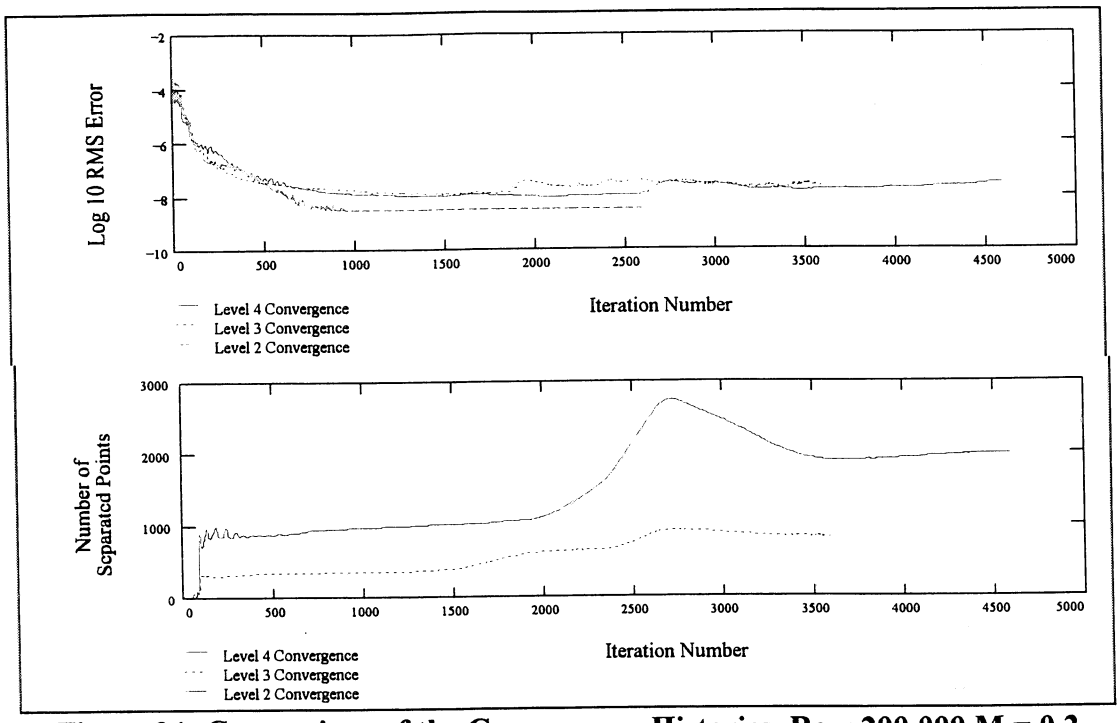

Figure 24: Comparison of the Convergence Histories, Re = 200,000 M = 0.2

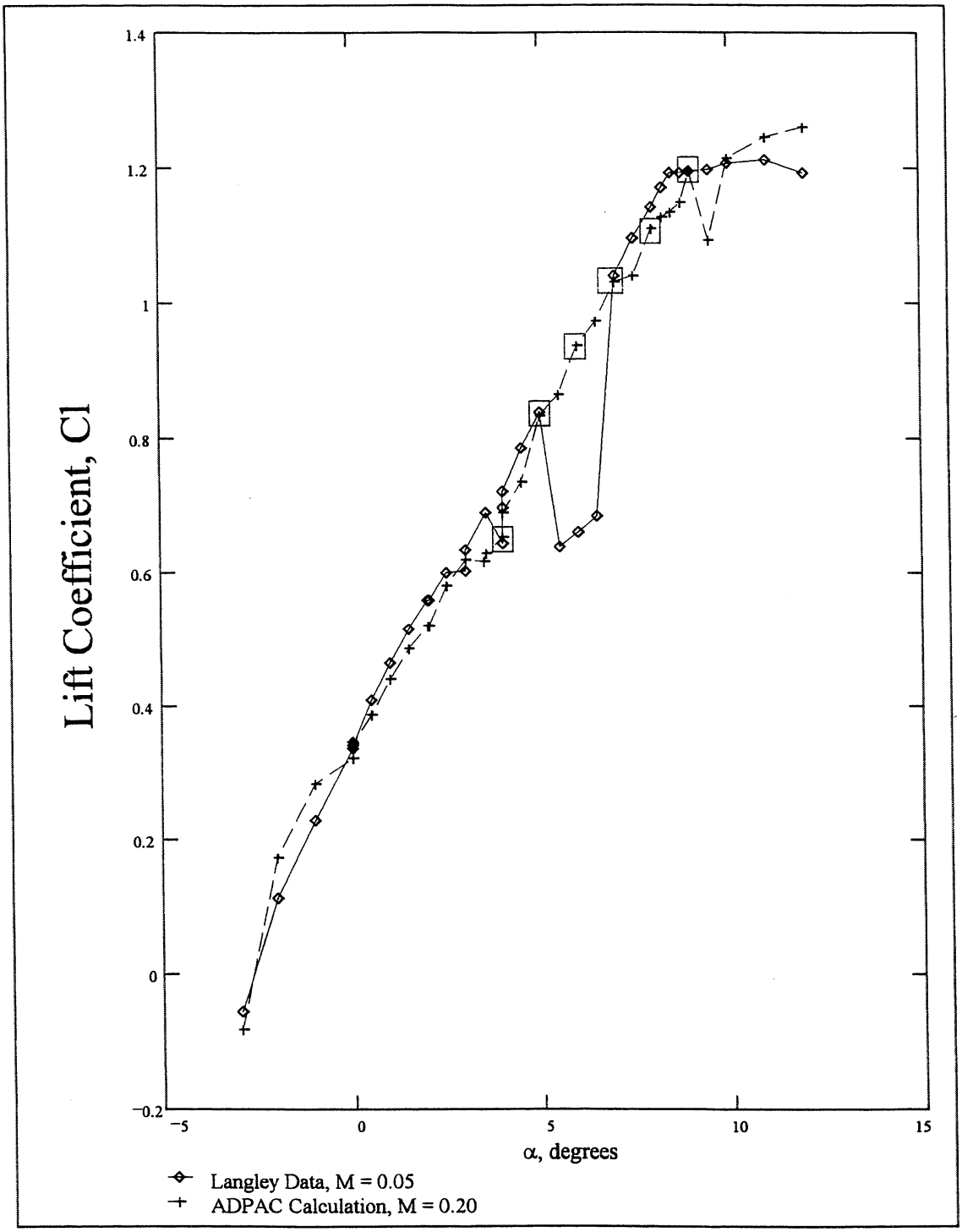

Figure 25: Comparison of Measured and Calculated Lift Coefficient versus Angle of Attack for Re = 60,000

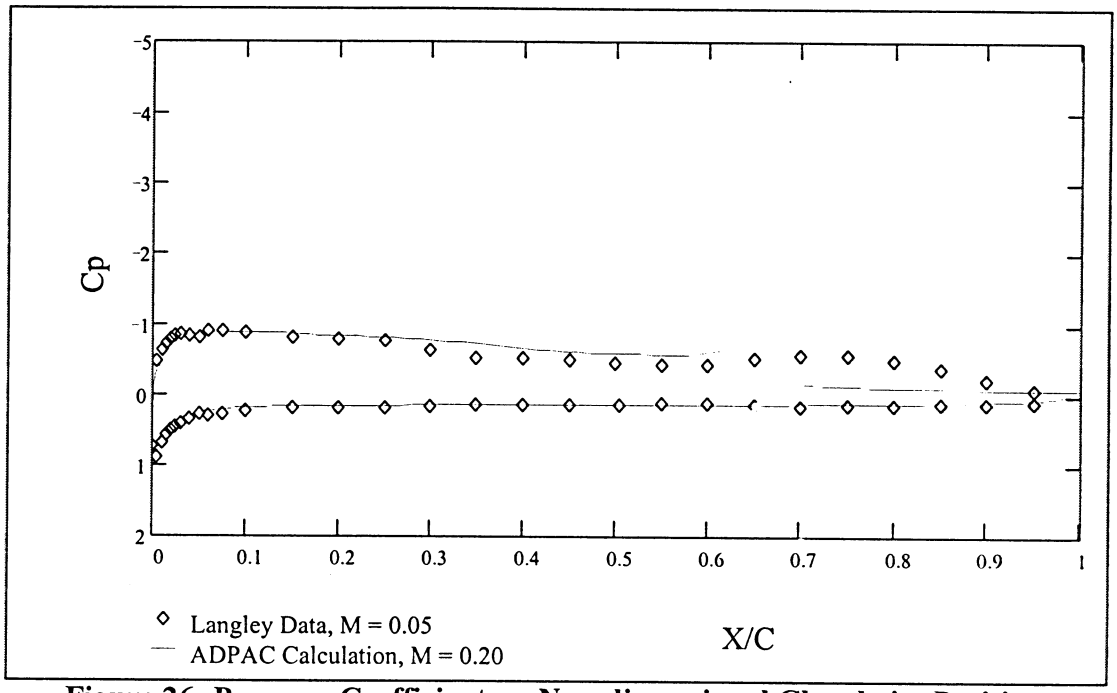

Figure 26: Pressure Coefficient vs. Non-dimensional Chordwise Position, Re = 60,000 α = 4.00°

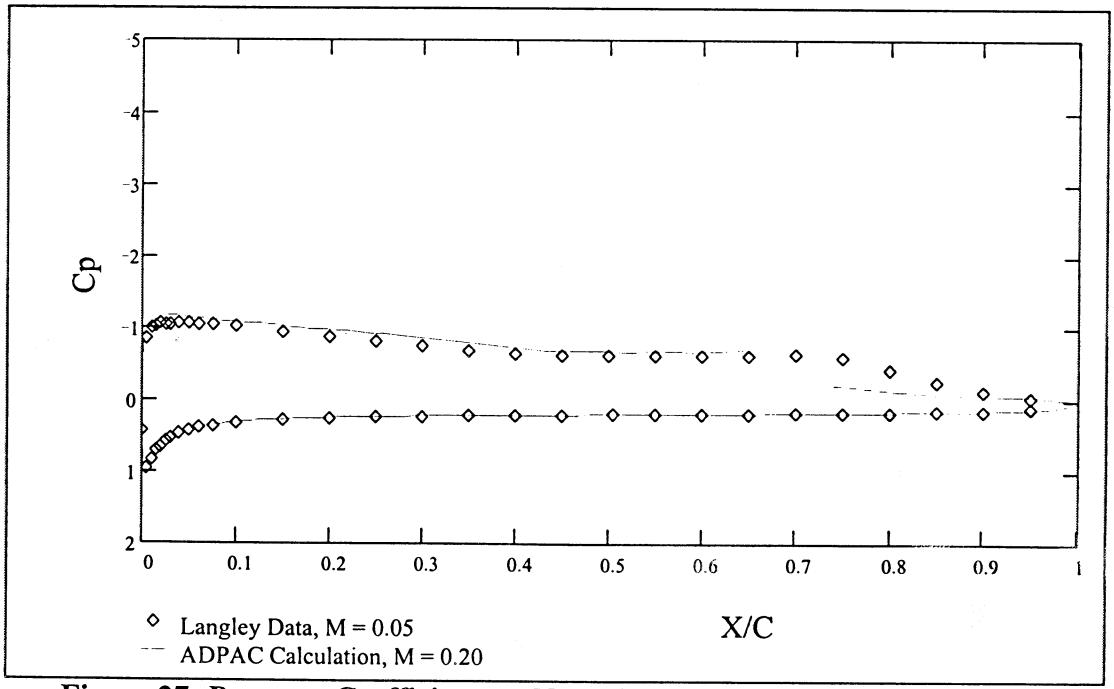

Figure 27: Pressure Coefficient vs. Non-dimensional Chordwise Position, Re = 60,000 α = 4.99°

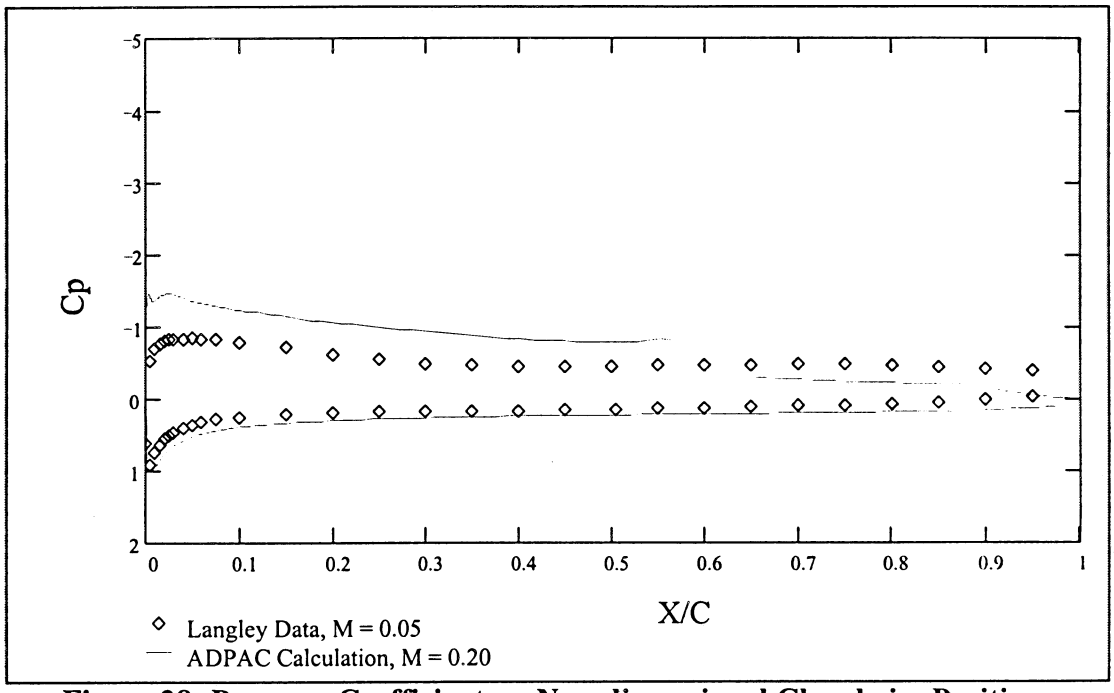

Figure 28: Pressure Coefficient vs. Non-dimensional Chordwise Position, Re = 60,000 α = 6.01°

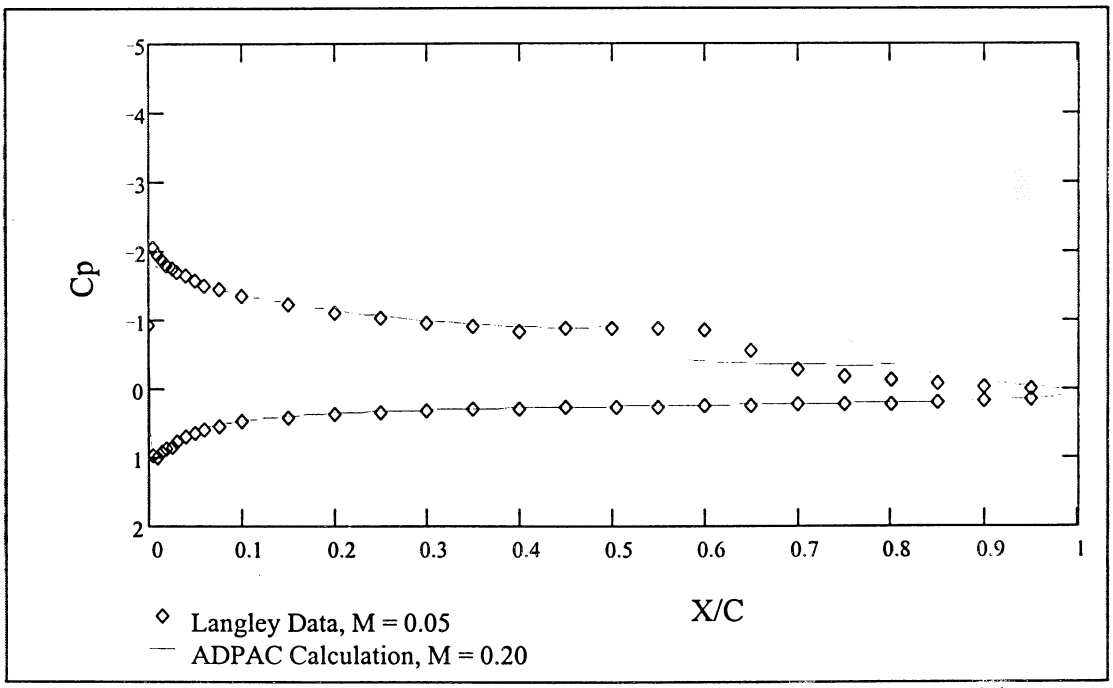

Figure 29: Pressure Coefficient vs. Non-dimensional Chordwise Position, Re = 60,000 α = 7.00°

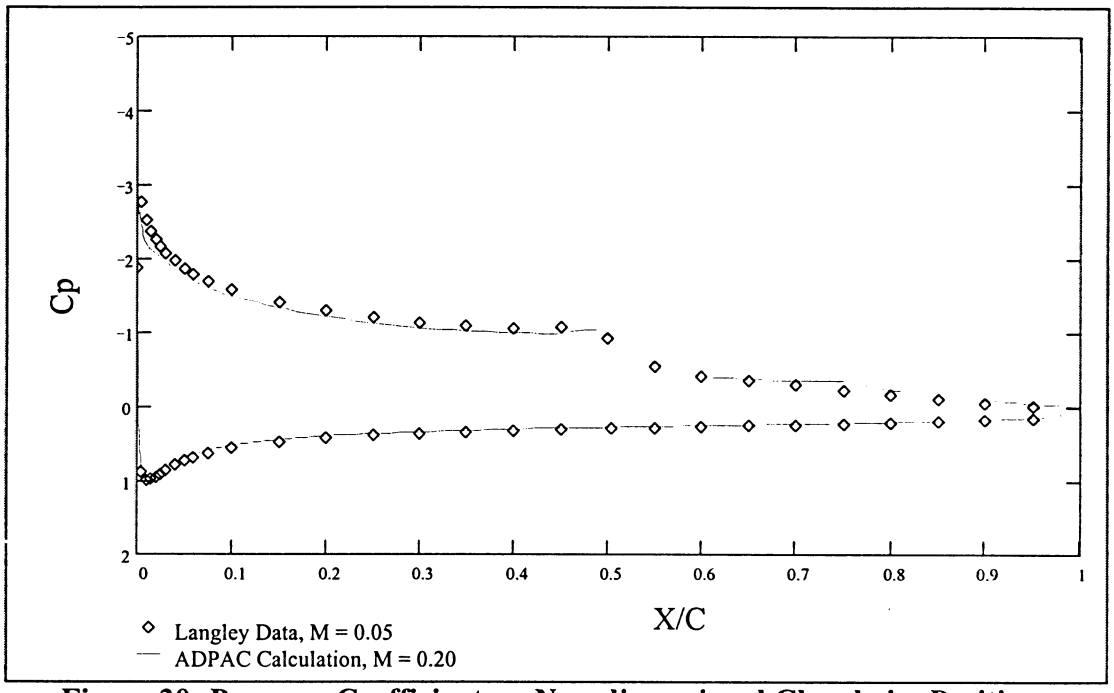

Figure 30: Pressure Coefficient vs. Non-dimensional Chordwise Position, Re = 60,000 α = 8.01°

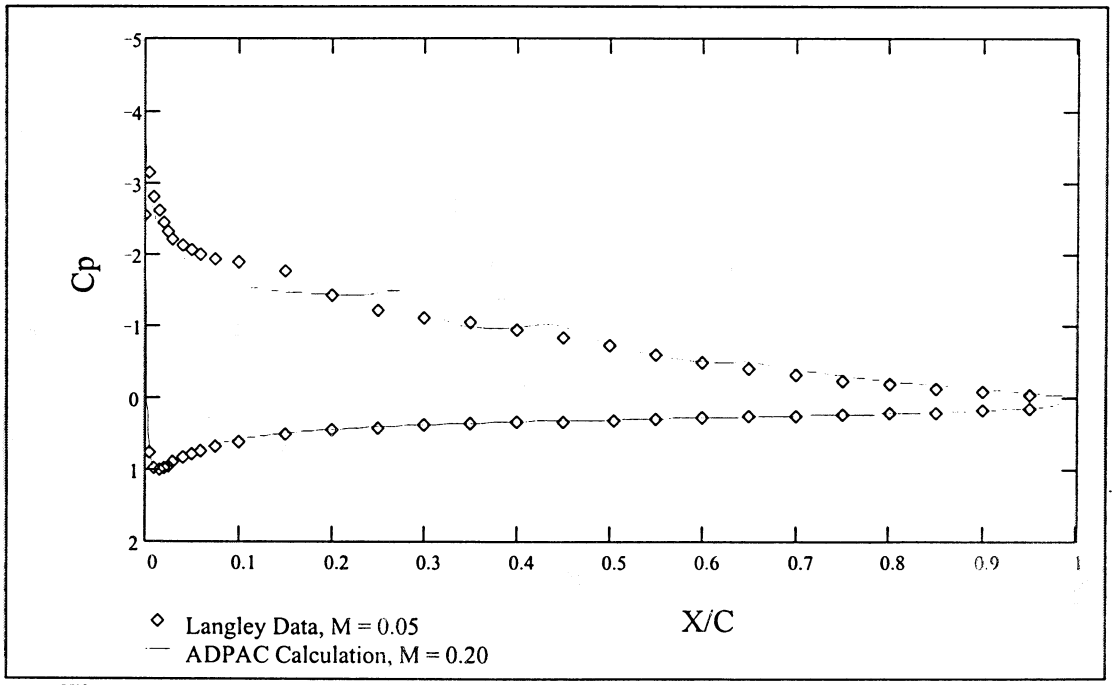

Figure 31: Pressure Coefficient vs. Non-dimensional Chordwise Position, Re = 60,000 α = 9.00°

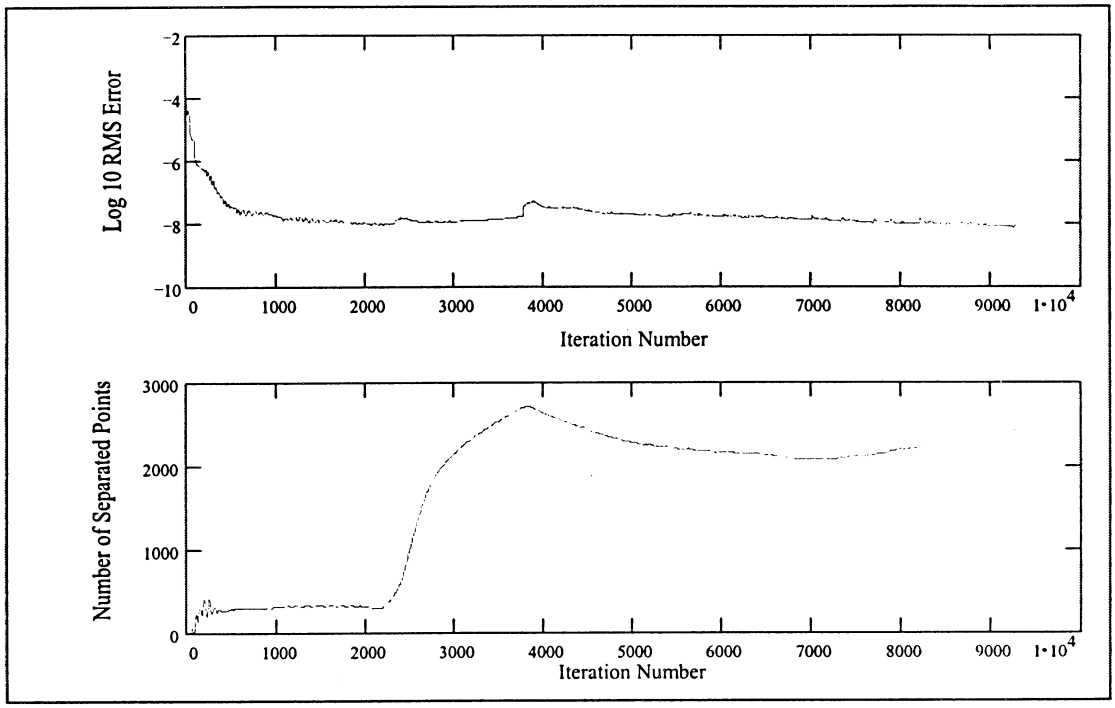

Figure 32: ADPAC Convergence History, Re = 60,000 M = 0.20 α = 4.00°

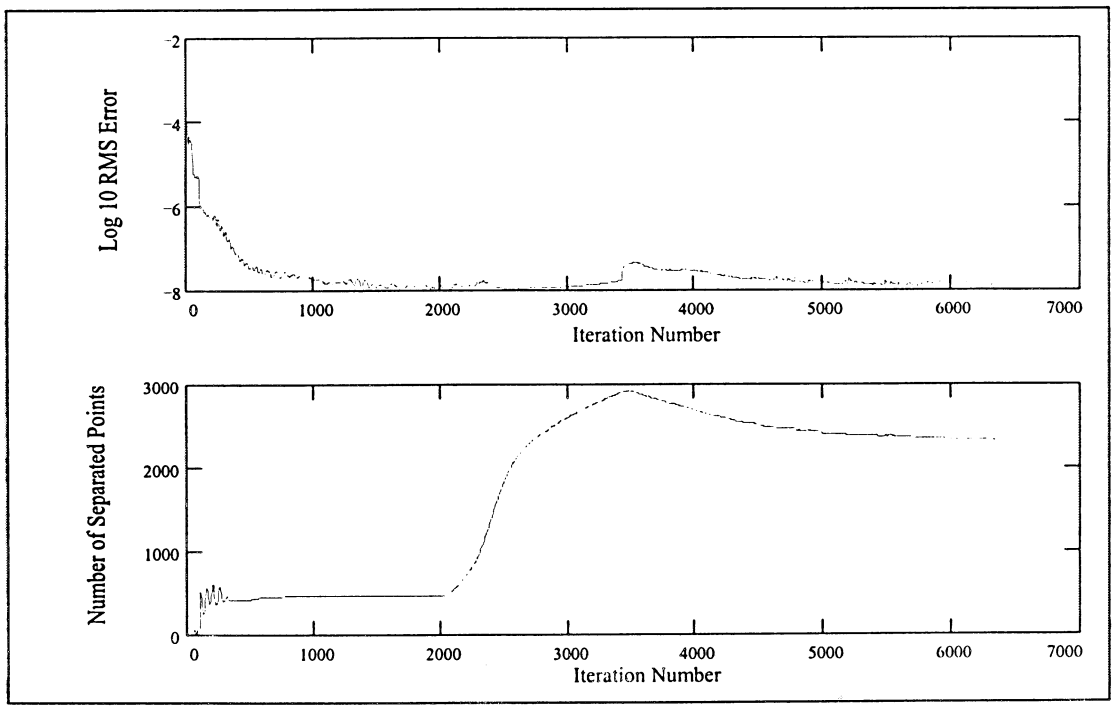

Figure 33: ADPAC Convergence History, Re = 60,000 M = 0.20 α = 4.99°

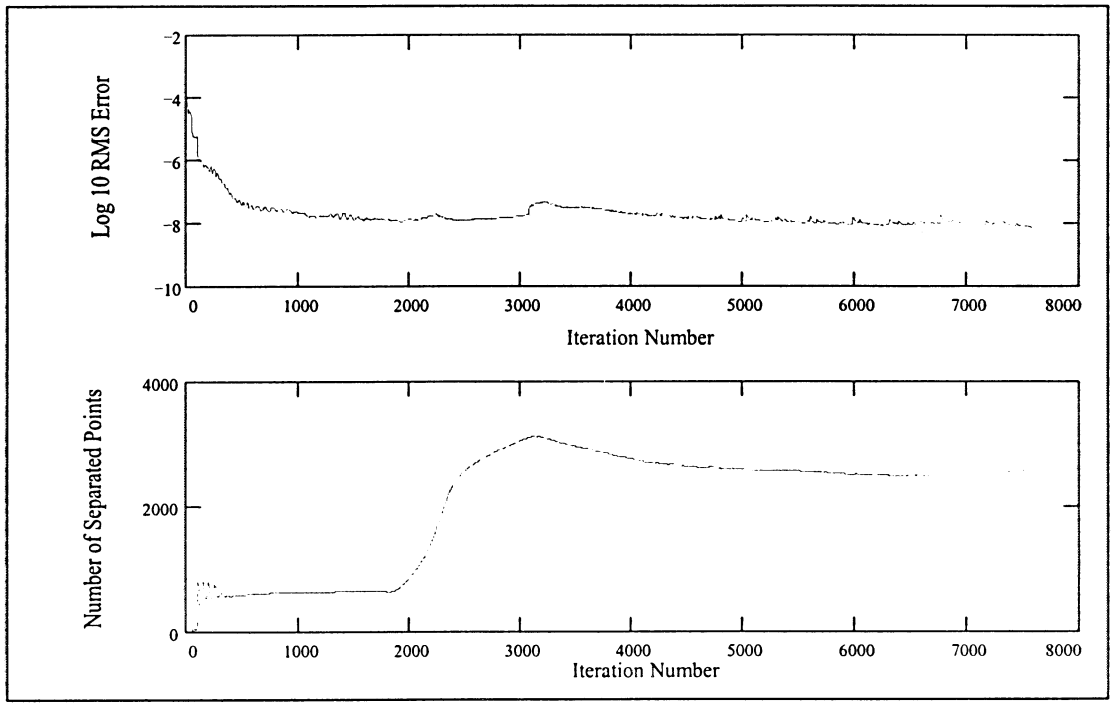

Figure 34: ADPAC Convergence History, Re = 60,000 M = 0.20 α = 6.01°

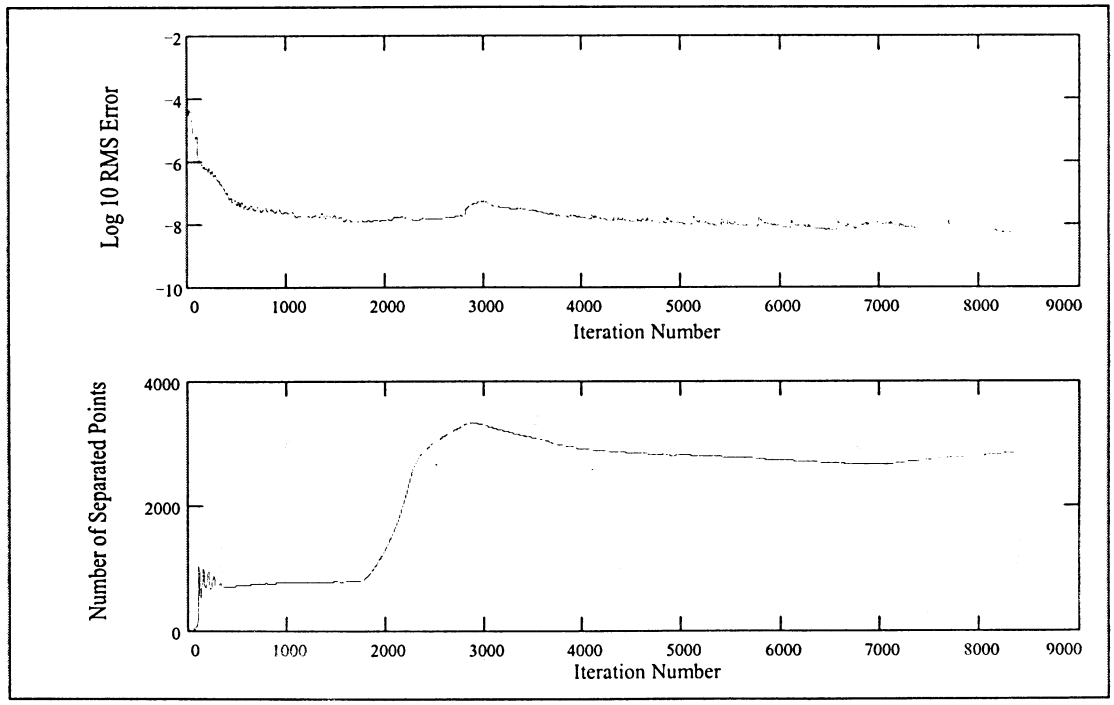

Figure 35: ADPAC Convergence History, Re = 60,000 M = 0.20 α = 7.00°

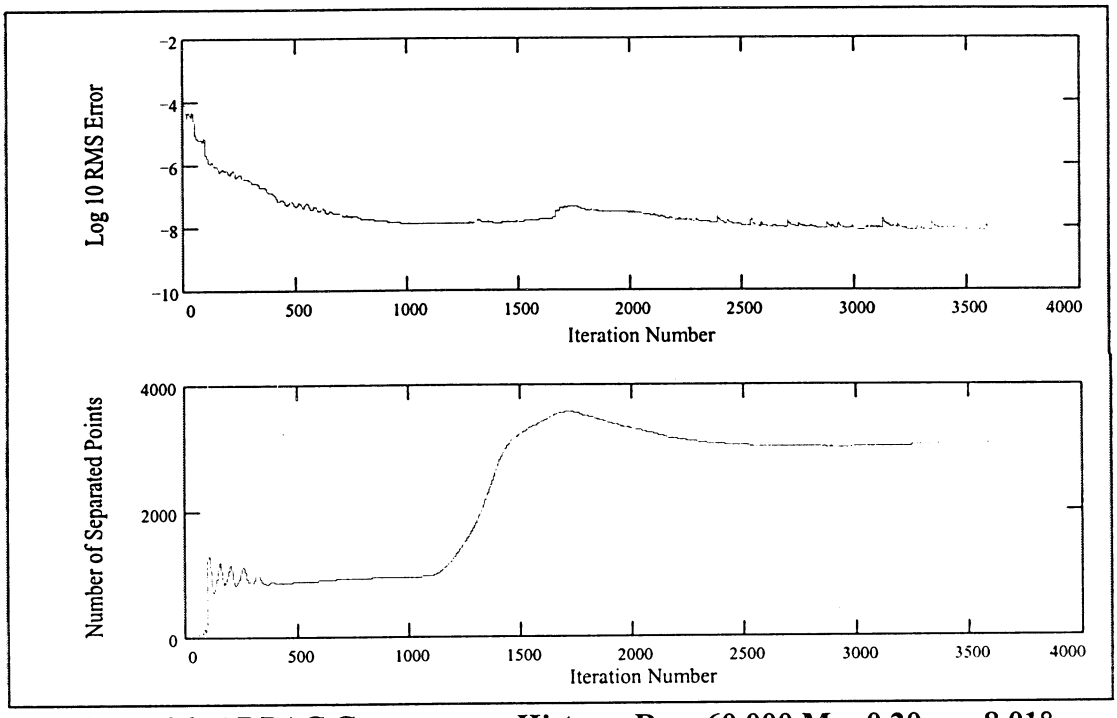

Figure 36: ADPAC Convergence History, Re = 60,000 M = 0.20 α = 8.01°

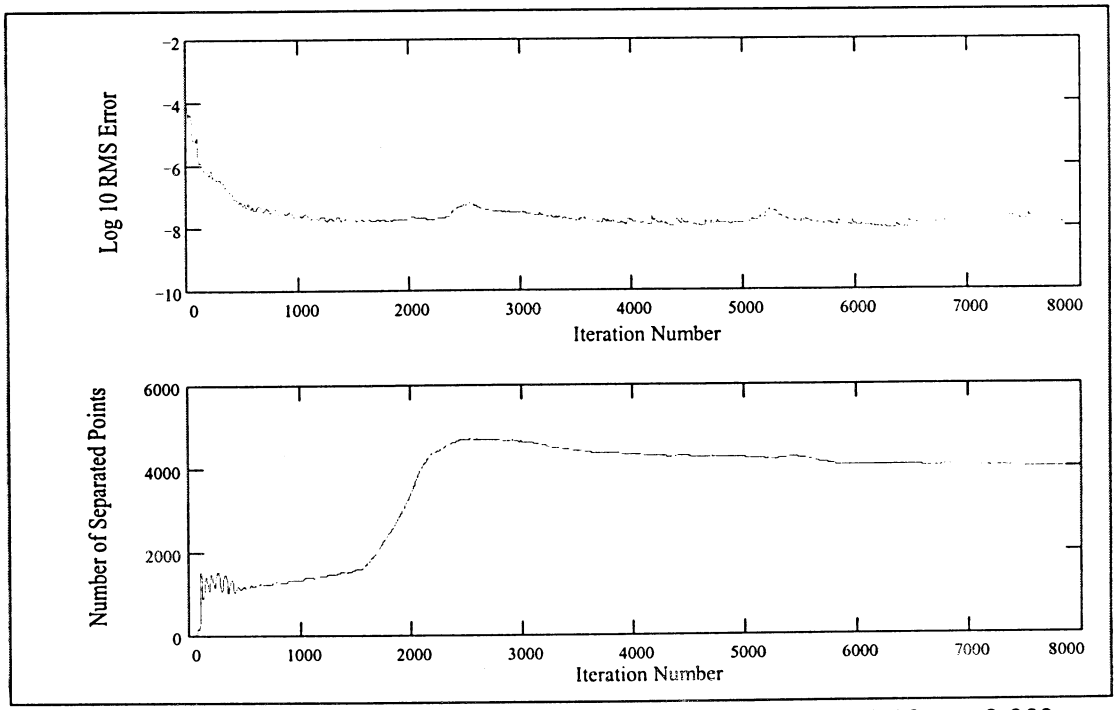

Figure 37: ADPAC Convergence History, Re = 60,000 M = 0.20 α = 9.00°

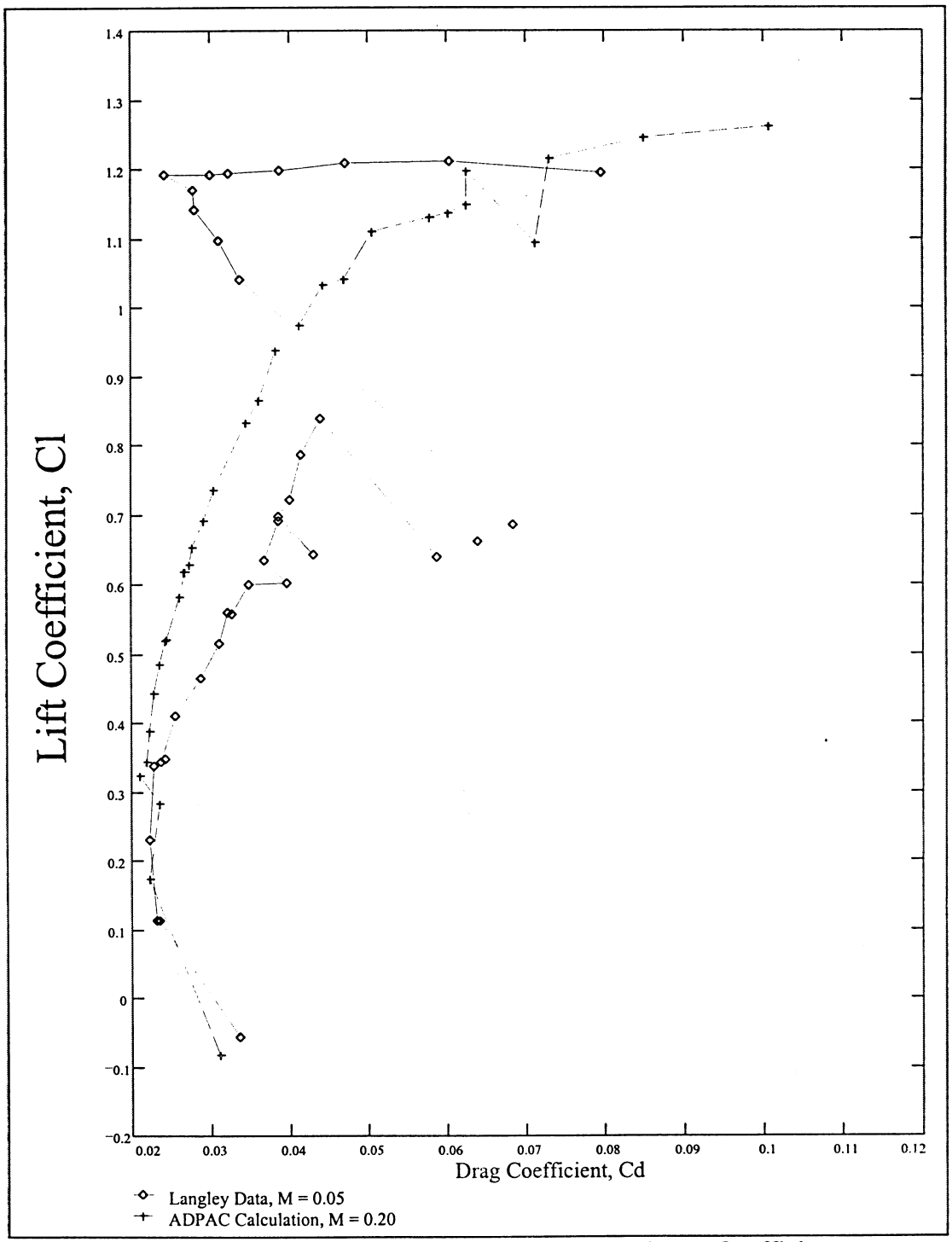

Figure 38: Comparison of Measured and Calculated Drag Coefficient versus Lift Coefficient for Re = 60,000

CHAPTER 4

Propeller Design Using Experimental Airfoil Data

Fundamentals of propeller theory were established by Glauert as early as 1926 (Ref. 11). Primarily because of the absence of computers, solutions of Glauert's analysis theory could only be obtained after making a number of simplifying assumptions. While the basic theory has remained the same, Adkins and Liebeck have recently removed most of the assumptions, establishing iterative design and analysis procedures which, with the aid of a computer, can solve for the geometry or performance of a propeller quickly.

Glauert used a combination of momentum and blade element theory to model the propeller. In the momentum theory, the flow upstream and downstream of the propeller is considered to be a potential flow, that is, the fluid is assumed to be inviscid, incompressible, and irrotational. The propeller is thought of to have a large number of blades so that it could be represented as an 'actuator disc.' Further, Glauert assumed that the axial velocity passing through the actuator disc is continuous, and the pressure over the surface of the disc is constant although it increases discontinuously after passing through the disc.

Glauert used a blade element theory to get more detailed information on the performance of the propeller blades. In this theory, flow past any blade airfoil section is assumed to be two-dimensional and the lift at each section results from the circulation of flow around the blade. Trailing vortices are shed from the blade and

pass downstream in a helical vortex sheet, and interference from these vortices cause the rise in axial and radial velocities through the propeller. Forces on the blade elements can be resolved, and once integrated over the length of the blade, ultimately yield propeller thrust, power, and efficiency.

Strip-theories other than Glauert's momentum-blade element theory exist, differing only in the way in which the induced velocities are found (Ref.12). It was Adkins and Liebeck (Ref. 2), however, who published algorithms for iterative design and analysis procedures in which many of the simplifying assumptions were eliminated. Specifically, Adkins and Liebeck's procedures eliminated the small angle assumption, and the lightly loaded assumption in the Prandtl approximation for momentum loss due to radial flow. Their procedures continue to neglect contraction of the wake. If the vortex sheet is assumed to form a rigid helical surface, the Betz condition for minimum energy loss will be met. A design will be optimized when viscous as well as momentum losses are minimized. To do this, the designer should specify that each section operate at an angle of attack corresponding to the maximum lift-to-drag ratio.

Adkins and Liebeck give eleven steps describing the iterative design procedure in Reference 2. Briefly, the parameters specified at the beginning of a design are: power, hub and tip radii, rotational speed, flight velocity, number of blades, number of radial stations along the blade, and either a lift coefficient or chord length distribution along the blade. The program iterates to find blade twist angles,

chord or lift coefficient distributions (depending on which was specified in the input), radial and axial interference factors, Reynolds number, and relative Mach number.

A Reynolds number distribution was specified for the initial propeller designs (Fig. 39). This ensured that the two-dimensional airfoil experimental data available to the design program would be representative of the blade sections. The program used simple conditional statements to apply the experimental data from the Langley tests shown in Figures 1 and 2. For chord Reynolds number equal to or exceeding 100,000, the experimental data for Reynolds number of 100,000 was used, while the experimental data for Reynolds number of 60,000 was used if the chord Reynolds number was below 100,000.

Several designs were produced using the specified Reynolds number distribution. The propeller diameter and number of blades were varied until the maximum lift coefficient along the blade did not exceed 80% of the maximum experimental lift coefficient for the section. For a two-bladed propeller, these criteria were met when the diameter was increased to 6.8 m (22.3 ft). A 4.6 m (15.1 ft) three-bladed propeller and a 3.5 m (11.5 ft) four-bladed propeller also met these requirements. Of the three designs, the three-bladed propeller was the most feasible. While there are several benefits to a two-bladed design, the extremely large diameter required raises manufacturing questions that would be avoided in the smaller three-bladed design. The three-bladed design yielded better efficiency than the even smaller four-bladed design because of the decreased disk loading. Efficiencies of the

three-bladed propeller and the four-bladed propeller were 85.3% and 81.5%, respectively. Comparisons of the propeller geometries can be found in Figures 40 through 42.

Examination of the blade twist distributions for all three designs (Fig. 40) showed a 'hook' in the curve as the blade was twisted through the stalled portion of the lift curve for the experimental data at the Reynolds number of 60,000 (Fig. 1). Since viscous losses were not minimized in these designs, the three-bladed design was optimized by relaxing the requirement that section lift coefficient be less than 80% of the maximum and specifying a constant lift coefficient corresponding to the maximum lift-to-drag ratio point in the experimental data set (Fig. 43 - 44). Blade twist, chord, lift coefficient, and chord Reynolds number distributions can be found in Figures 45 through 47. While this eliminated the 'hook' in the twist distribution (Fig. 40), it was clear that the lift coefficients near the hub would have to be decreased in order to increase the chordlengths of the inboard sections. The exercise of refining the hub sections was deferred to the next design trials.

The design studies using the Langley experimental data were useful in several ways. These studies showed that the specified Reynolds number distribution did yield a reasonable propeller geometry. With refinement, chordlengths of the inboard sections could be improved and the hook in the twist distribution curve could be eliminated. Knowing the Reynolds number and relative Mach number distribution over the blade would help to account for compressibility effects that were so far

neglected in the present designs. As will be shown in the next chapter, ADPAC would be used to make performance predictions for the Eppler 387 airfoil operating at these transonic low Reynolds number conditions. Finally, the design studies were useful in identifying feasible values for the propeller diameter and number of blades.

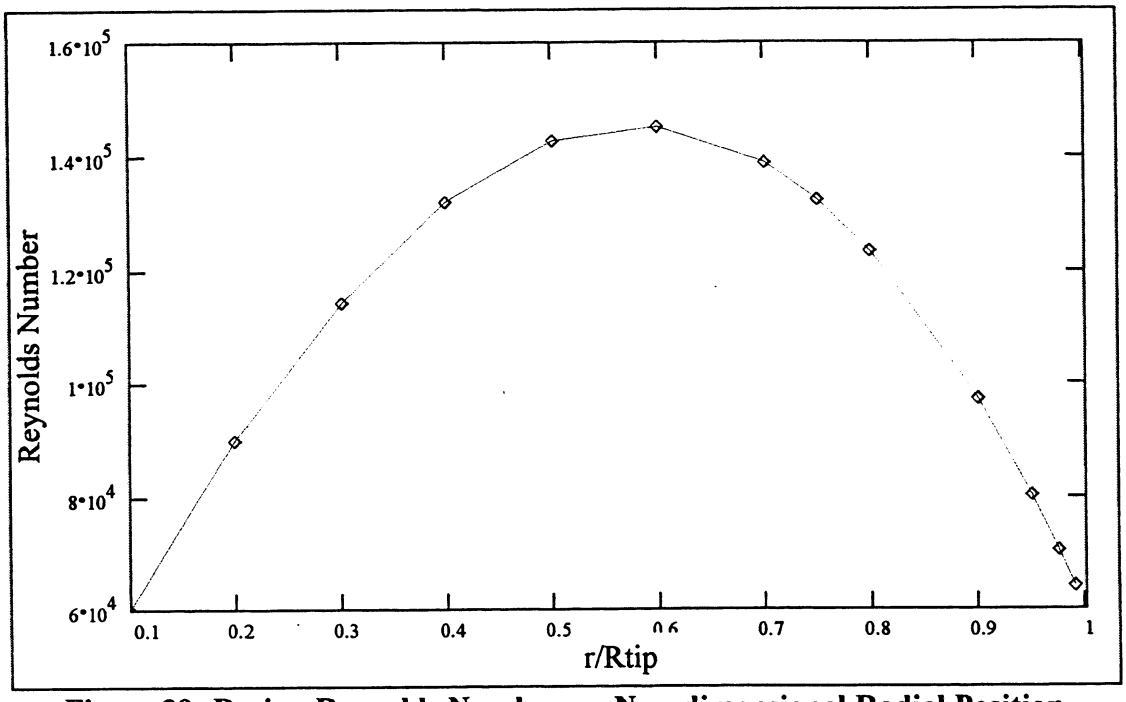

Figure 39: Design Reynolds Number vs. Non-dimensional Radial Position

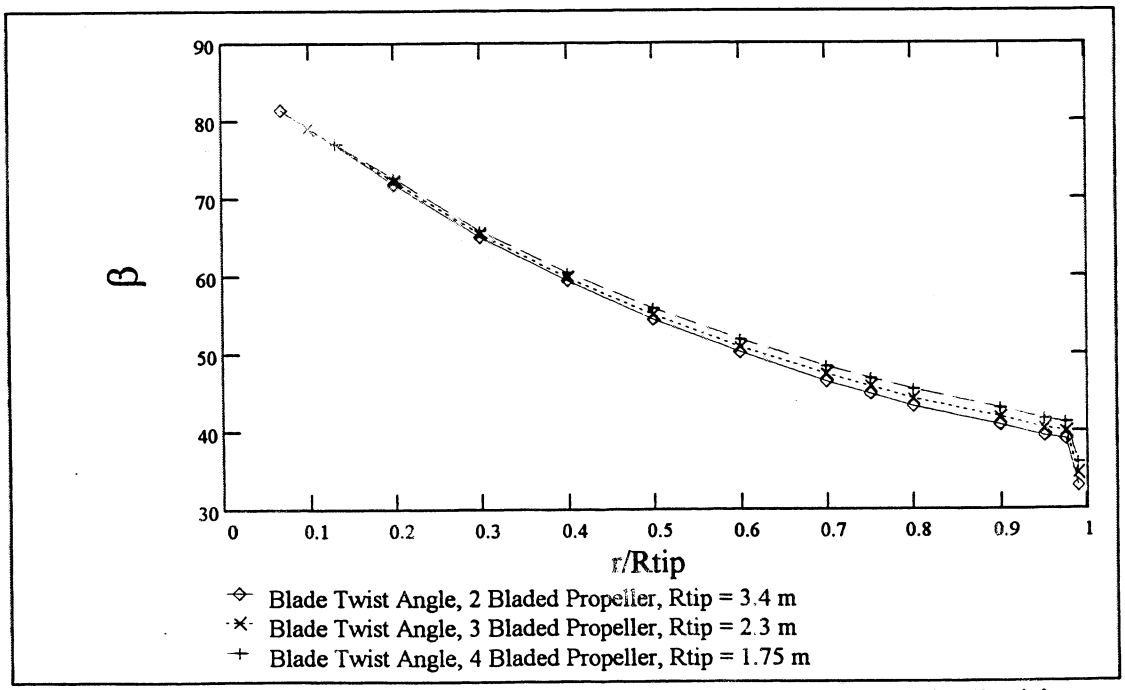

Figure 40: Blade Twist Angle (degrees) vs. Non-dimensional Radial Position, Designed Using Langley 2-D Experimental Data Only

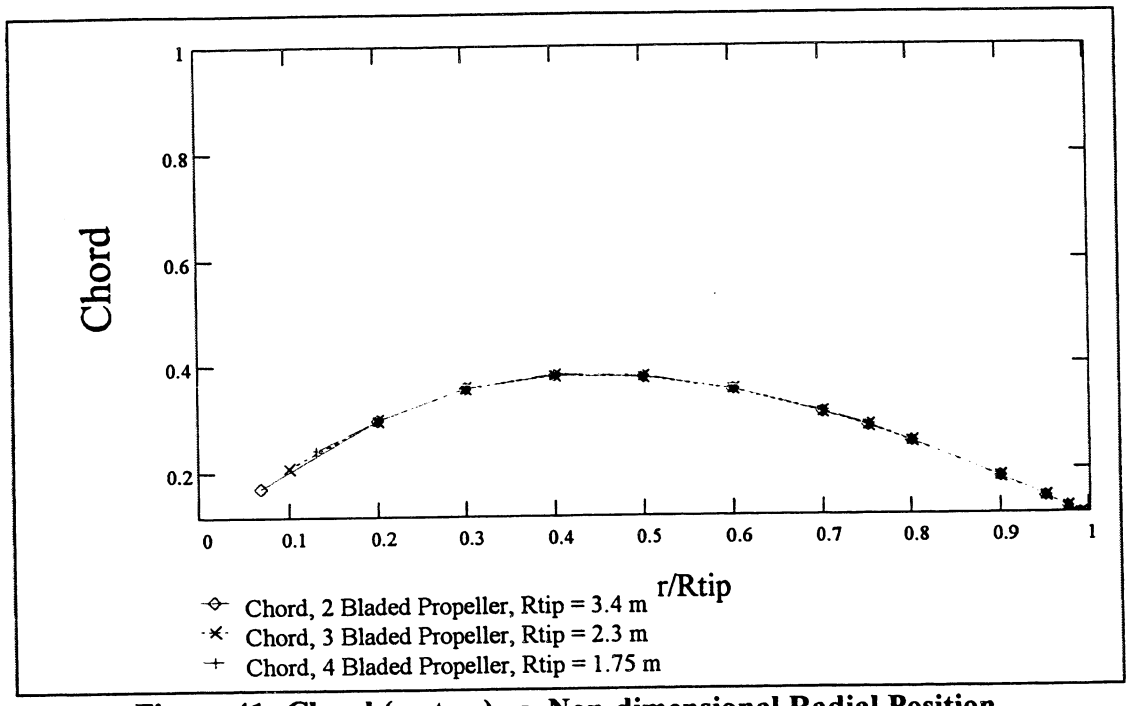

Figure 41: Chord (meters) vs. Non-dimensional Radial Position, Designed Using Langley 2-D Experimental Data Only

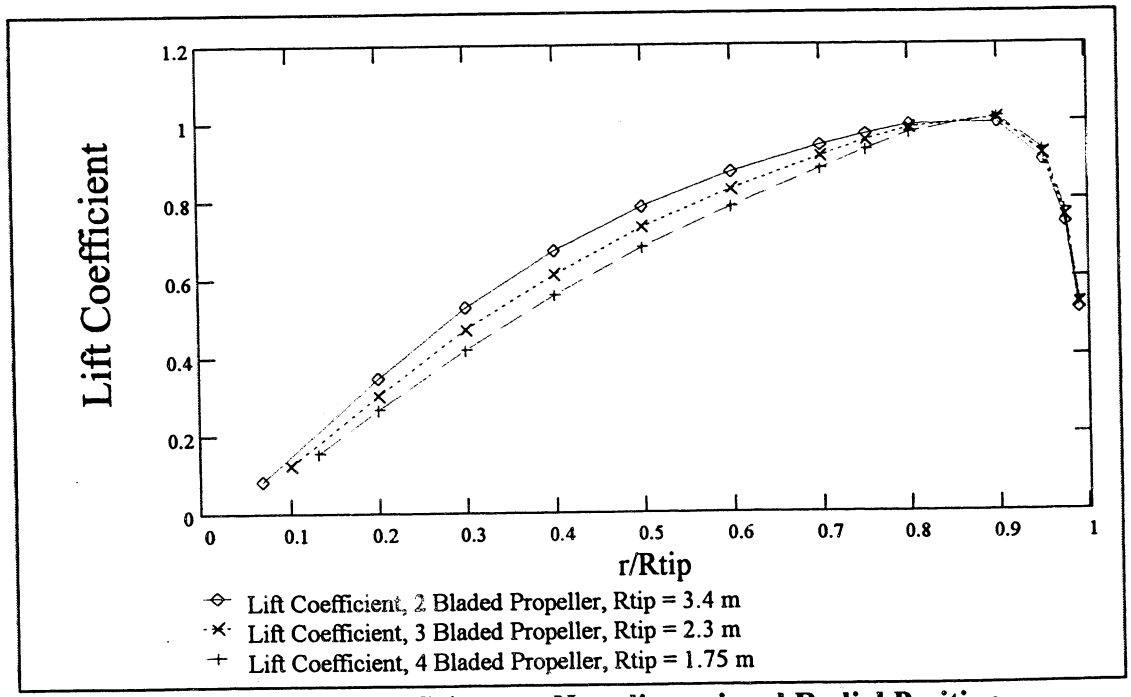

Figure 42: Lift Coefficient vs. Non-dimensional Radial Position, Designed Using Langley 2-D Experimental Data Only

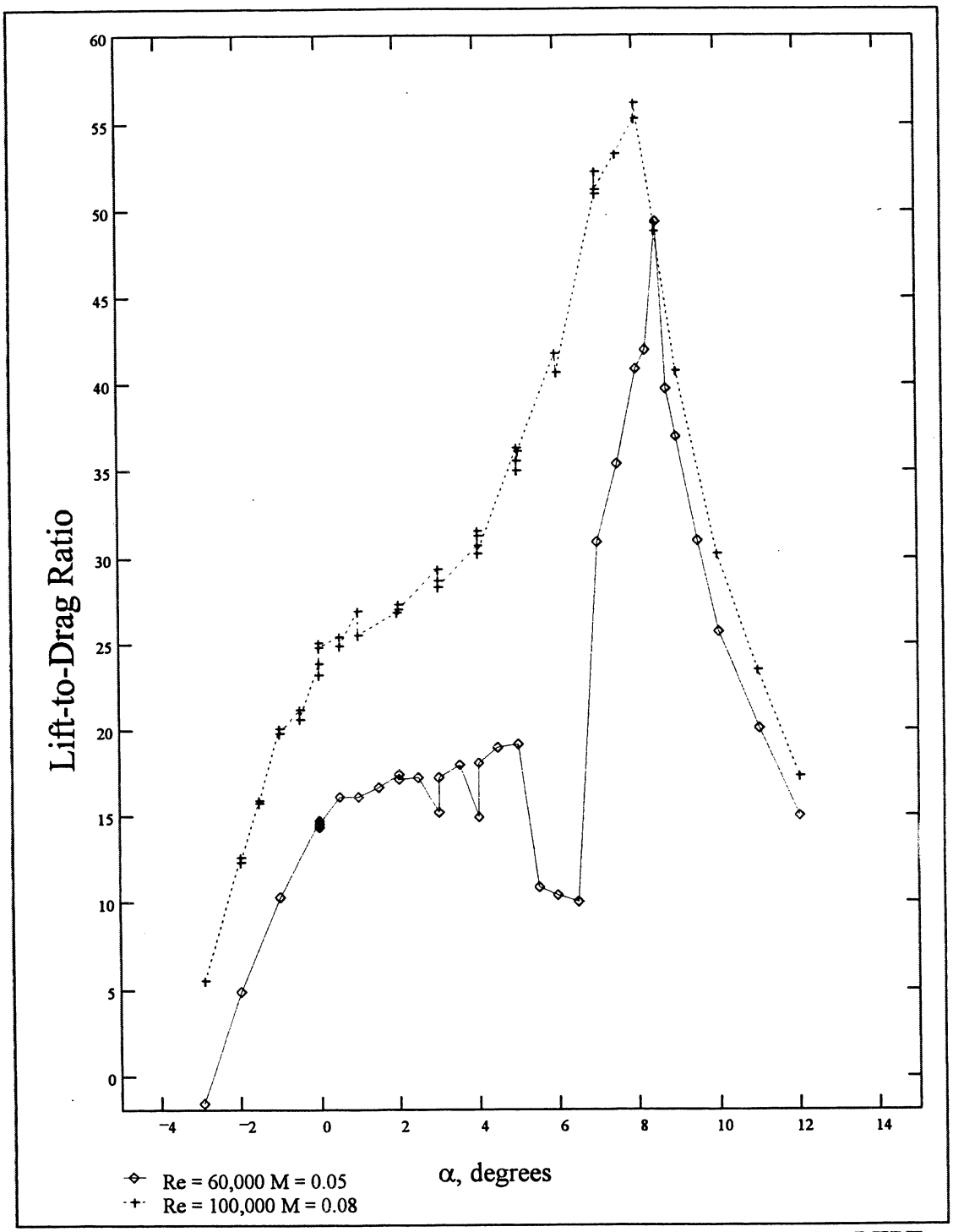

Figure 43: Lift-to-Drag Ratio versus Angle of Attack for the Langley LTPT Experimental Data

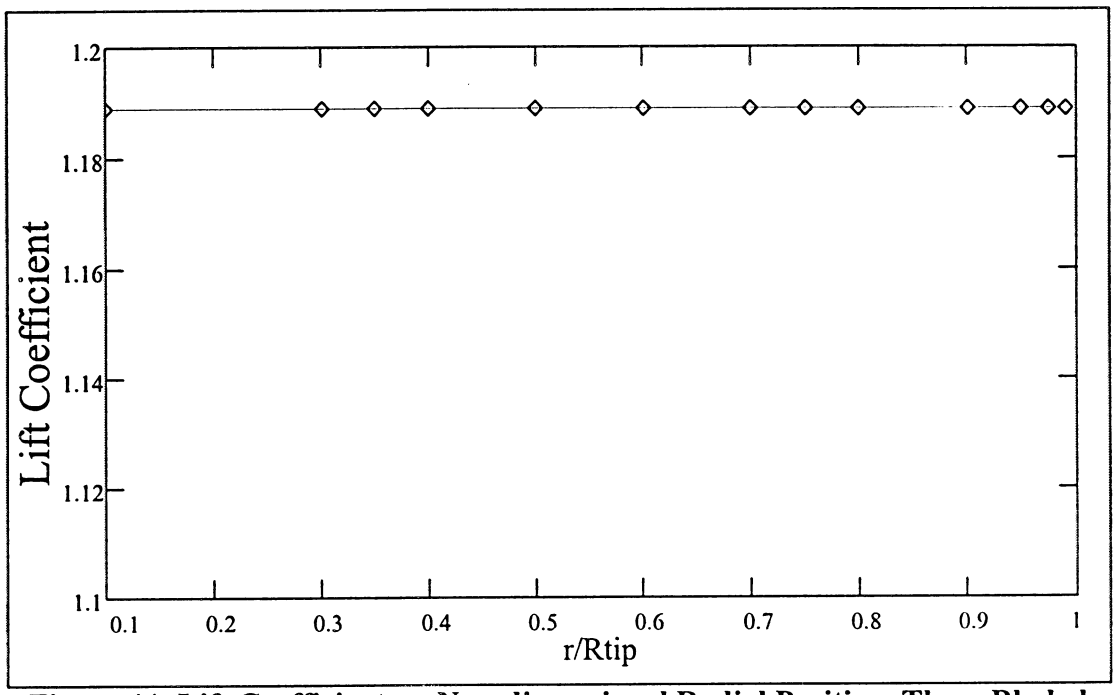

Figure 44: Lift Coefficient vs. Non-dimensional Radial Position, Three Bladed Design, Tip Radius = 2.3 m, Langley 2-D Experimental Data Only

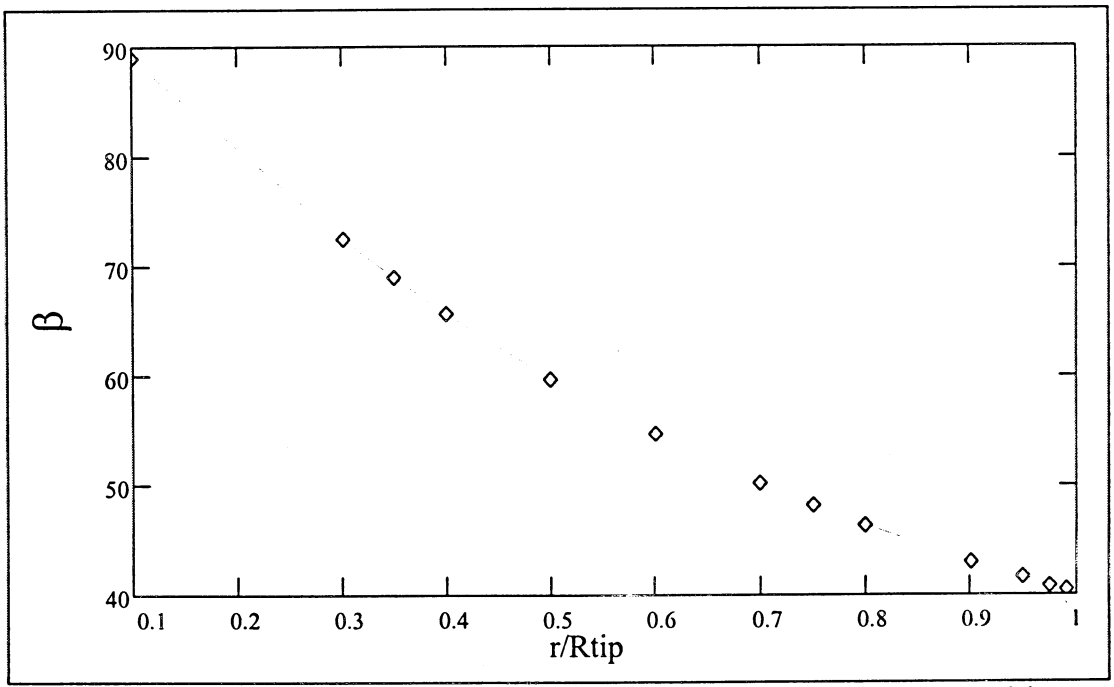

Figure 45: Blade Twist Angle (degrees) vs. Non-dimensional Radial Position, Three Bladed Design, Tip Radius = 2.3 m, Langley 2-D Data Only

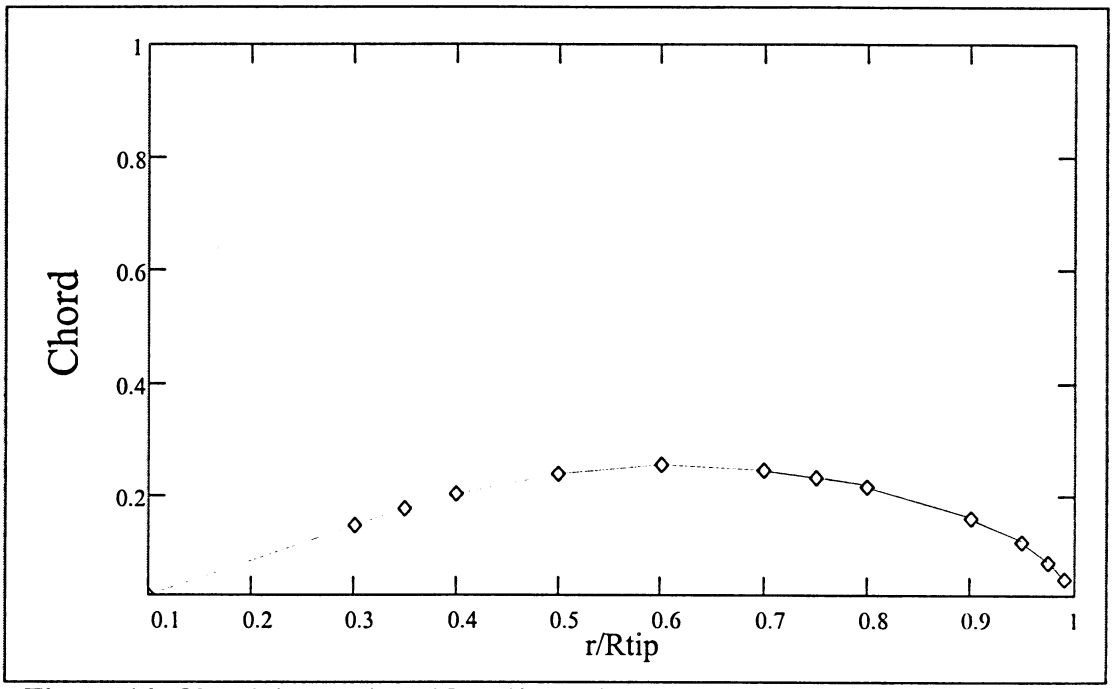

Figure 46: Chord (meters) vs. Non-dimensional Radial Position, Three Bladed Design, Tip Radius = 2.3 m, Langley 2-D Experimental Data Only

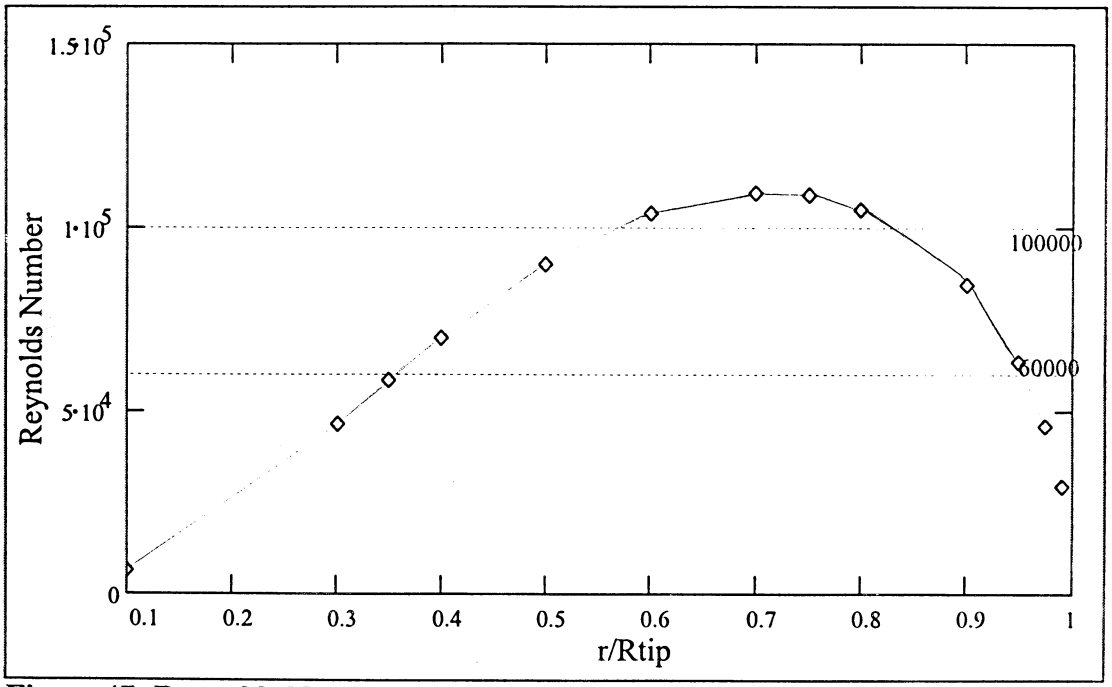

Figure 47: Reynolds Number vs. Non-dimensional Radial Position, Three Bladed Design, Tip Radius = 2.30 m, Langley 2-D Data Only

CHAPTER 5

ADPAC Two-Dimensional Aerodynamic Predictions

ADPAC two-dimensional results were combined with the strip theory design program in an effort to account for compressibility effects so far neglected. To do so, the blade was divided into four segments. The specified propeller Reynolds number distribution and the resulting Mach number distribution were used to identify an average value of the Reynolds number and the Mach number for each segment (Figure 48). These values are listed in Table 3.

Table 3. Reynolds Number-Mach Number Combinations

Segment	Reynolds Number	Mach Number
1	60,000	0.45
2	100,000	0.55
3	100,000	0.65
4	60,000	0.75

The Level 4 computational mesh of the Eppler 387 (Figures 14 and 15) was used to generate section performance predictions for a range of angles of attack for each of the Reynolds number-Mach number combinations in Table 3. Surface pressure coefficients were compared to Langley experimental data that had been corrected for the elevated relative Mach number using the Prandtl-Glauert compressibility correction (Ref. 13)

$$Cp_{corrected} = \frac{Cp_0}{\sqrt{1 - M_\infty{}^2}}$$

where Cp_0 is the value of the incompressible pressure coefficient and M_∞ is the free stream Mach number. The pressure coefficients calculated with ADPAC were in turn integrated to yield lift and pressure drag coefficients. The total drag coefficient was found by adding the viscous drag component once again estimated by drag on both sides of a flat plate given by Schlichting in Reference 10:

$$Cd = \frac{1.328}{\sqrt{\mathrm{Re}}}$$

Lift and drag curves are found in Figures 49 through 52. Plots of the surface pressure coefficients and corresponding ADPAC convergence history plots for angles of attack of 4°, 5°, 6°, 7°, 8°, and 9° are given for Segment 1 in Figures 53 through 64, Segment 2 in Figures 65 through 76, Segment 3 in Figures 77 through 88, and Segment 4 in Figures 89 through 100. Where appropriate, the number of supersonic points at each iteration are included in the convergence history plots.

An examination of the Segment 1 results at Re = 60,000 and M = 0.45 shows that agreement between the ADPAC calculated values and the corrected Langley data is generally good. The calculated suction side pressure recoveries are sharper than the corrected data would suggest for low angles of attack. Just as was seen in the code validation, ADPAC did not predict a laminar stall at angles of attack between 5.00° and 6.49°. For angles of attack between 7.51° and 12.00°, there appears to be periodic shedding of the separated shear layer, similar to that reported by Pauley, et. al. in Reference 4. Figure 101 shows the pressure distribution over the airfoil at an angle of attack at 8.01° and the streamlines shown in Figure 102 for the same

condition indicate multiple separation and reattachment points near the trailing edge of the suction side. These results, as well as all of the other ADPAC results presented here, are not time-accurate, but represent the steady state flow solution achieved with local time stepping. The local time stepping technique advances each cell in time by an increment equal to the maximum allowable time step for that cell. Generally, larger cells away from a boundary layer will have a larger time step than smaller cells closer to a solid surface.

Examination of the results in Segment 2 for a Reynolds number of 100,000 and a Mach number of 0.55 shows that there was also generally good agreement for angles of attack ranging from -2.88° to 4.00°. Shock waves near the leading edge are seen in the ADPAC predictions for angles of attack greater than 6.00°. Full stall is not predicted at 14.04°. The Prandtl-Glauert correction is inadequate for these conditions and an experiment would be needed to validate these predictions.

As Mach number is increased from 0.55 in Segment 2 to 0.65 in Segment 3, more differences are seen between the corrected experimental data and the ADPAC predictions. Shock waves are seen for all angles of attack above 3.00°, and like in Segment 2, full stall of the airfoil at 14.04° is not predicted by ADPAC.

Representative of the tip sections, Segment 4 with a Reynolds number of 60,000 and a Mach number of 0.75 shows gross differences between the corrected Langley data and the ADPAC predictions as would be expected from the inaccuracy of the Prandtl-Glauert correction at these conditions. ADPAC solutions indicate that

the airfoil is unable to produce a strong leading edge suction as a result of the shock waves seen at every angle of attack.

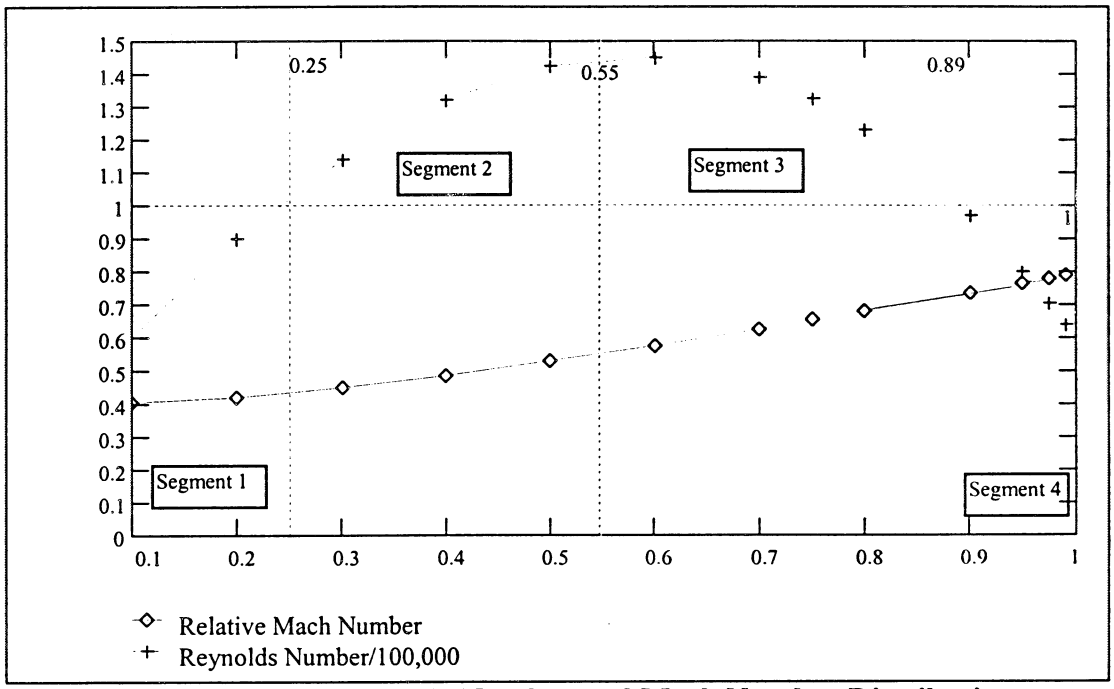

Figure 48: Segmented Reynolds Number and Mach Number Distributions

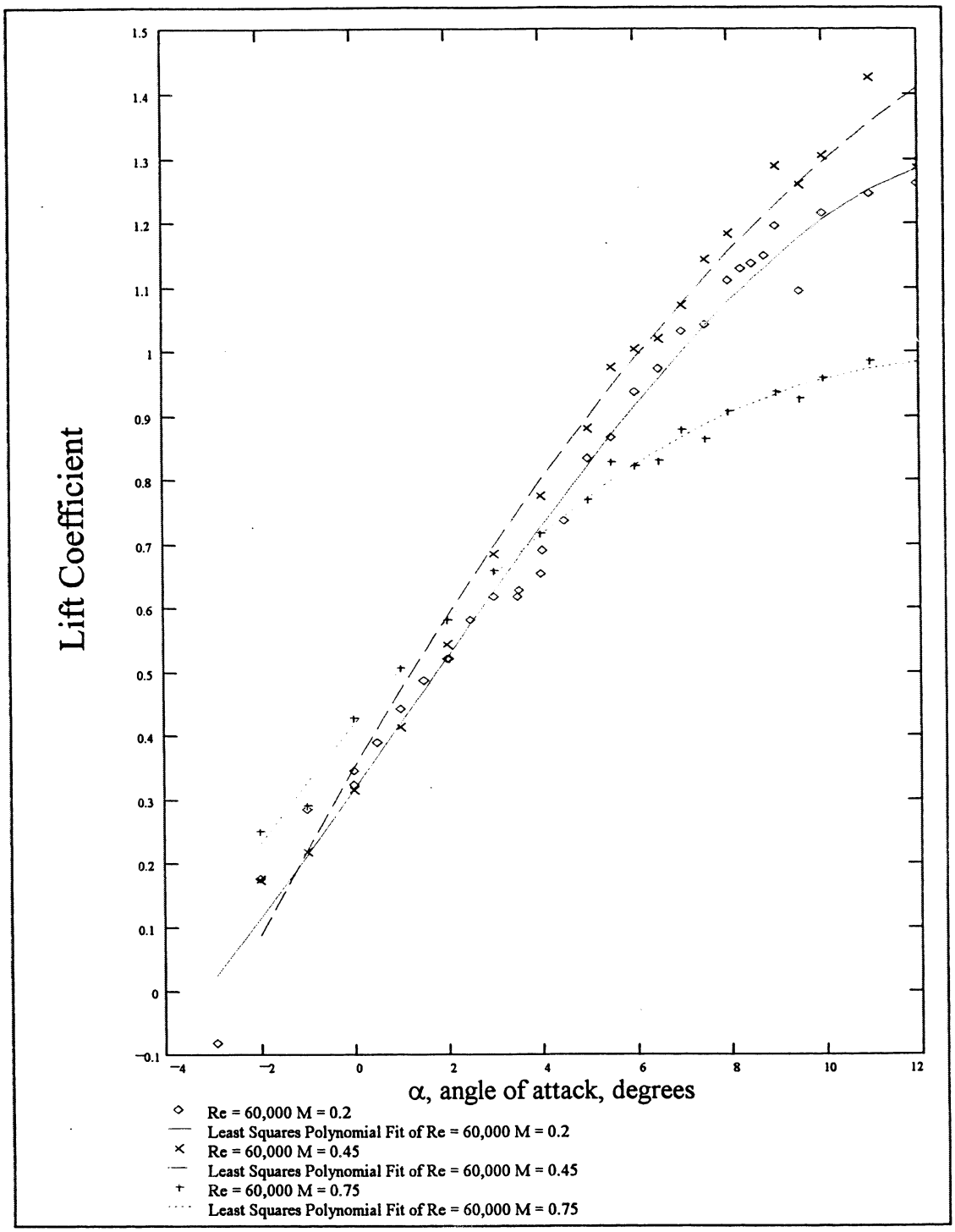

Figure 49: Comparison of ADPAC Predicted Lift Coefficients at Re = 60,000 and M = 0.20, 0.45, 0.75

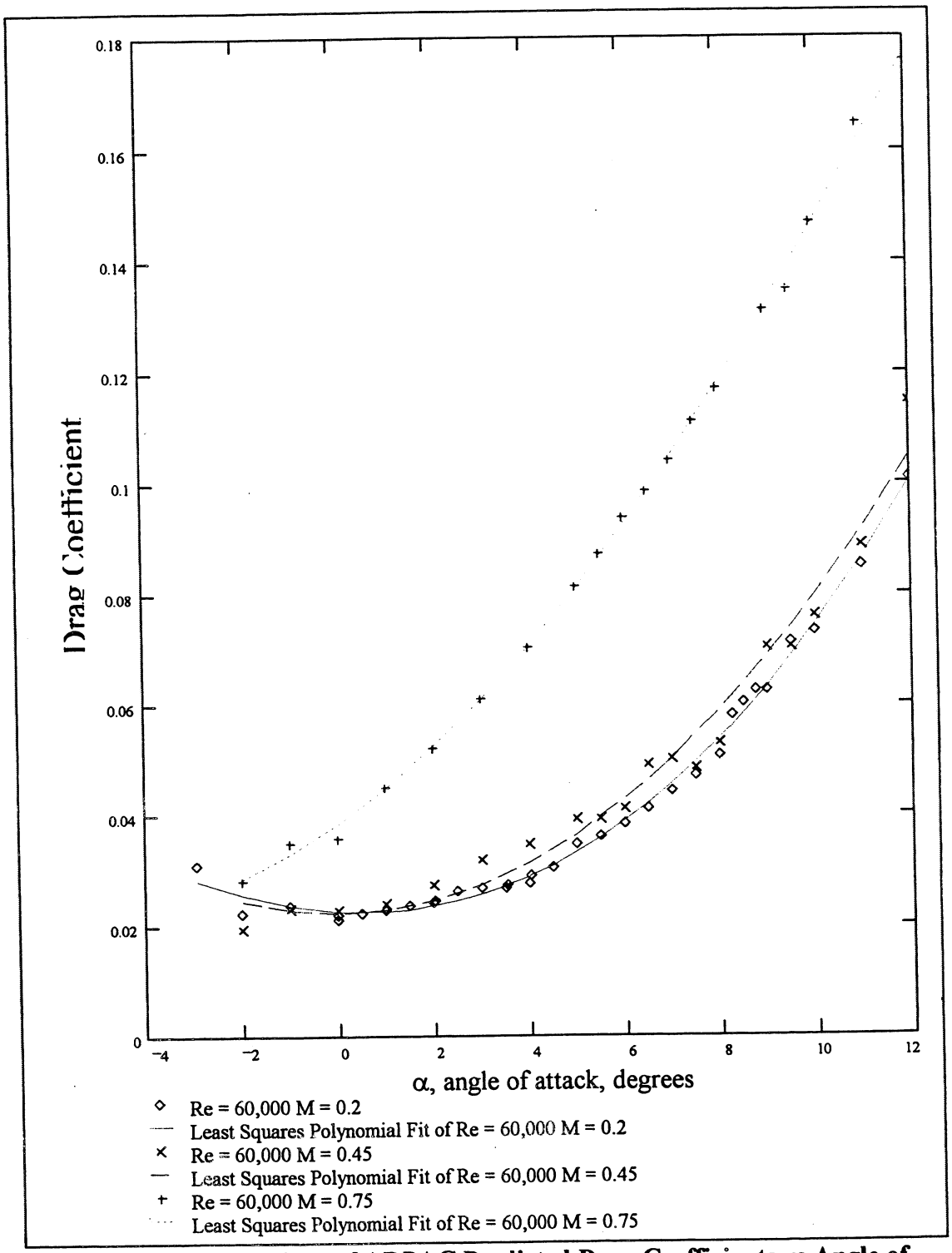

Figure 50: Comparison of ADPAC Predicted Drag Coefficients vs Angle of Attack at Re = 60,000 and M = 0.20, 0.45, 0.75

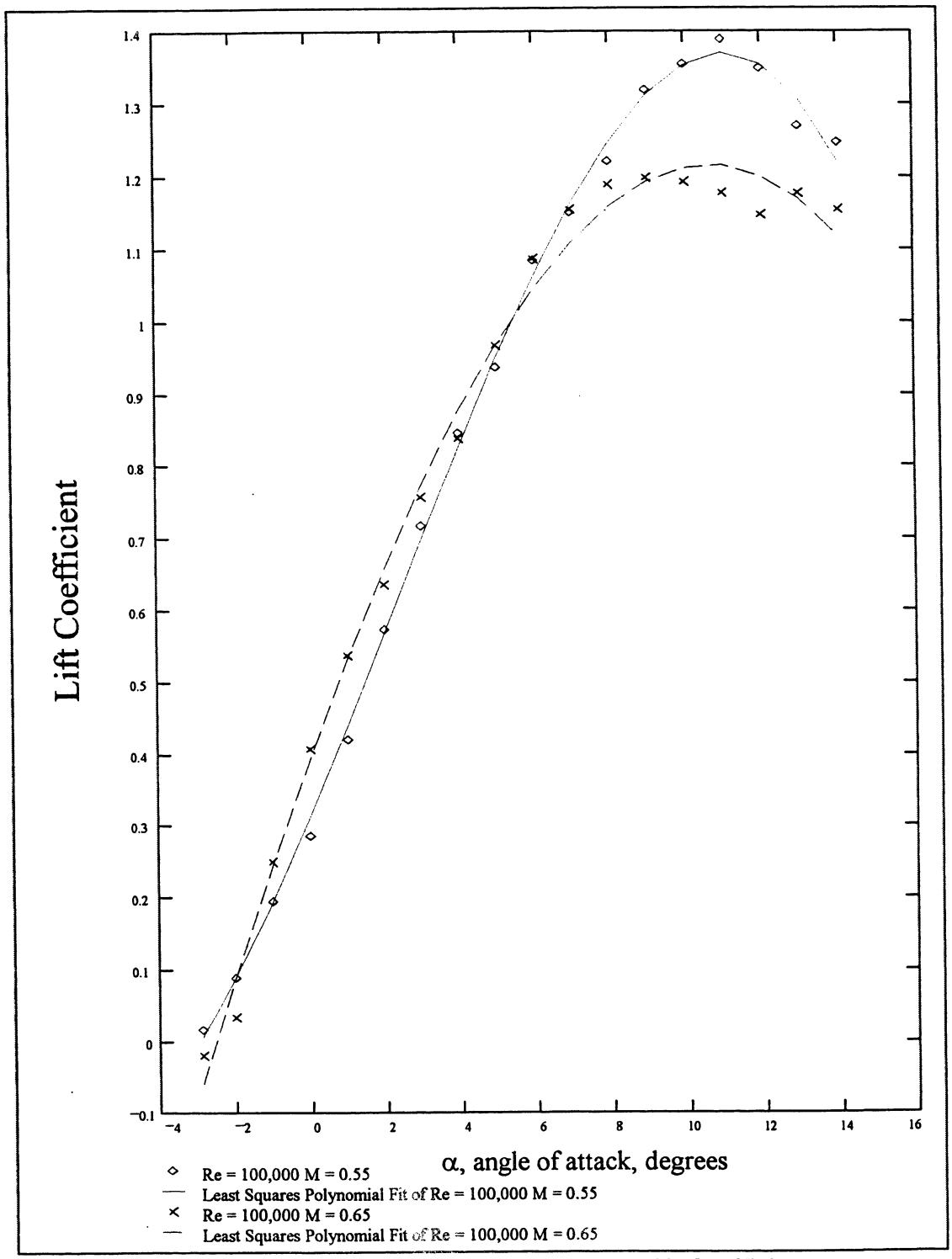

Figure 51: Comparison of ADPAC Predicted Lift Coefficients at Re = 100,000 and M = 0.55, 0.65

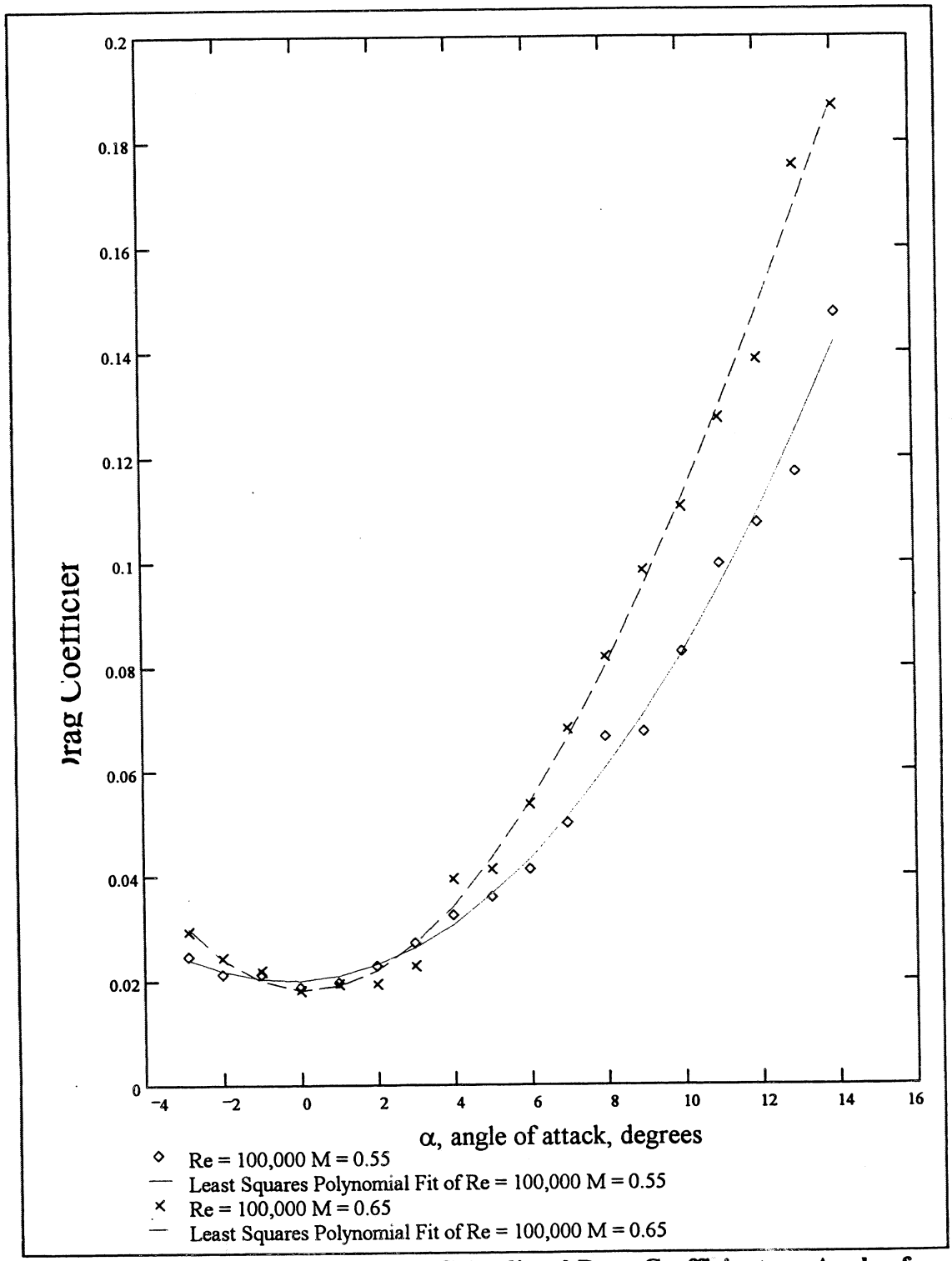

Figure 52: Comparison of ADPAC Predicted Drag Coefficients vs Angle of Attack at Re = 100,000 and M = 0.55, 0.65

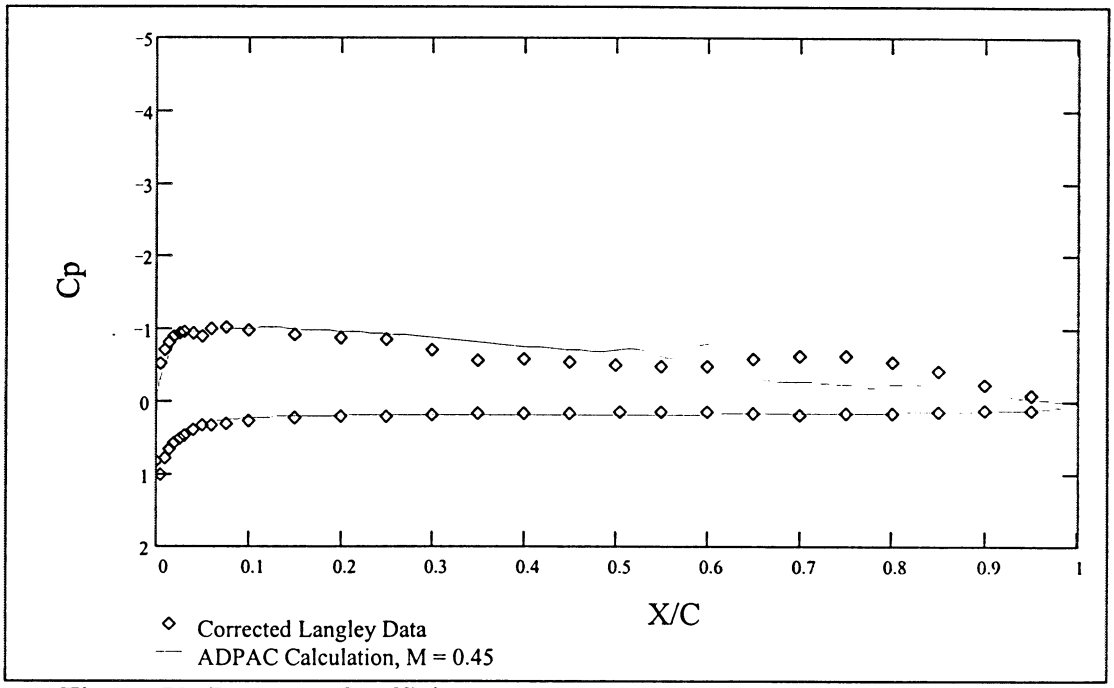

Figure 53: Pressure Coefficient vs. Non-dimensional Chordwise Position, Re = 60,000 α = 4.00°

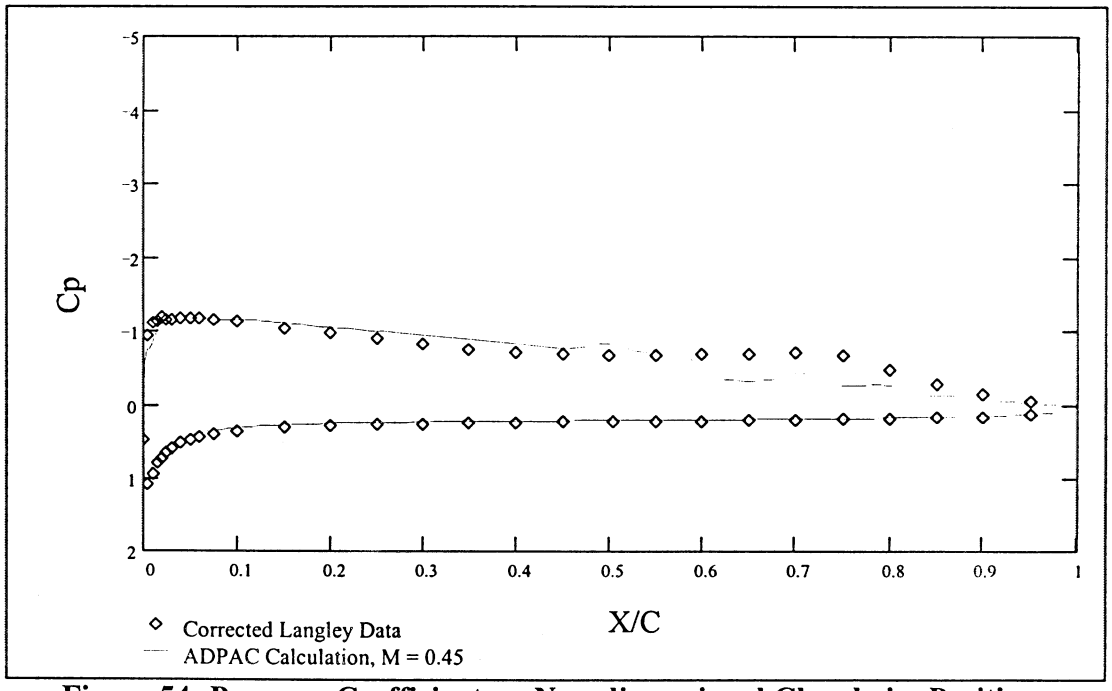

Figure 54: Pressure Coefficient vs. Non-dimensional Chordwise Position, Re = 60,000 α = 4.99°

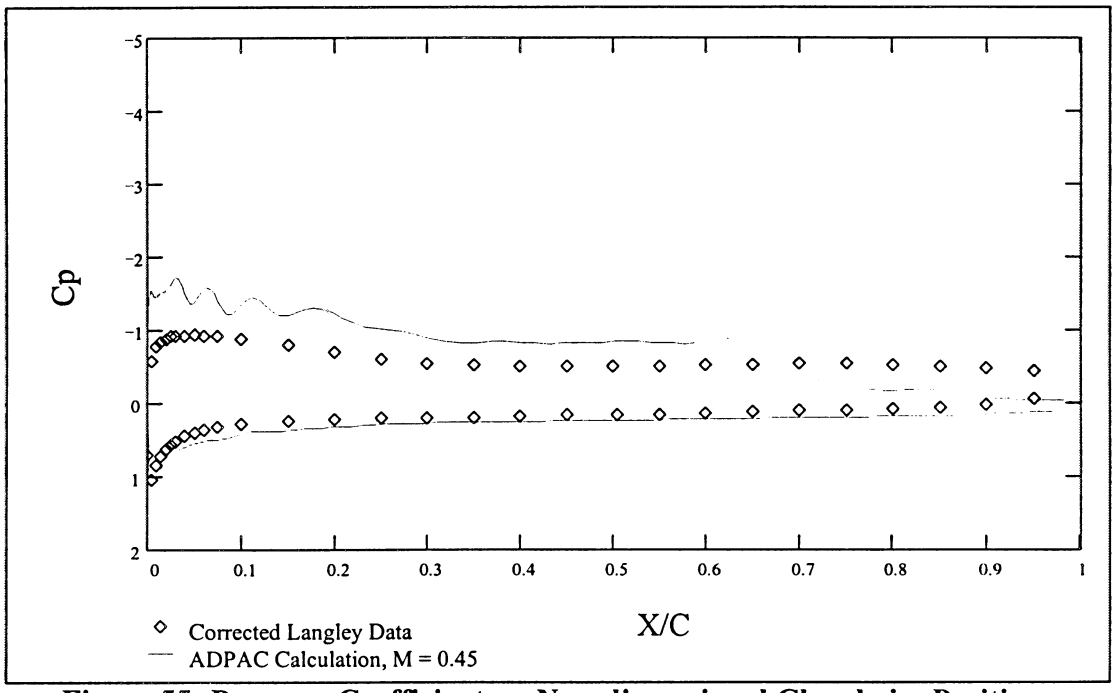

Figure 55: Pressure Coefficient vs. Non-dimensional Chordwise Position, Re = 60,000 α = 6.01°

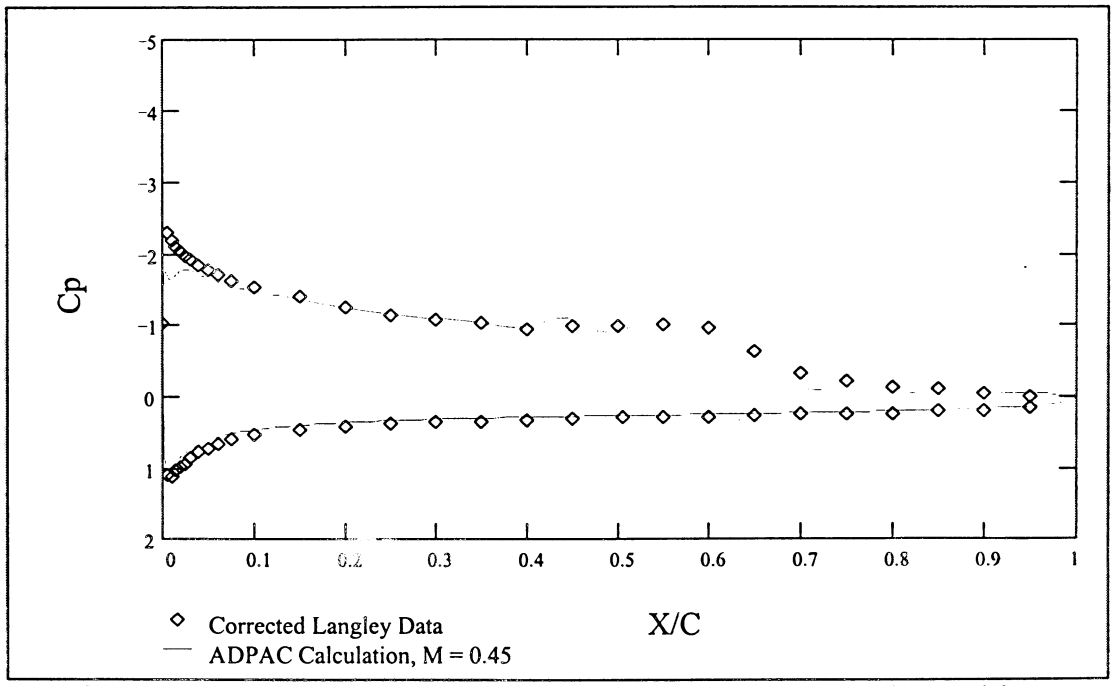

Figure 56: Pressure Coefficient vs. Non-dimensional Chordwise Position, Re = 60,000 α = 7.00°

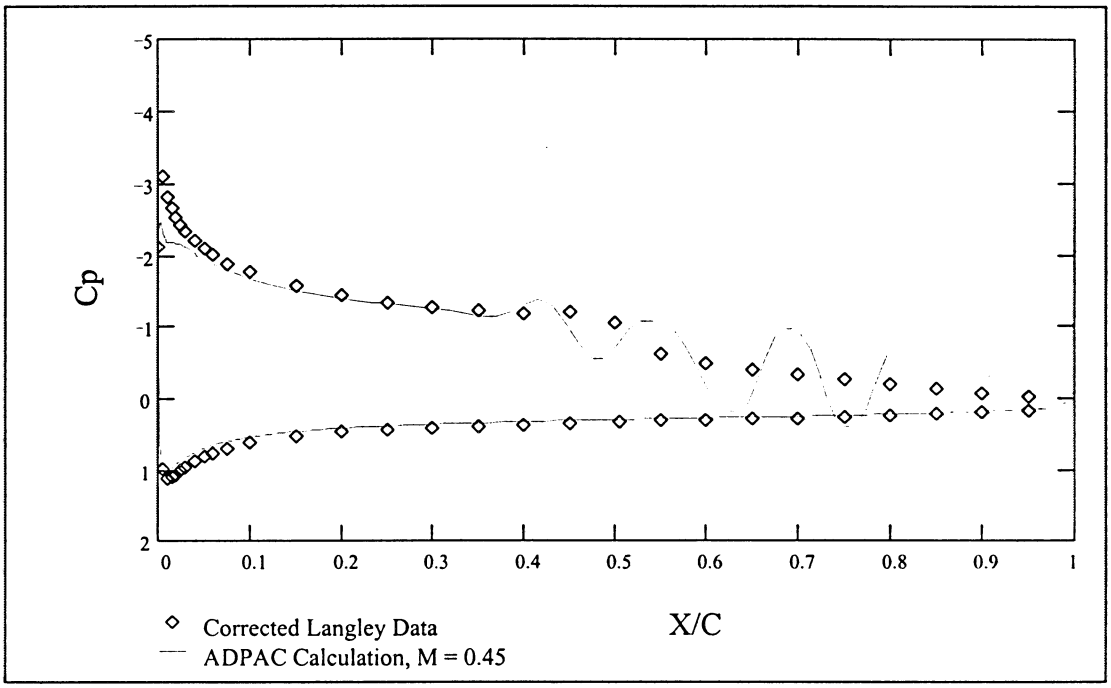

Figure 57 : Pressure Coefficient vs. Non-dimensional Chordwise Position, Re = 60,000 α = 8.01°

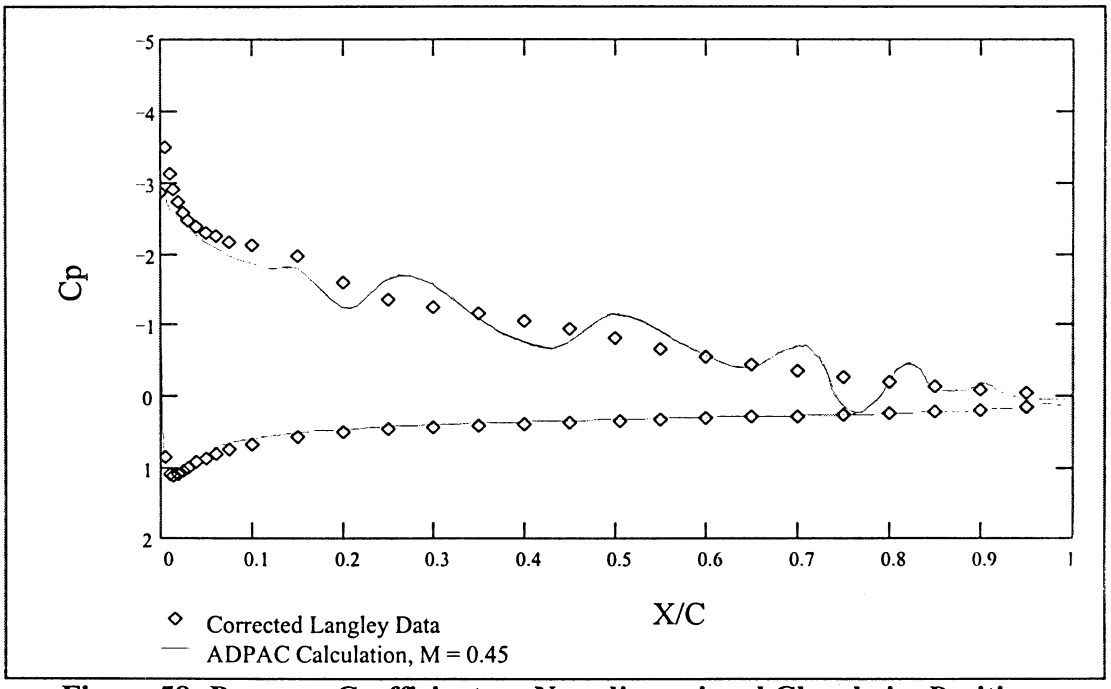

Figure 58: Pressure Coefficient vs. Non-dimensional Chordwise Position, Re = 60,000 α = 9.00°

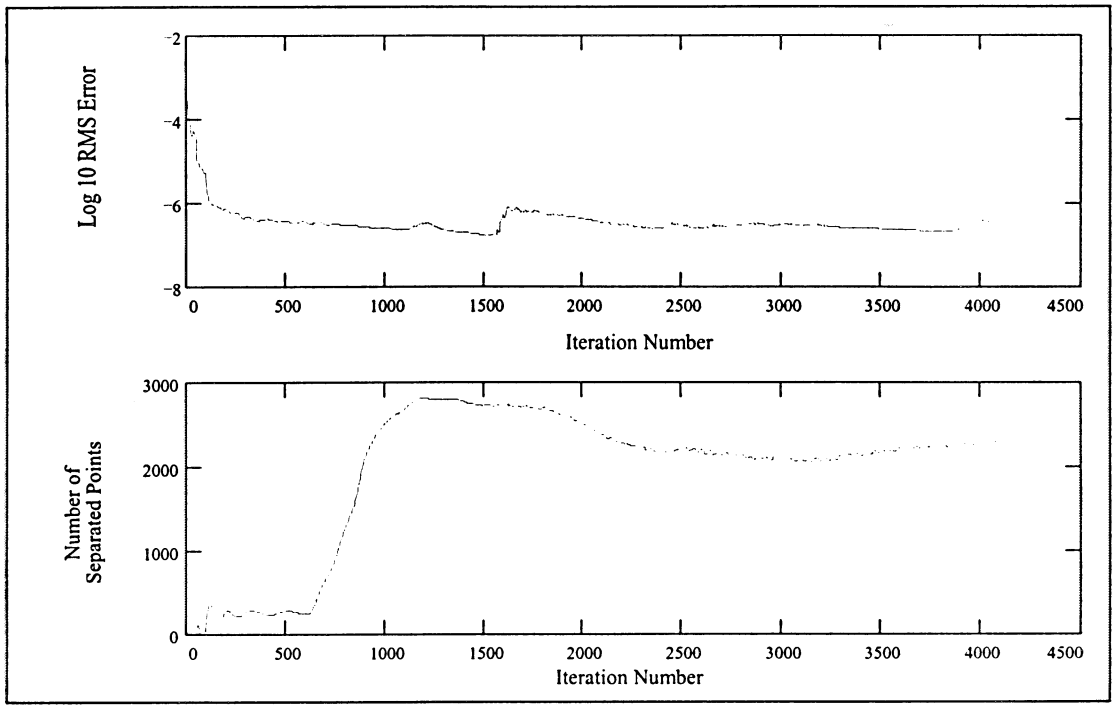

Figure 59: ADPAC Convergence History, Re = 60,000 M = 0.45 α =4.00°

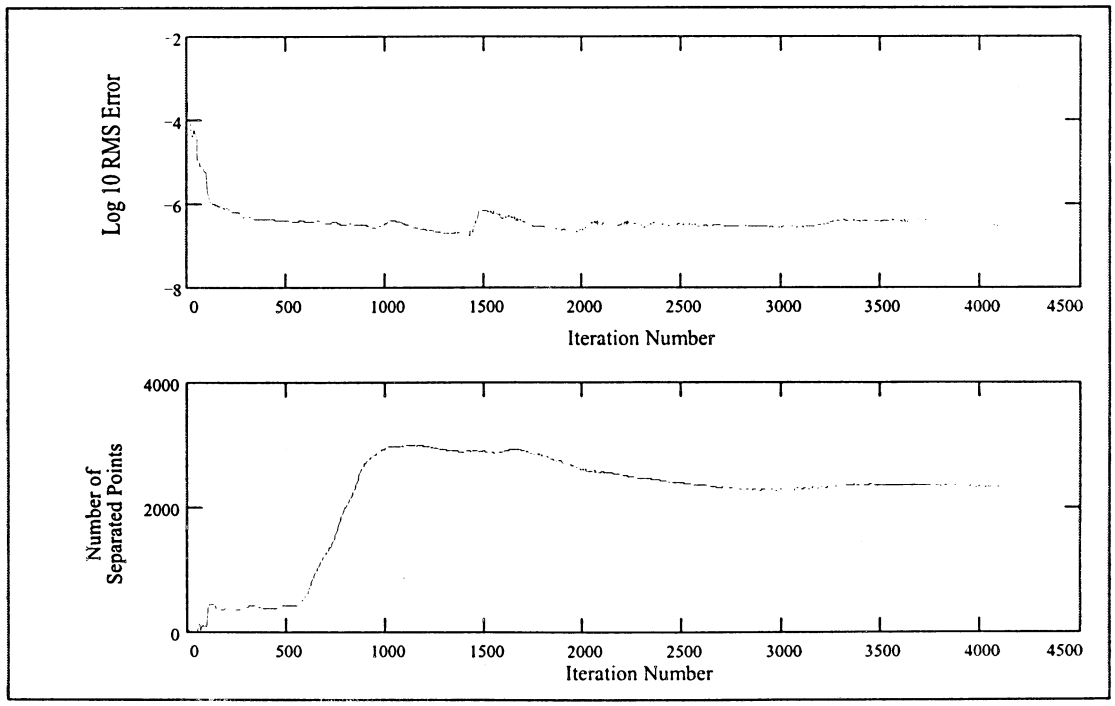

Figure 60: ADPAC Convergence History, Re = 60,000 M = 0.45 α =4.99°

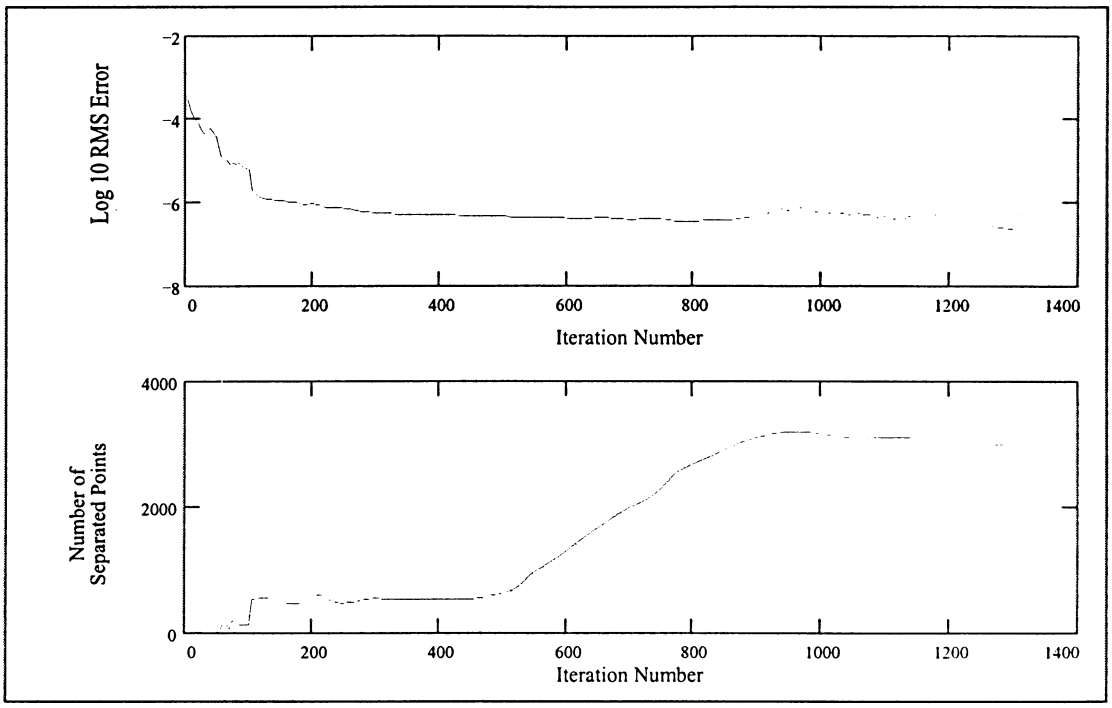

Figure 61: ADPAC Convergence History, Re = 60,000 M = 0.45 α =6.01°

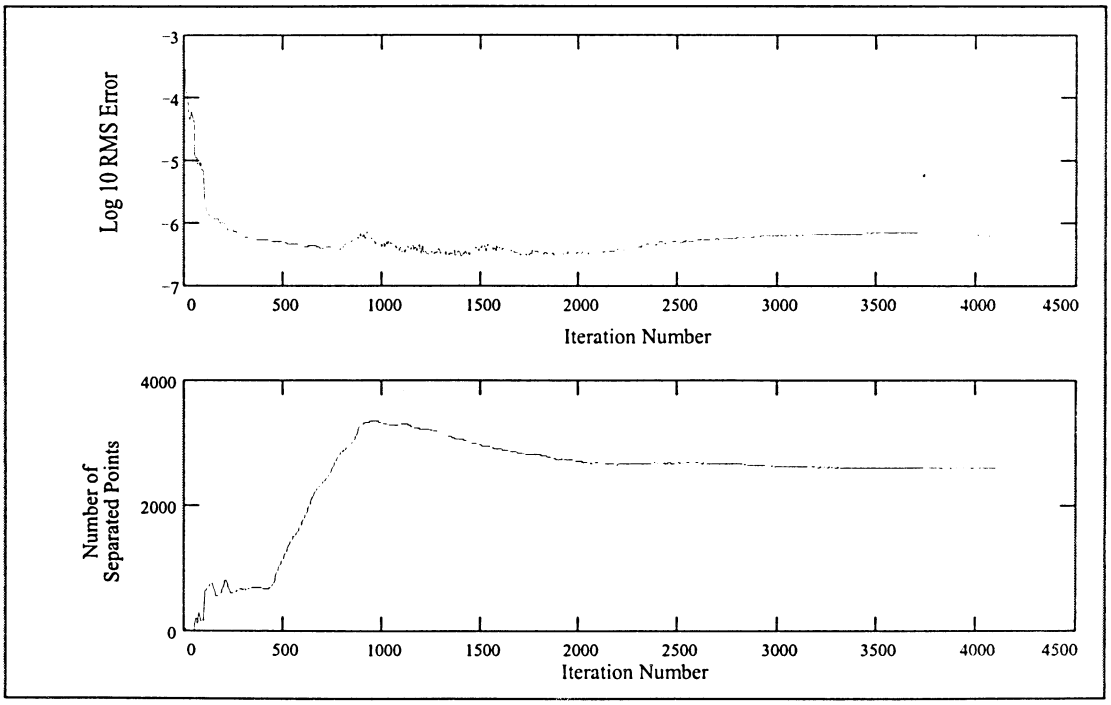

Figure 62: ADPAC Convergence History, Re = 60,000 M = 0.45 α =7.00°

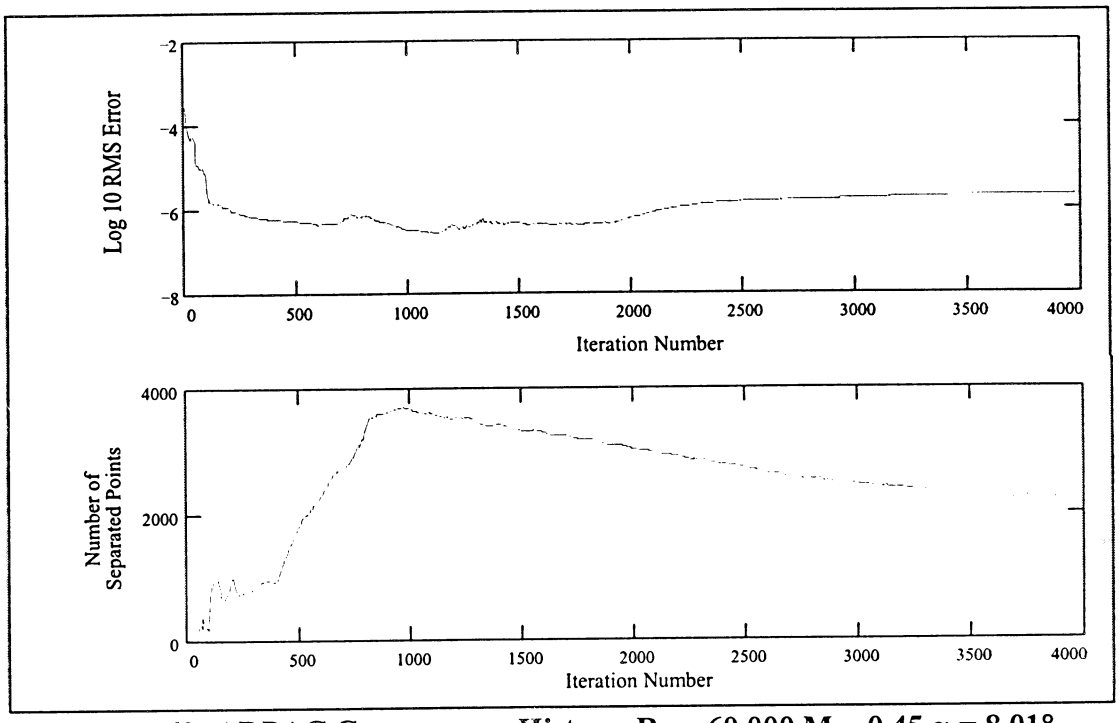

Figure 63: ADPAC Convergence History, Re = 60,000 M = 0.45 α = 8.01°

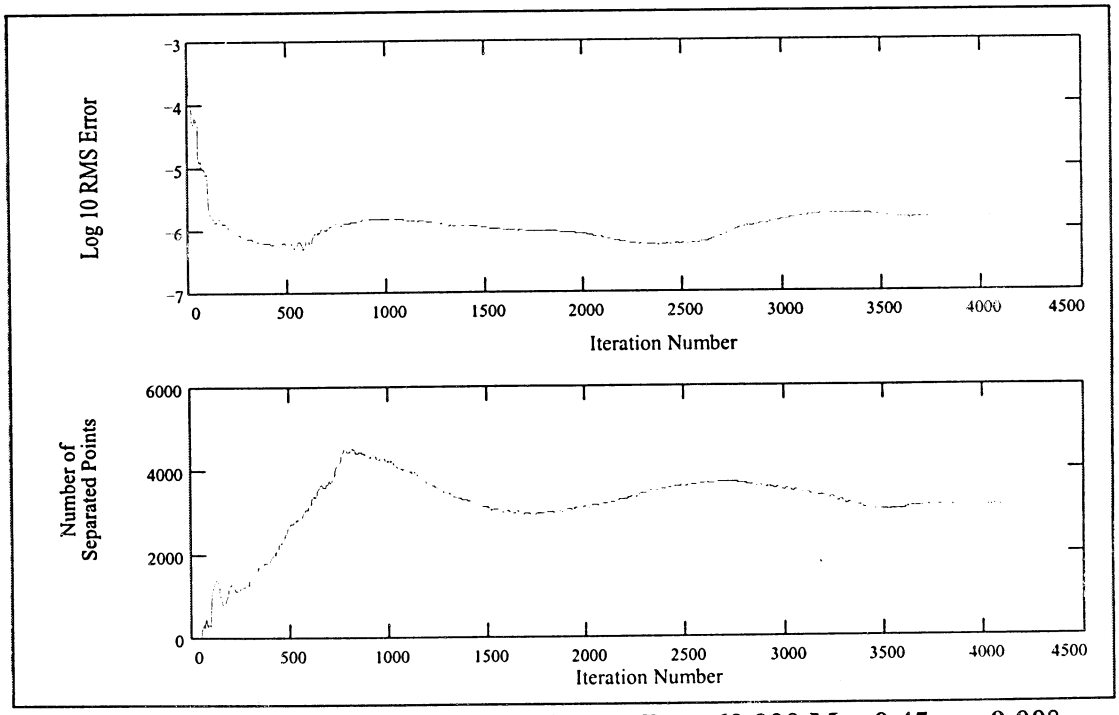

Figure 64: ADPAC Convergence History, Re = 60,000 M = 0.45 α = 9.00°

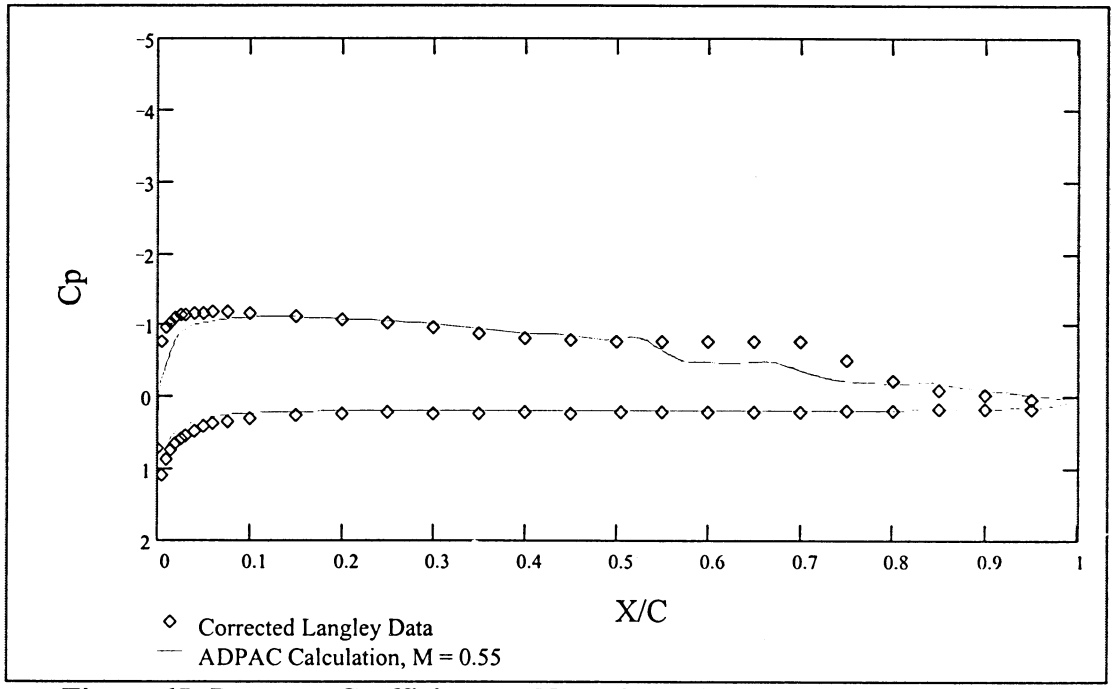

Figure 65: Pressure Coefficient vs. Non-dimensional Chordwise Position, Re = 100,000 α = 4.00°

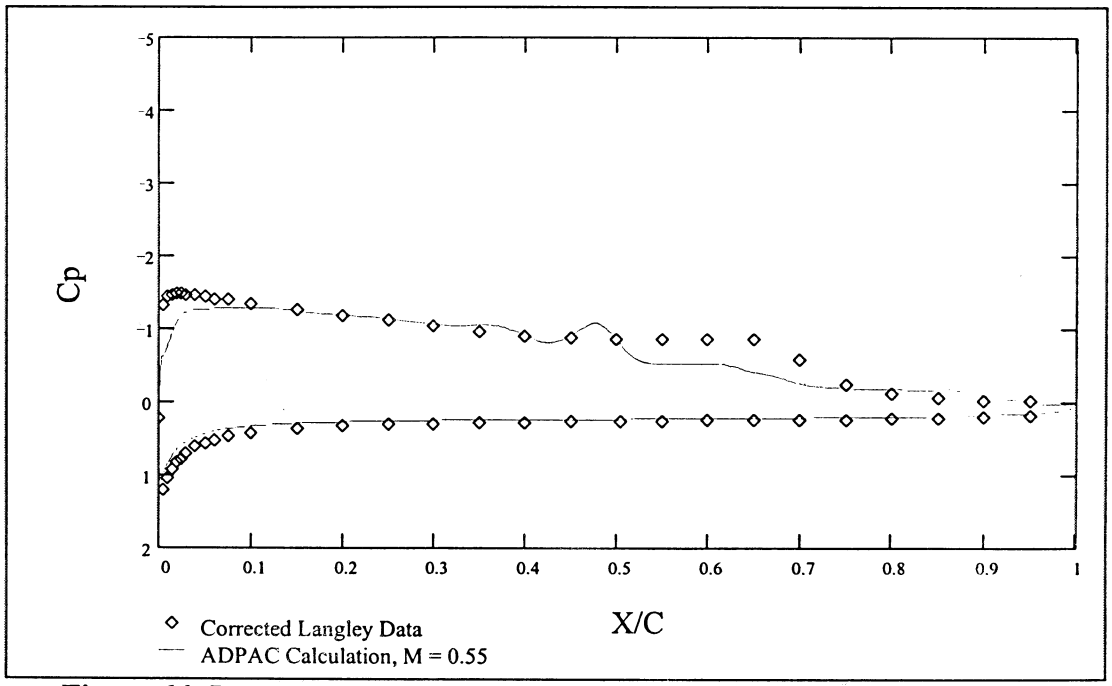

Figure 66: Pressure Coefficient vs. Non-dimensional Chordwise Position, Re = 100,000 α = 5.01°

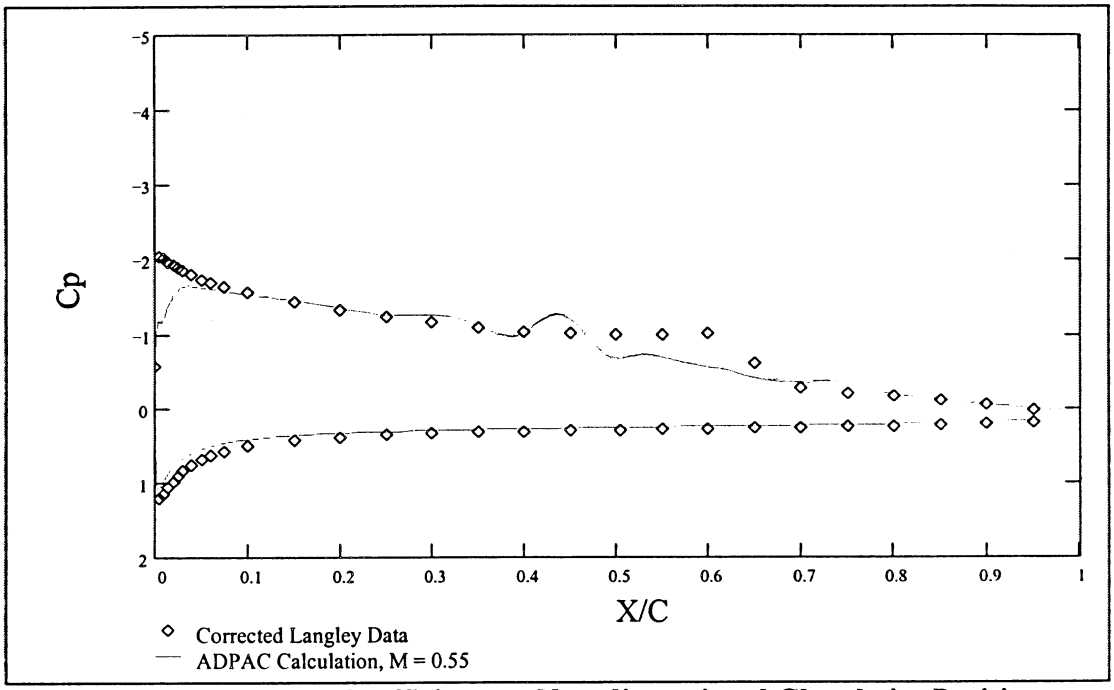

Figure 67: Pressure Coefficient vs. Non-dimensional Chordwise Position, Re = 100,000 α = 6.00°

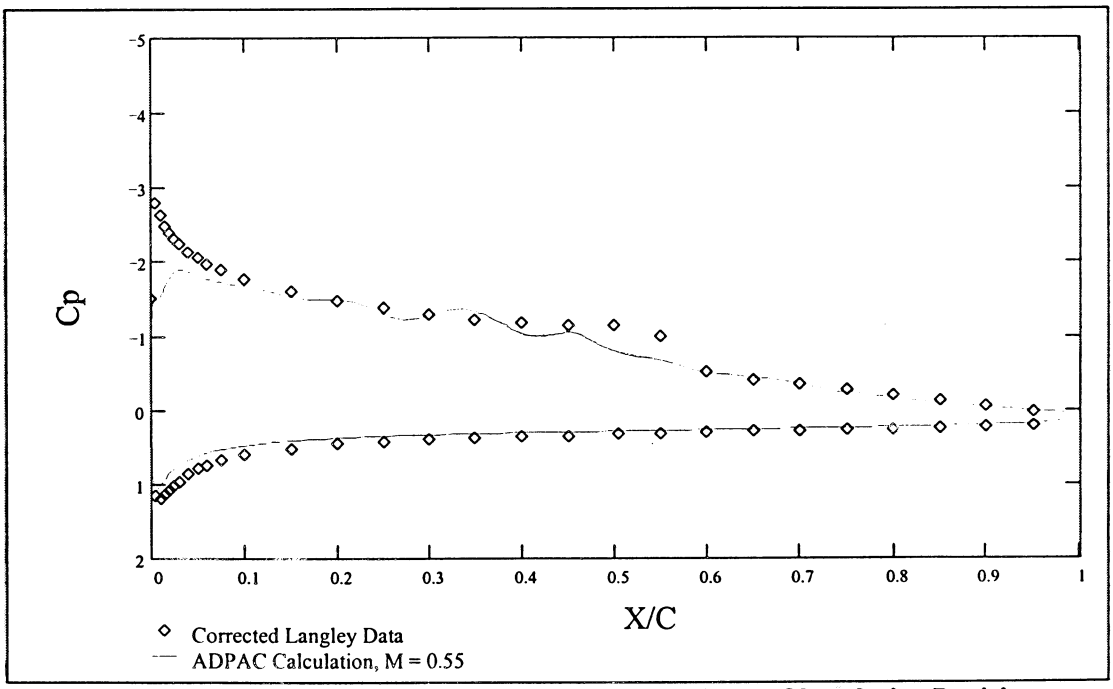

Figure 68: Pressure Coefficient vs. Non-dimensional Chordwise Position, Re = 100,000 α = 7.00°

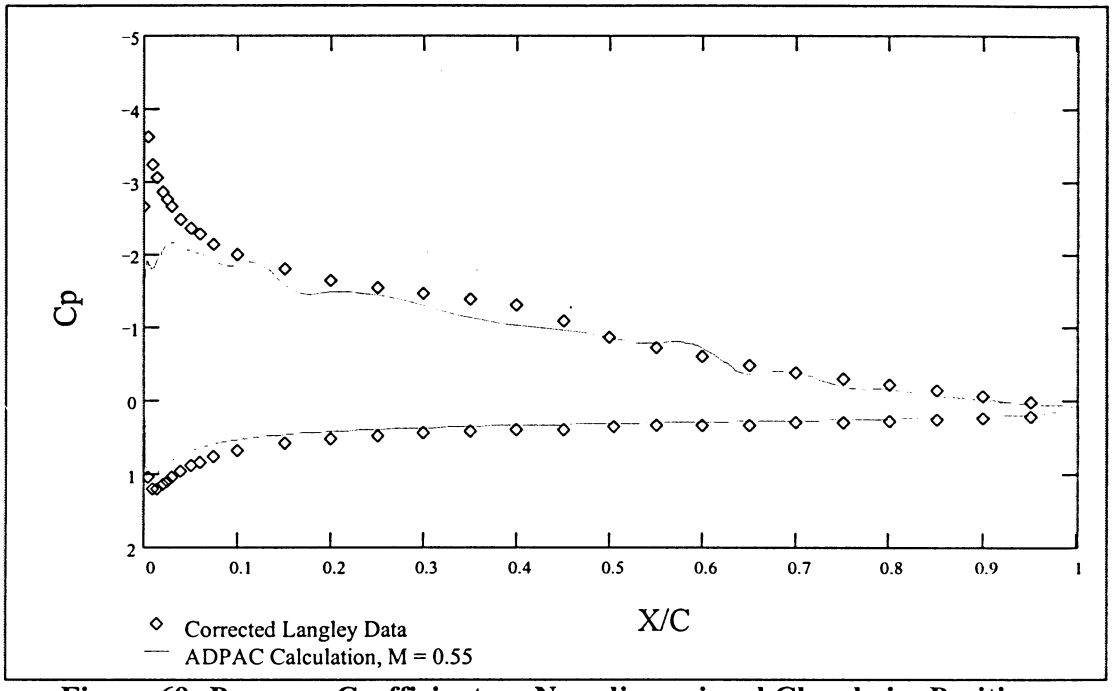

Figure 69: Pressure Coefficient vs. Non-dimensional Chordwise Position, Re = 100,000 α = 8.00°

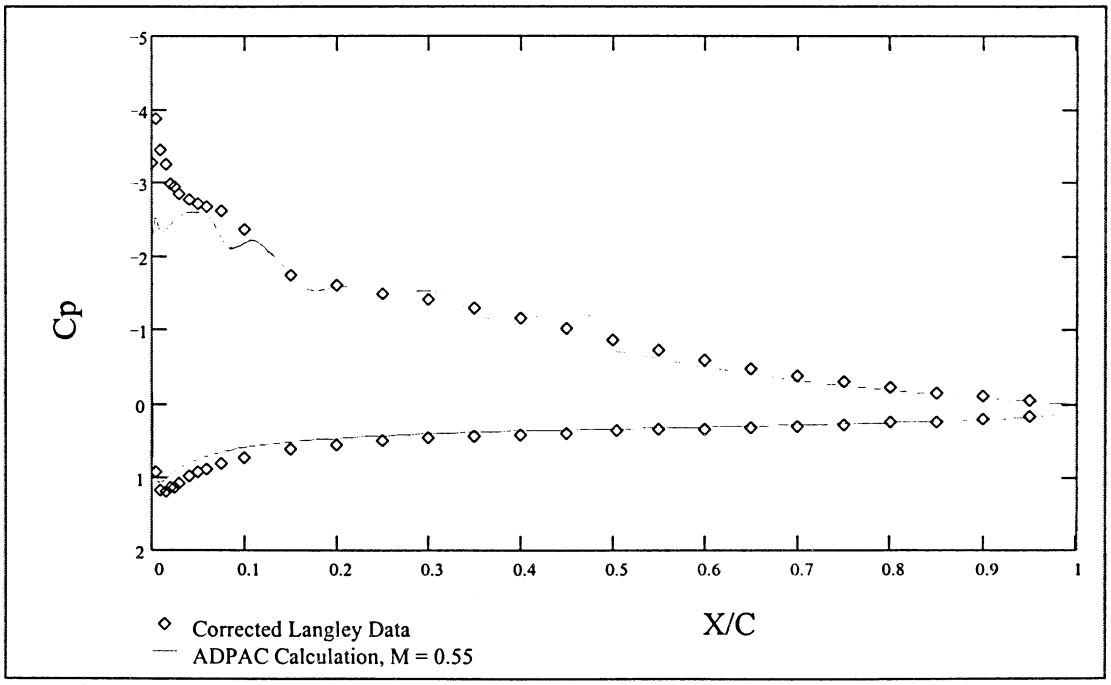

Figure 70: Pressure Coefficient vs. Non-dimensional Chordwise Position, Re = 100,000 α = 9.00°

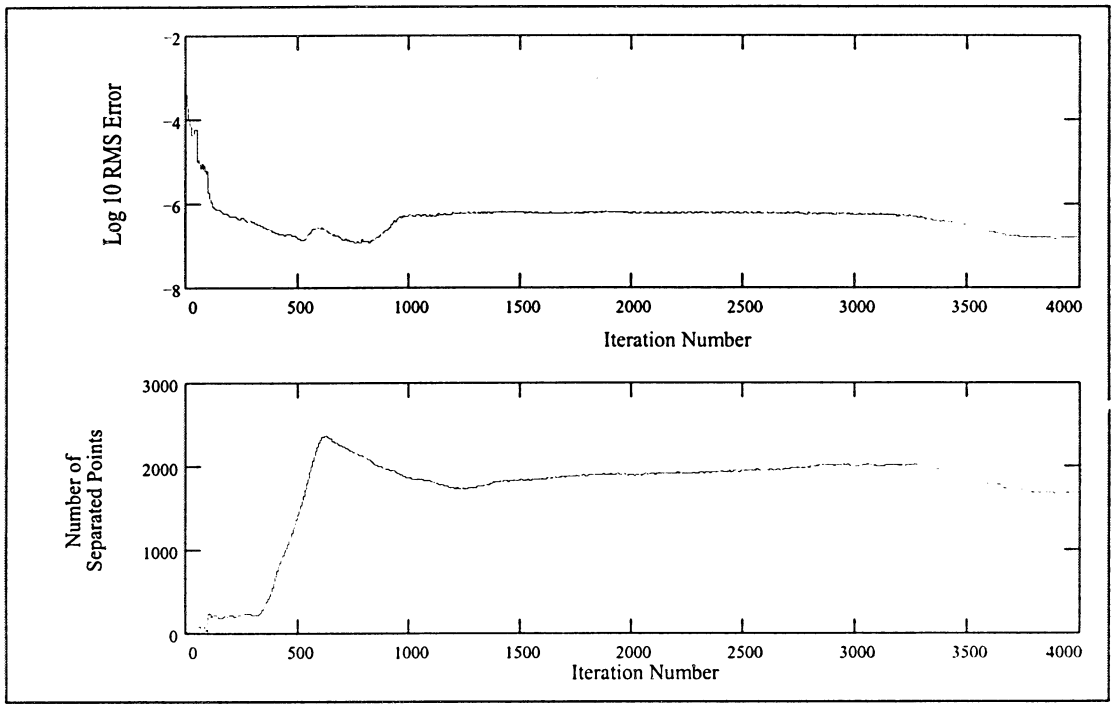

Figure 71: ADPAC Convergence History, Re = 100,000 M = 0.55 α = 4.00°

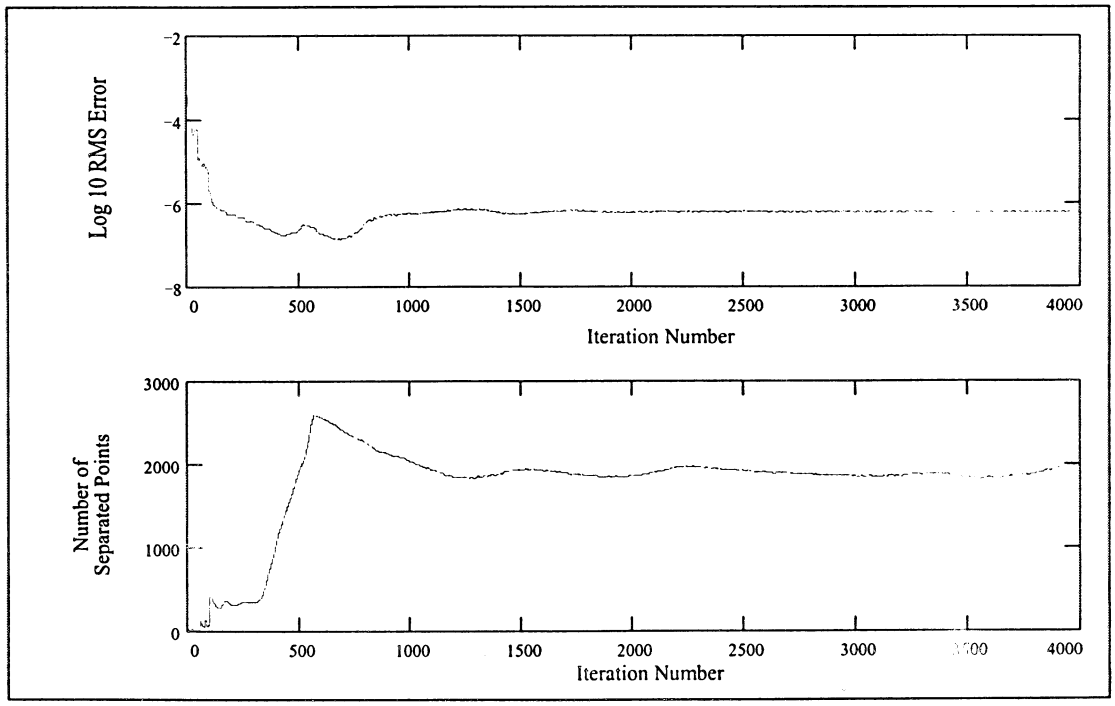

Figure 72: ADPAC Convergence History, Re = 100,000 M = 0.55 α = 5.01°

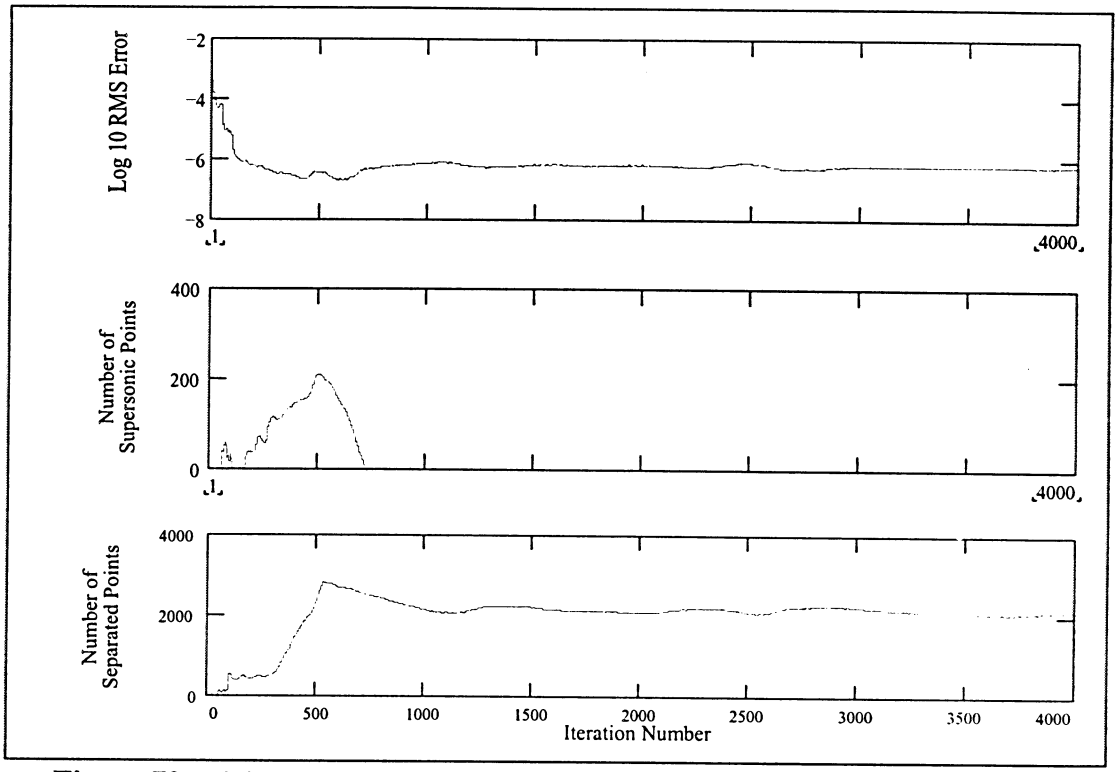

Figure 73: ADPAC Convergence History, Re = 100,000 M = 0.55 α = 6.00°

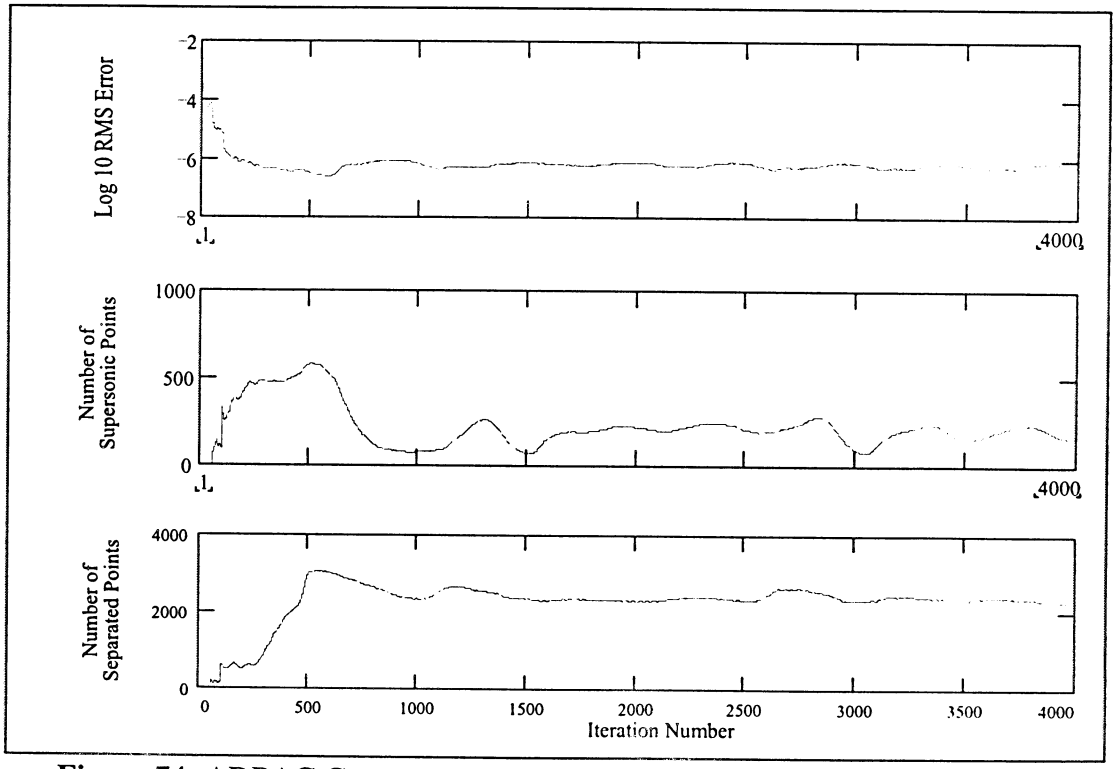

Figure 74: ADPAC Convergence History, Re = 100,000 M = 0.55 α = 7.00°

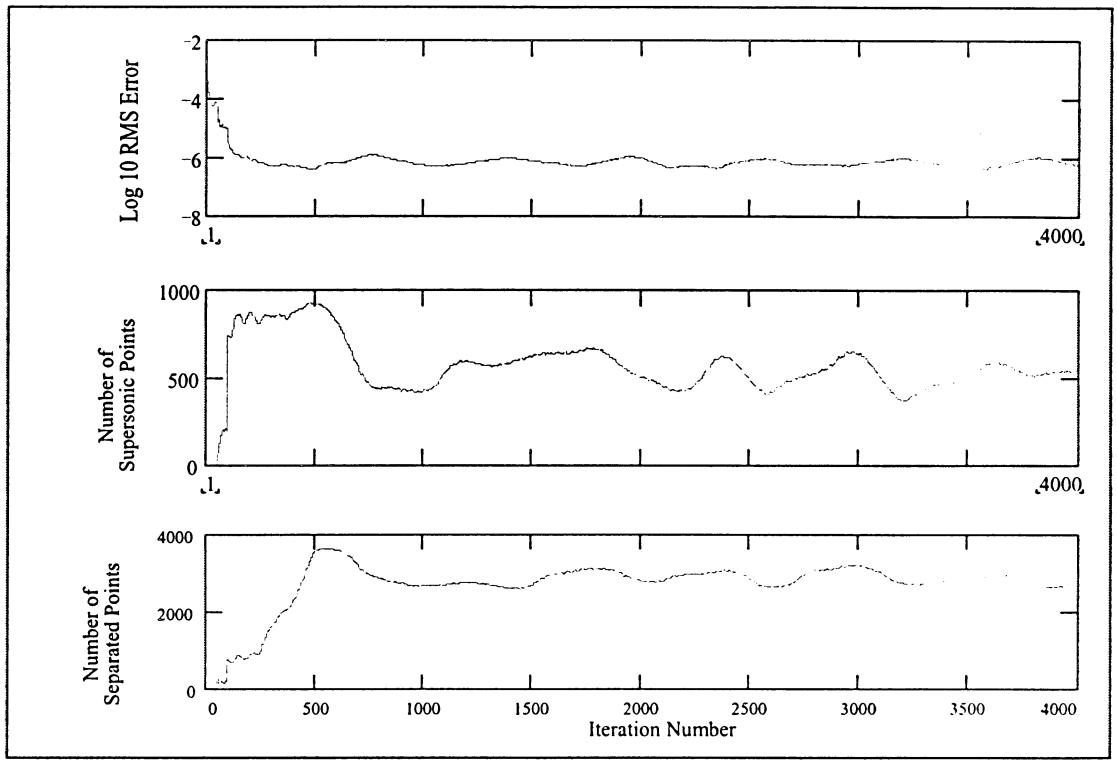

Figure 75: ADPAC Convergence History, Re = 100,000 M = 0.55 α = 8.00°

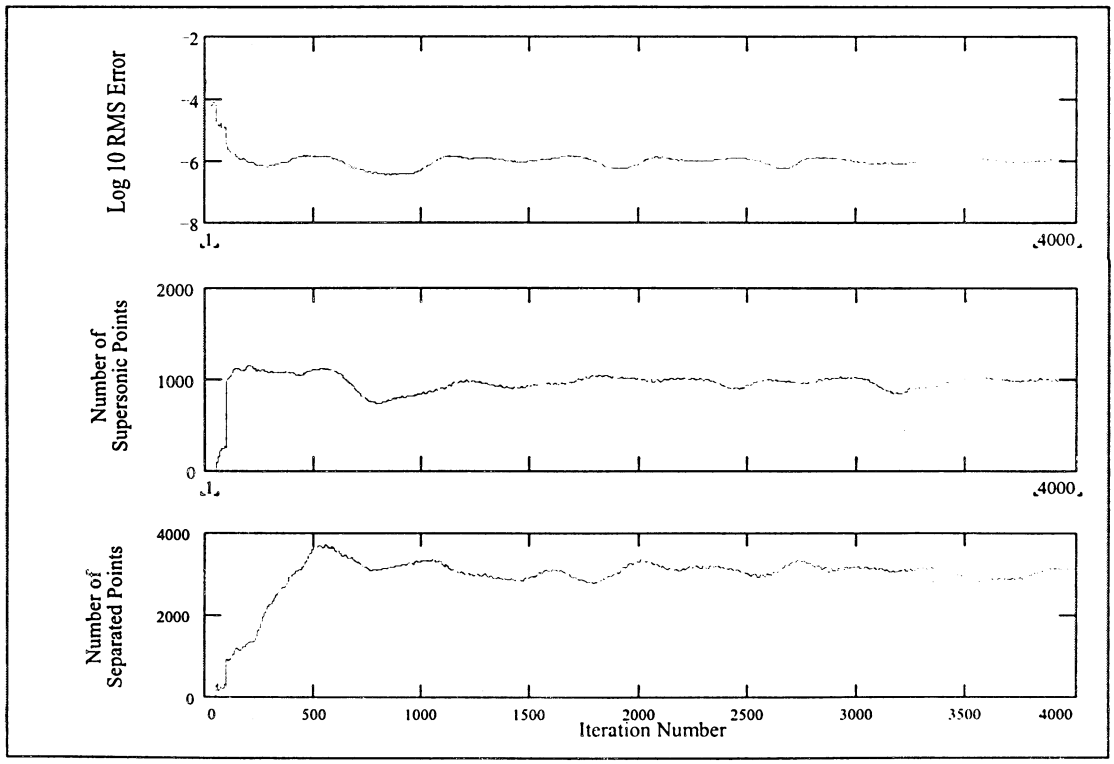

Figure 76: ADPAC Convergence History, Re = 100,000 M = 0.55 α = 9.00°

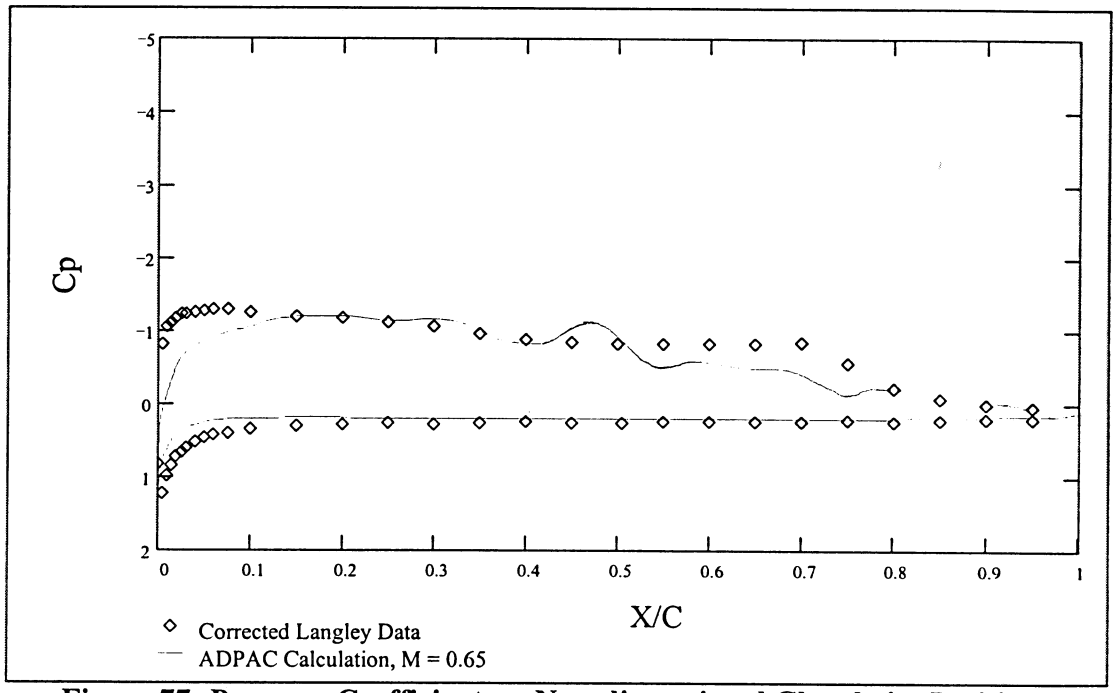

Figure 77: Pressure Coefficient vs. Non-dimensional Chordwise Position, Re = 100,000 α = 4.00°

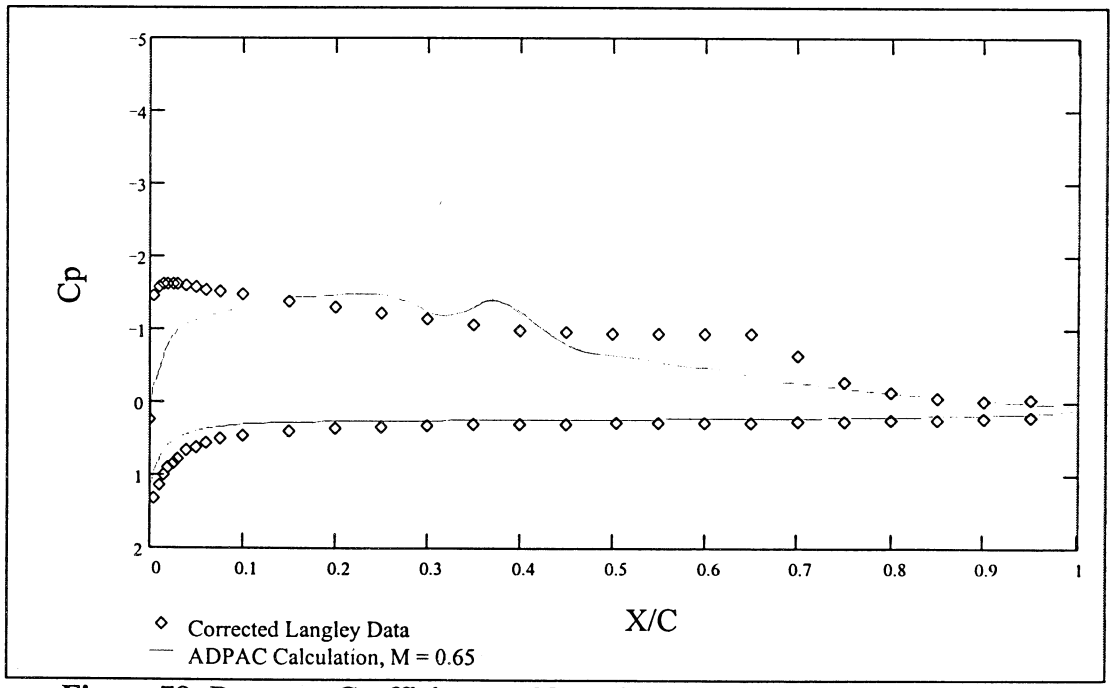

Figure 78: Pressure Coefficient vs. Non-dimensional Chordwise Position, Re = 100,000 α = 5.01°

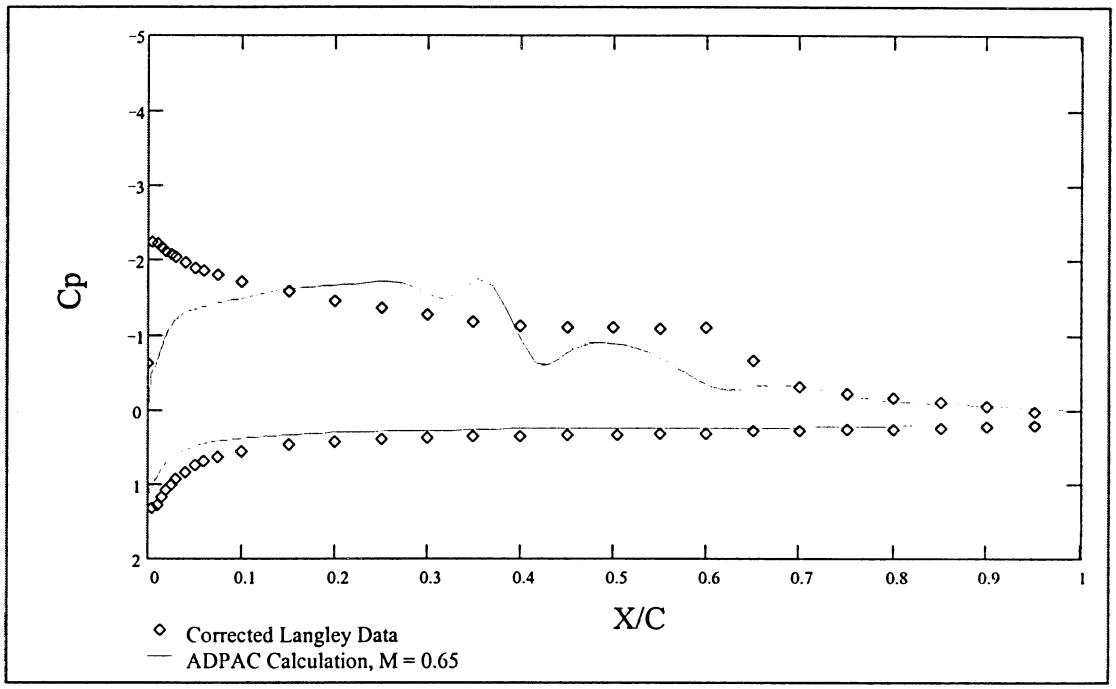

Figure 79: Pressure Coefficient vs. Non-dimensional Chordwise Position, Re = 100,000 α = 6.00°

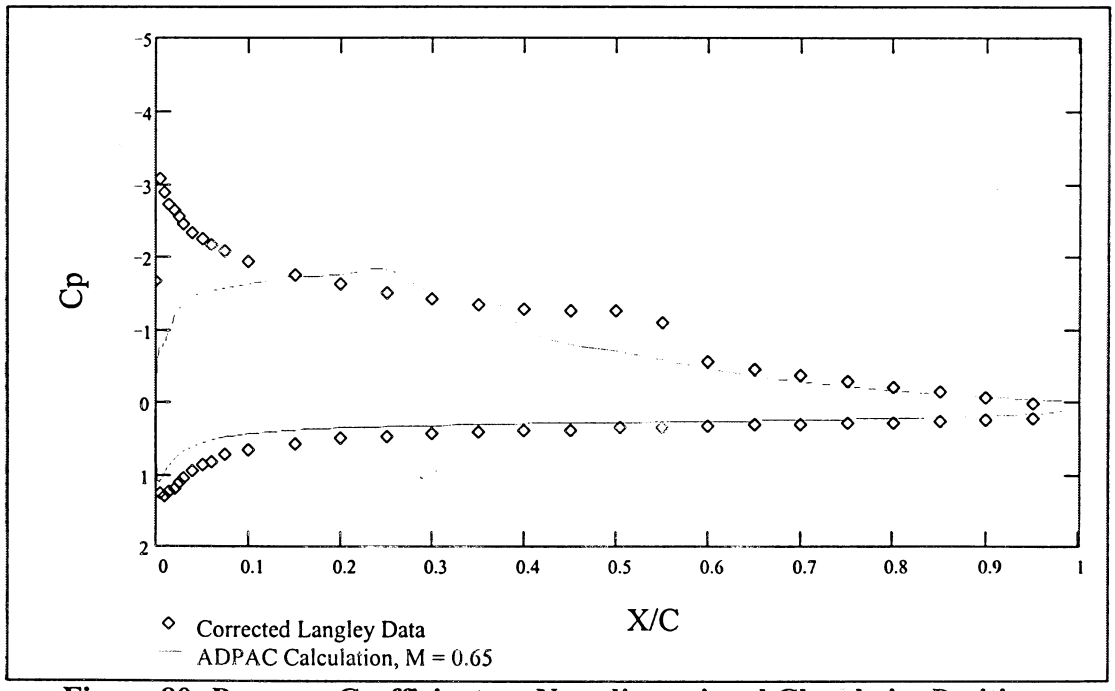

Figure 80: Pressure Coefficient vs. Non-dimensional Chordwise Position, Re = 100,000 α = 7.00°

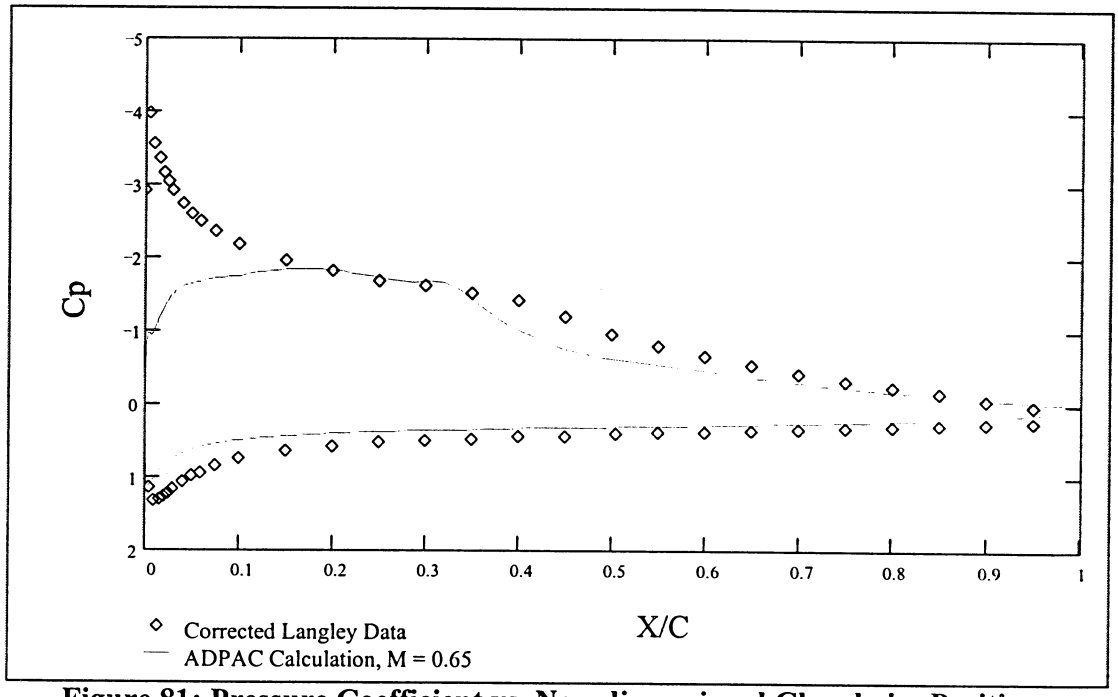

Figure 81: Pressure Coefficient vs. Non-dimensional Chordwise Position, Re = 100,000 α = 8.00°

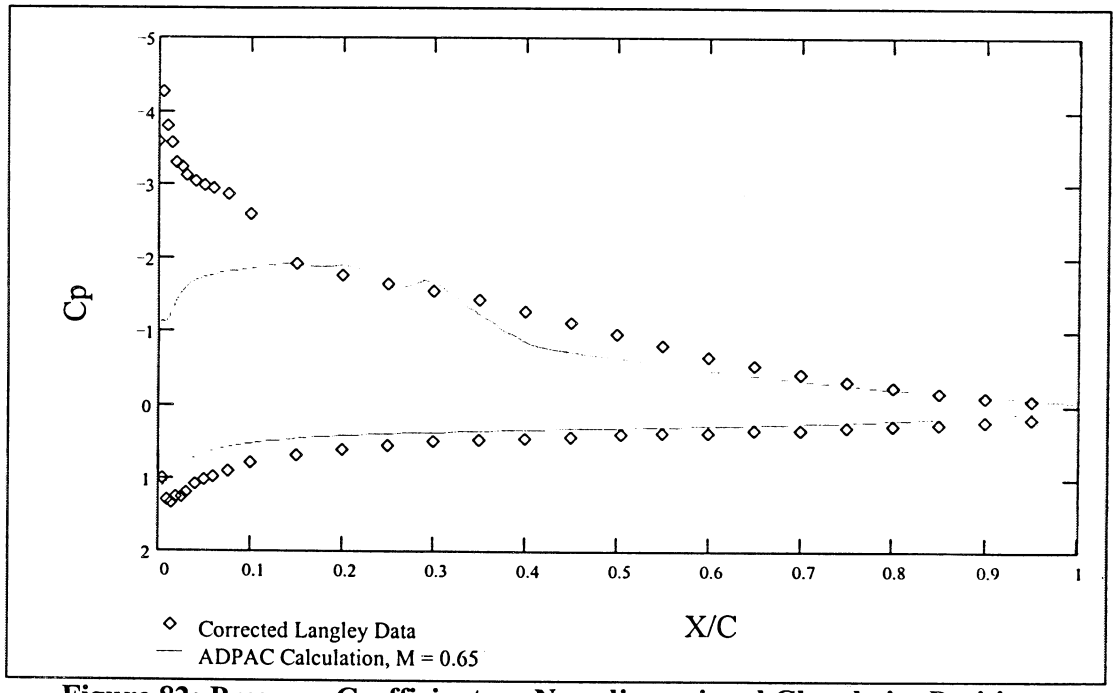

Figure 82: Pressure Coefficient vs. Non-dimensional Chordwise Position, Re = 100,000 α = 9.00°

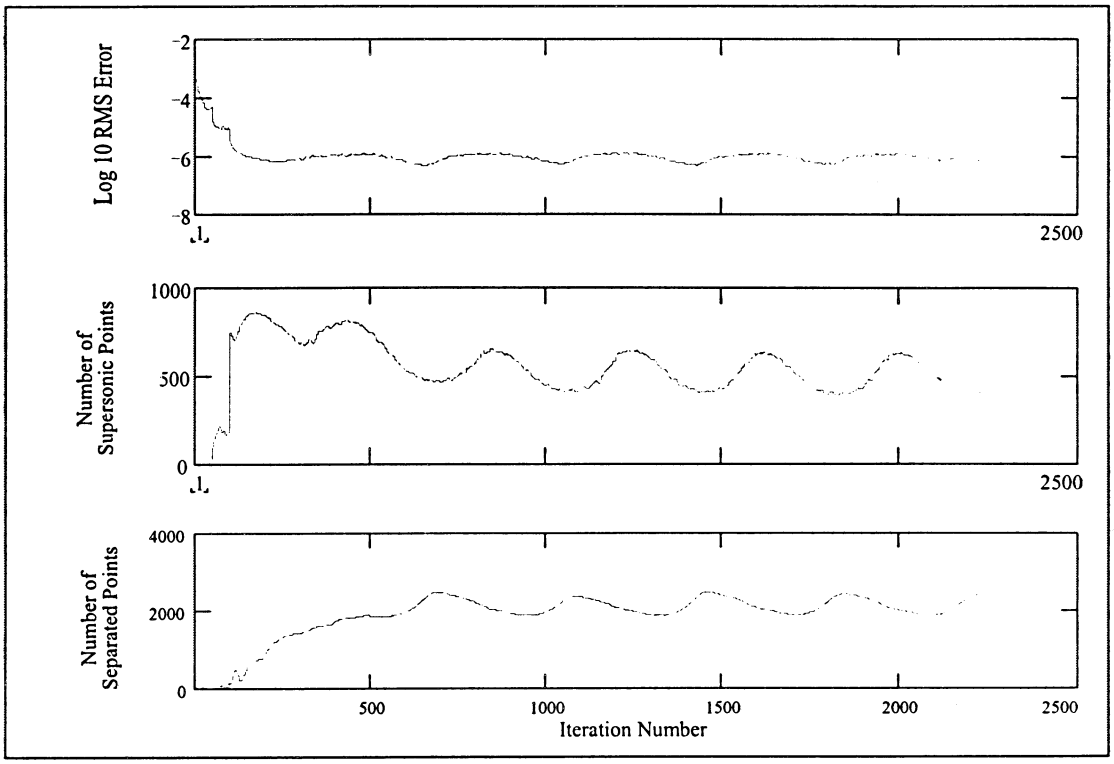

Figure 83: ADPAC Convergence History, Re = 100,000 M = 0.65 α = 4.00°

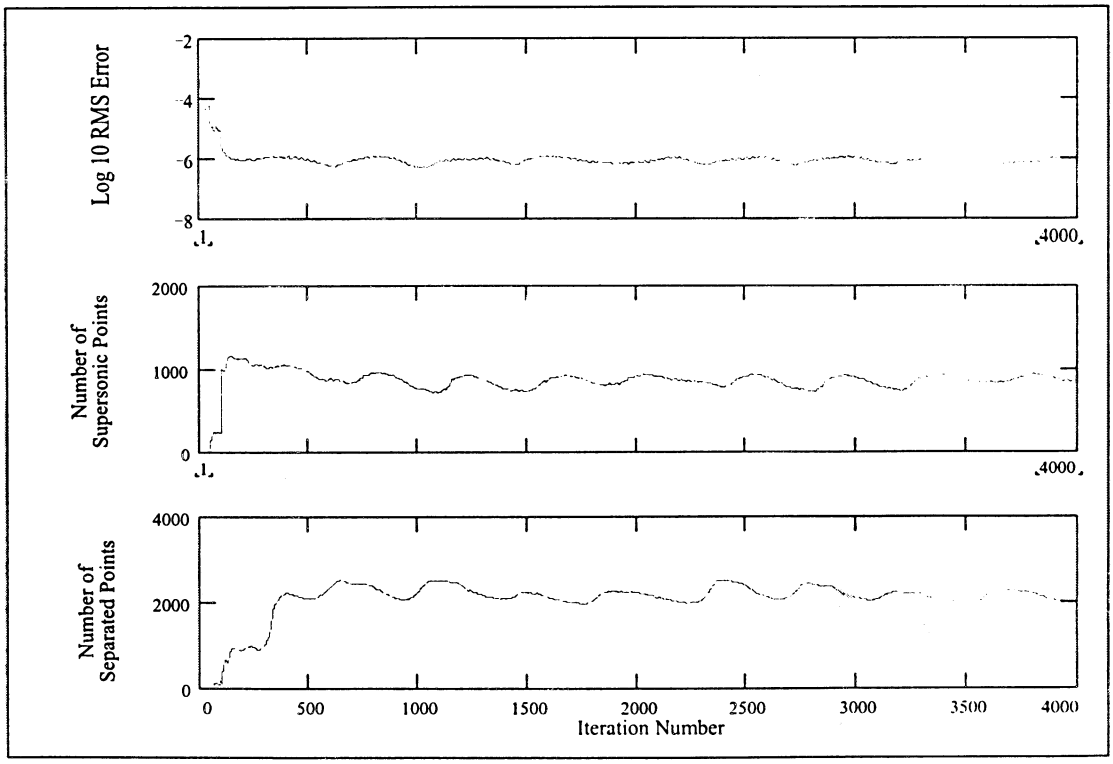

Figure 84: ADPAC Convergence History, Re = 100,000 M = 0.65 α = 5.01°

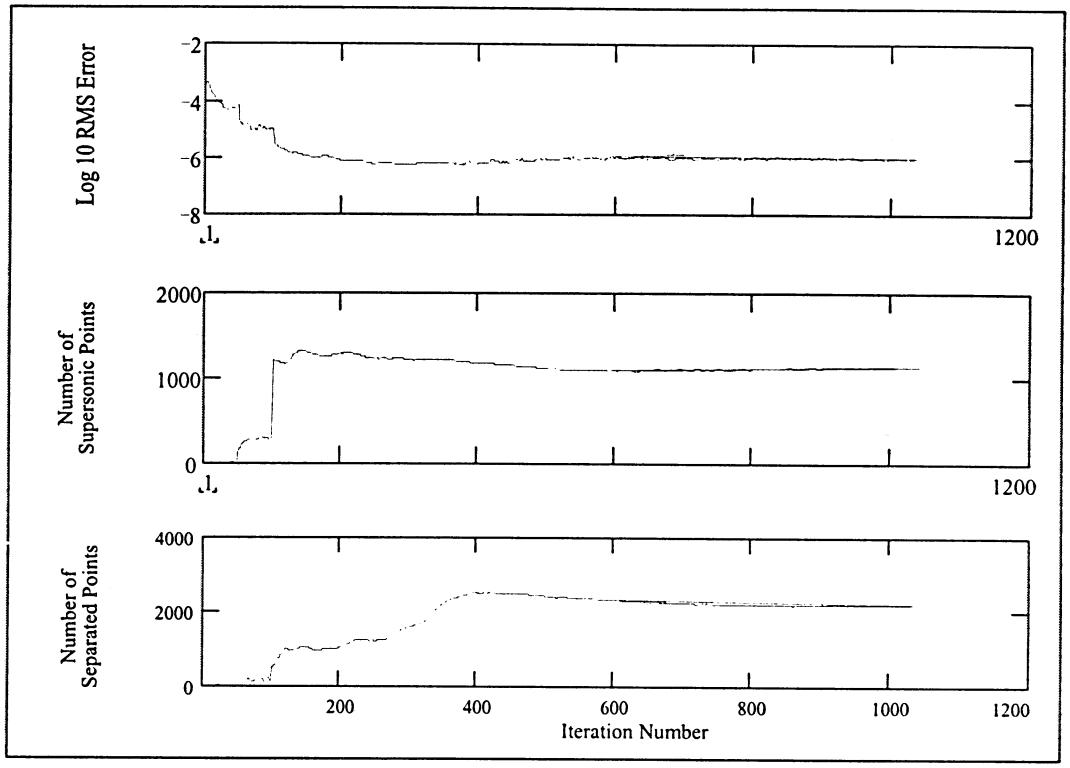

Figure 85: ADPAC Convergence History, Re = 100,000 M = 0.65 α = 6.00°

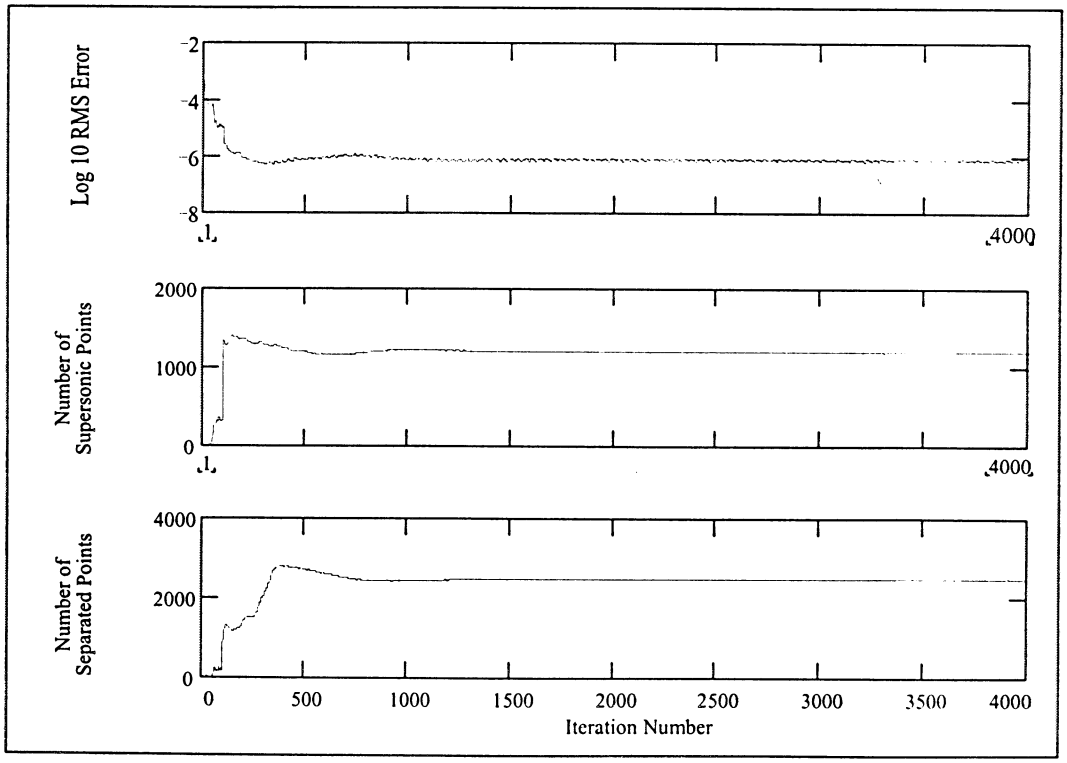

Figure 86: ADPAC Convergence History, Re = 100,000 M = 0.65 α = 7.00°

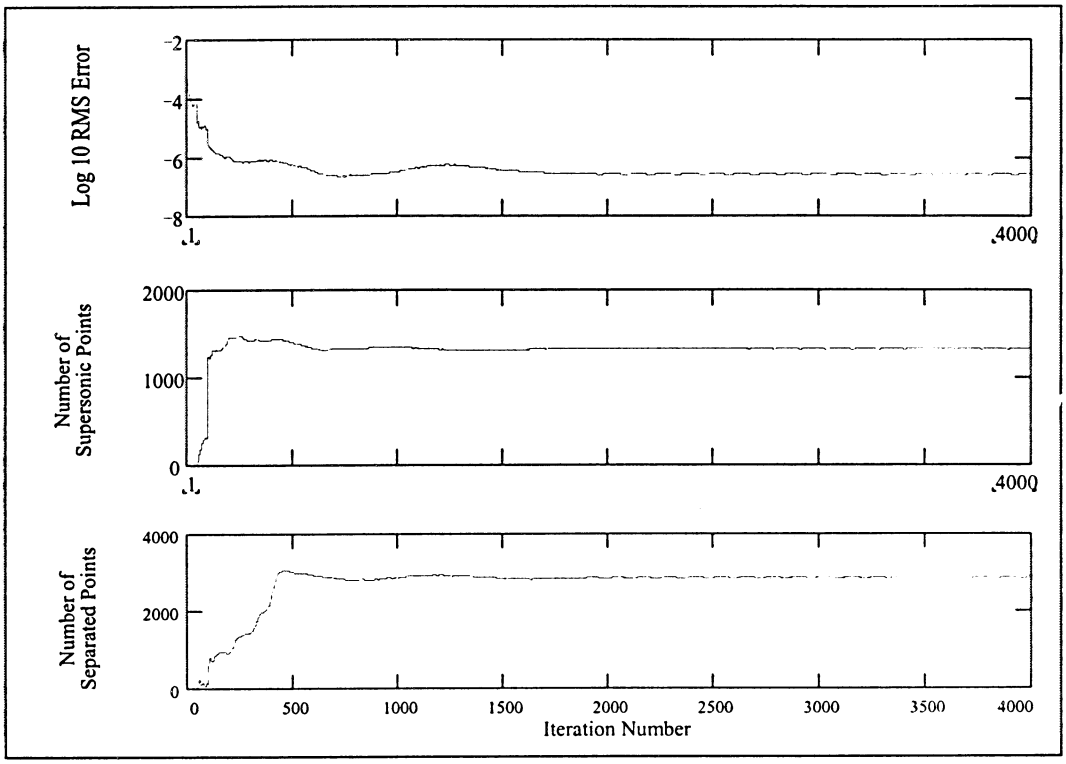

Figure 87: ADPAC Convergence History, Re = 100,000 M = 0.65 α = 8.00°

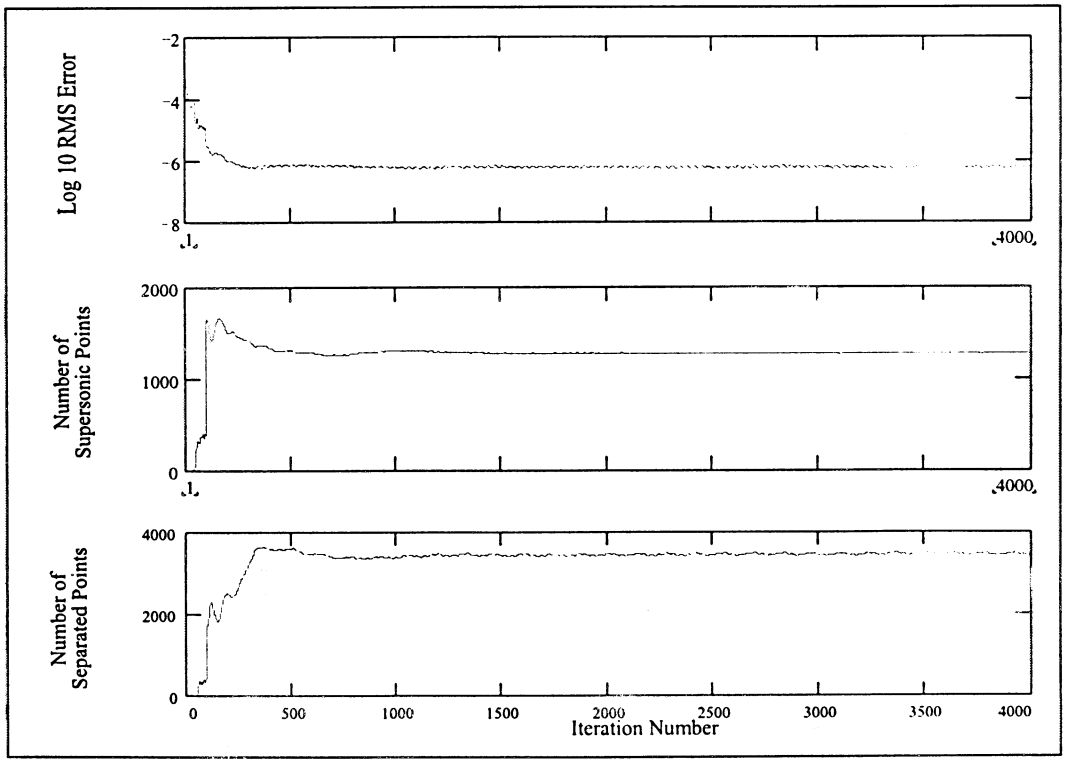

Figure 88: ADPAC Convergence History, Re = 100,000 M = 0.65 α = 9.00°

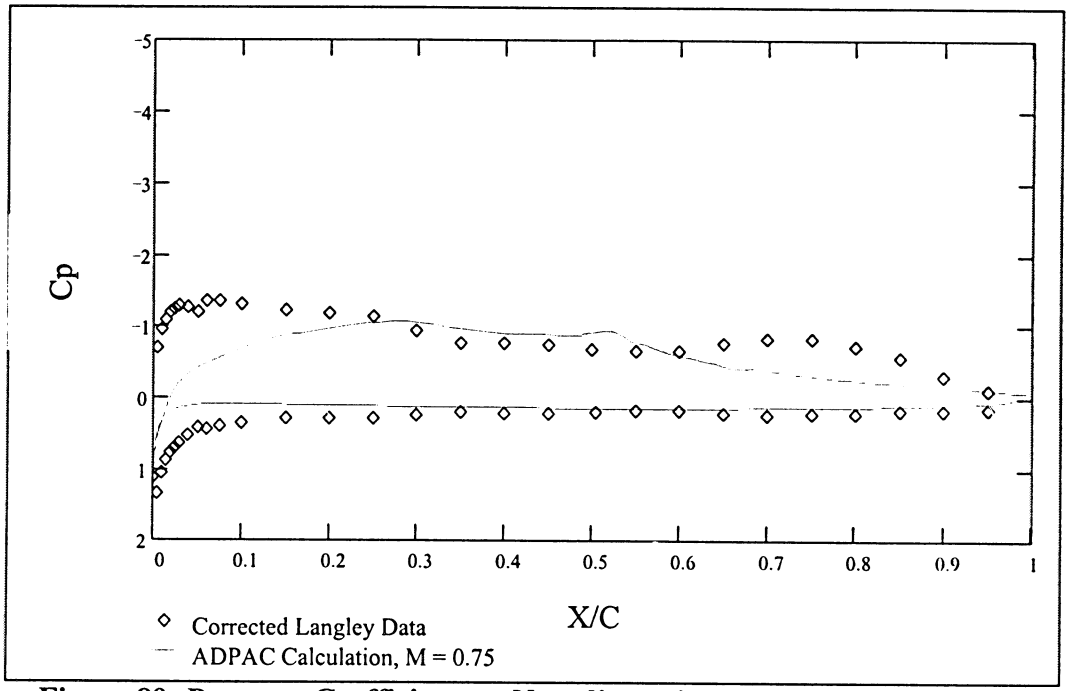

Figure 89: Pressure Coefficient vs. Non-dimensional Chordwise Position, Re = 60,000 α = 4.00°

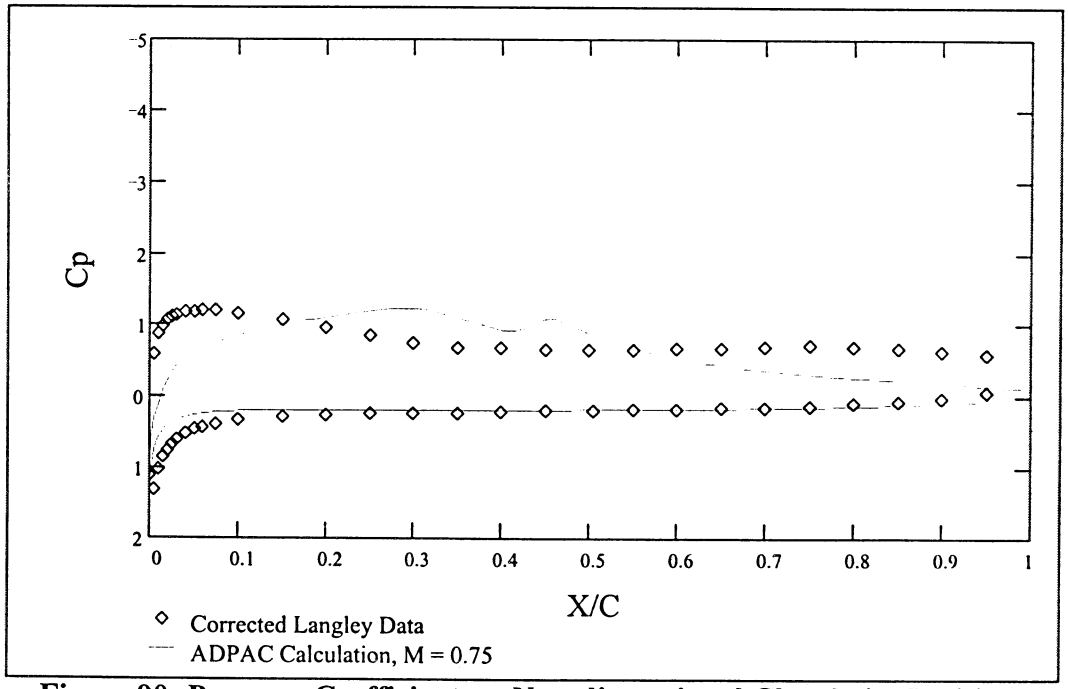

Figure 90: Pressure Coefficient vs. Non-dimensional Chordwise Position, Re = 60,000 α = 4.99°

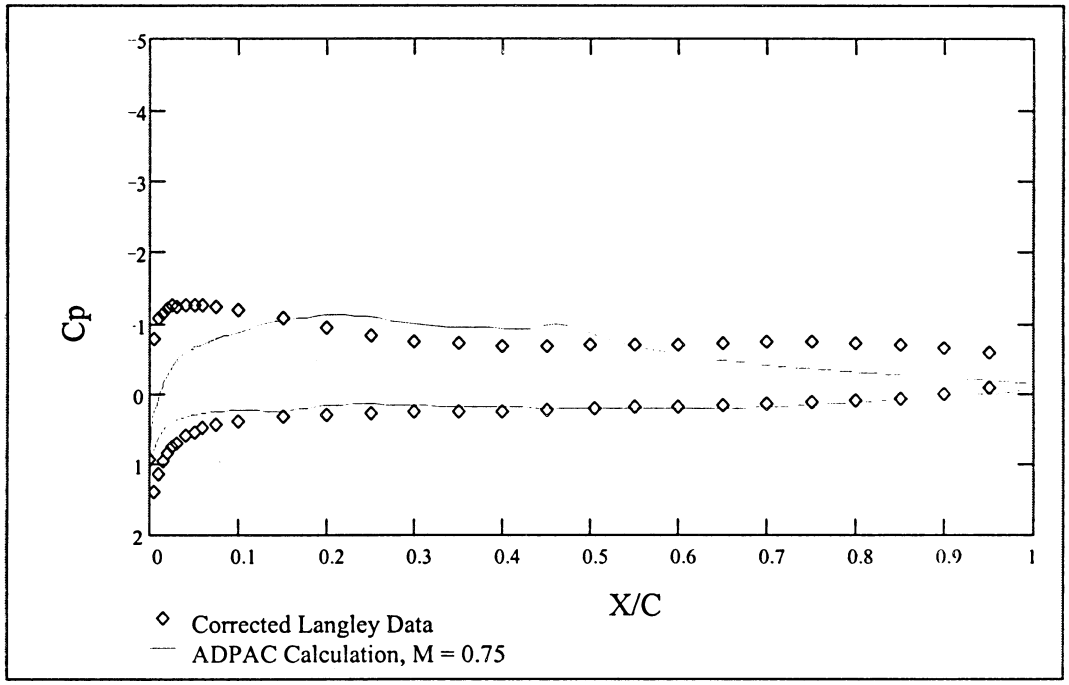

Figure 91: Pressure Coefficient vs. Non-dimensional Chordwise Position, Re = 60,000 α = 6.01°

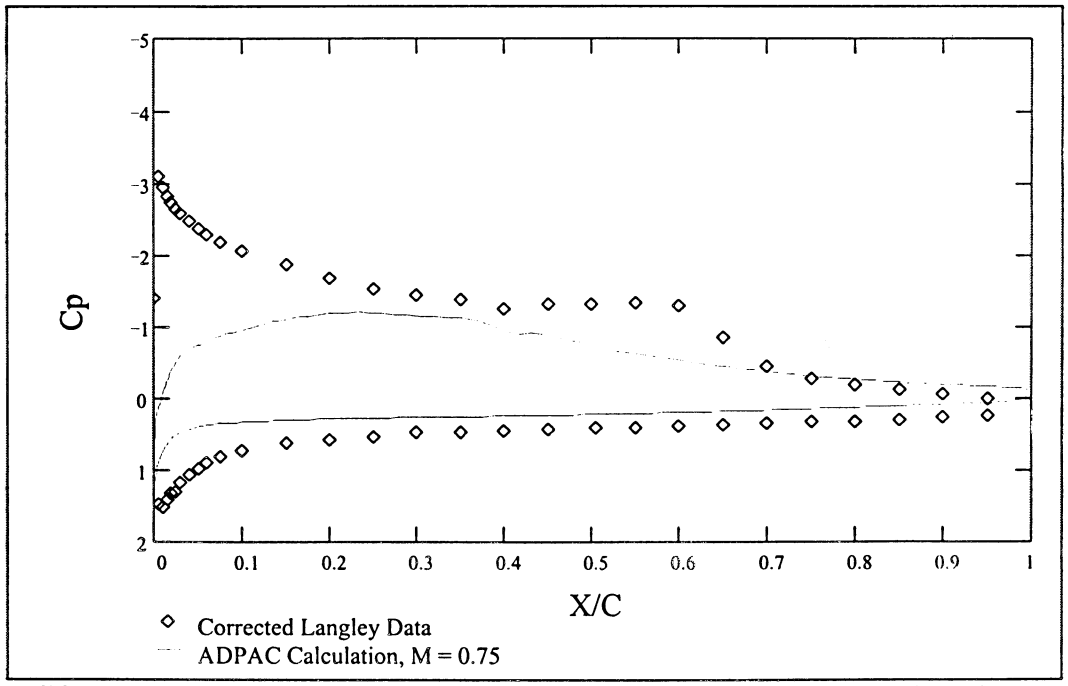

Figure 92: Pressure Coefficient vs. Non-dimensional Chordwise Position, Re = 60,000 α = 7.00°

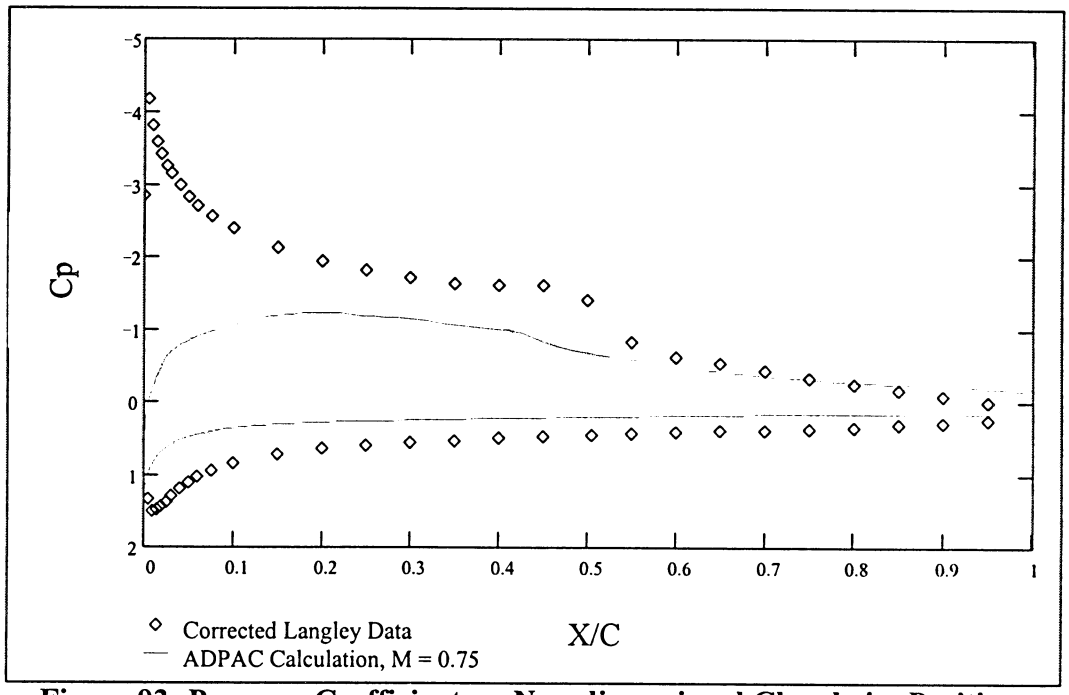

Figure 93: Pressure Coefficient vs. Non-dimensional Chordwise Position, Re = 60,000 α = 8.01°

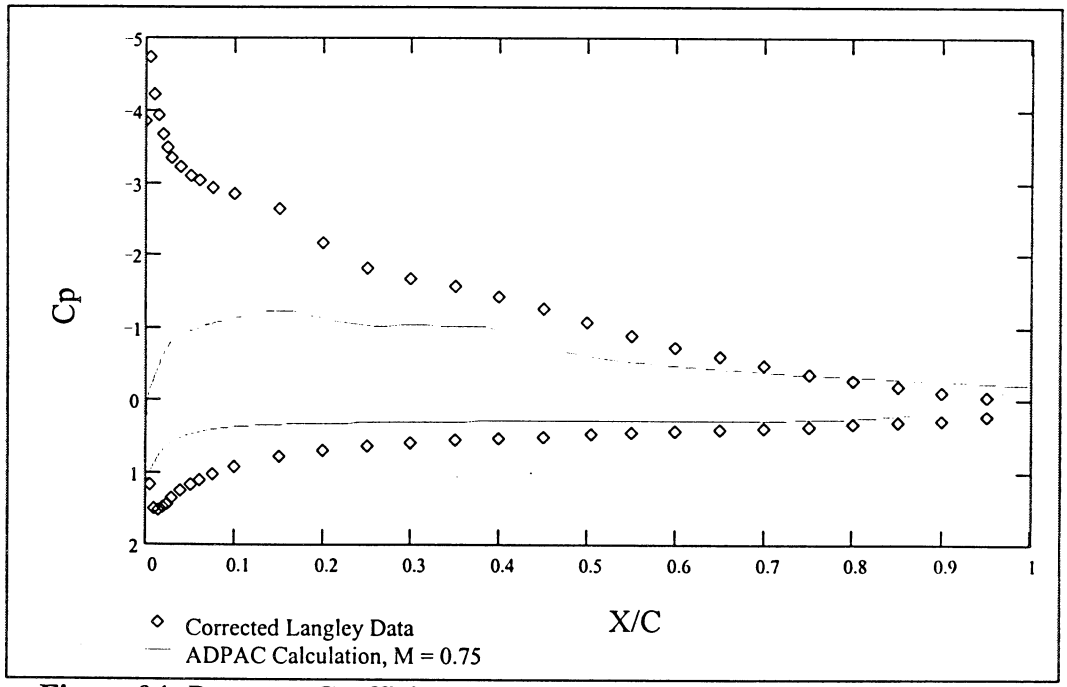

Figure 94: Pressure Coefficient vs. Non-dimensional Chordwise Position, Re = 60,000 α = 9.00°

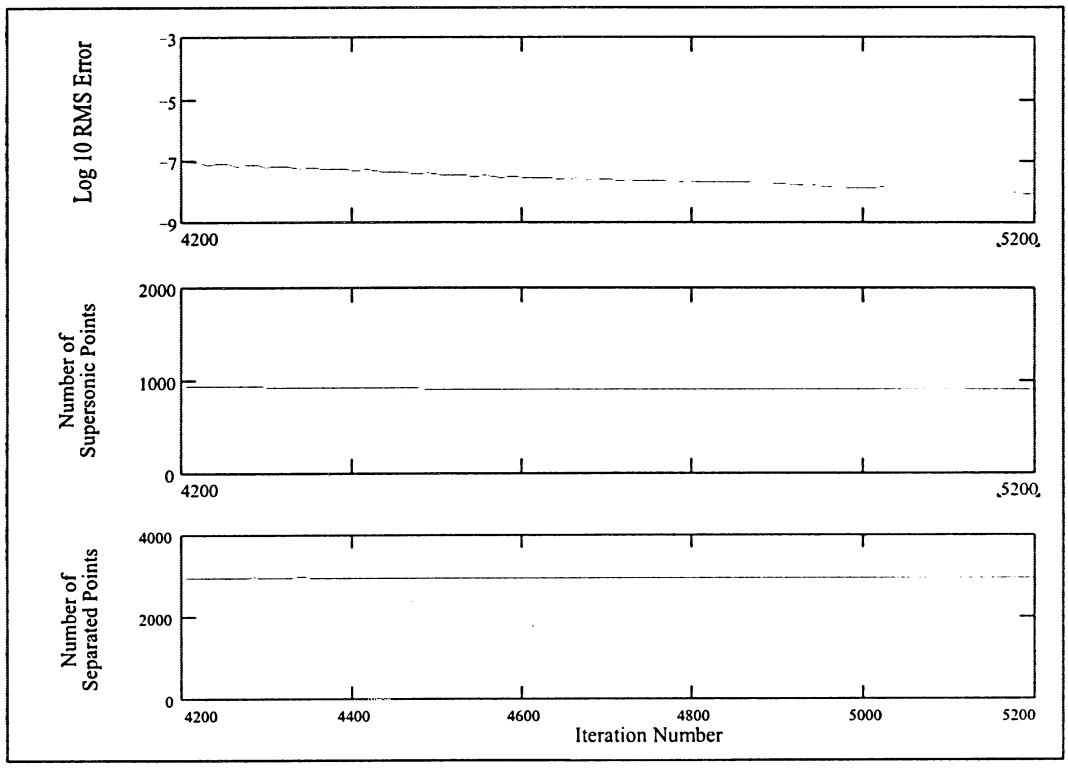

Figure 95: ADPAC Convergence History, Re = 60,000 M = 0.75 α = 4.00°

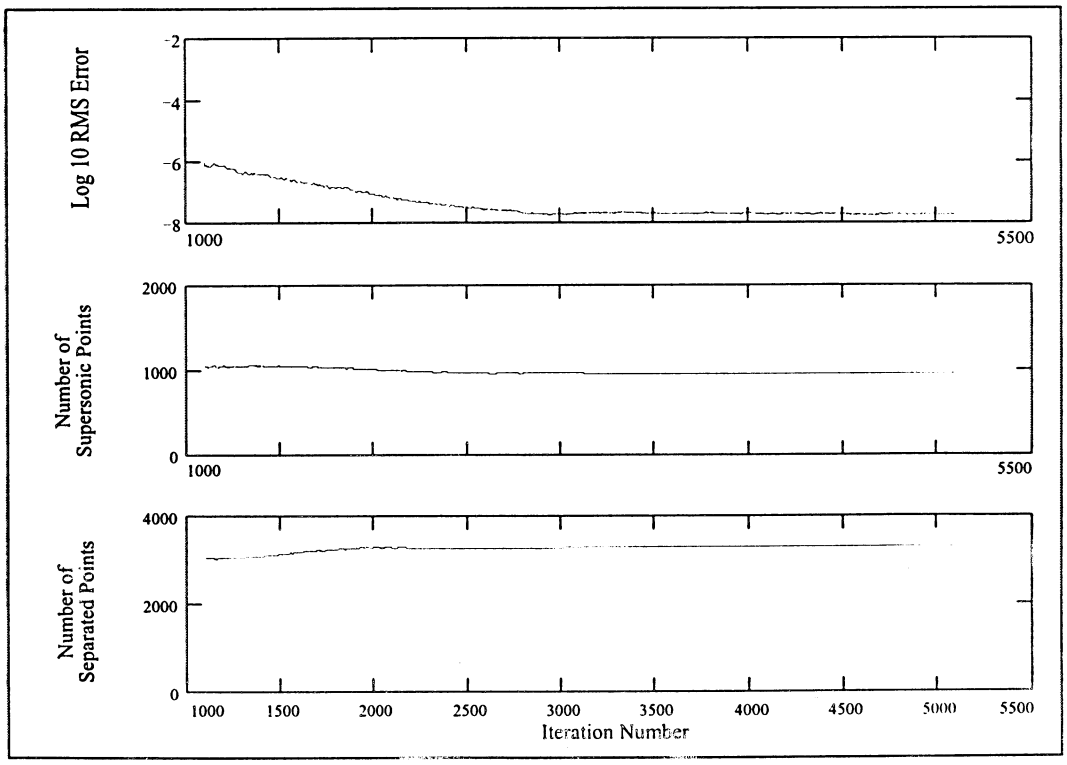

Figure 96: ADPAC Convergence History, Re = 60,000 M = 0.75 α = 4.99°

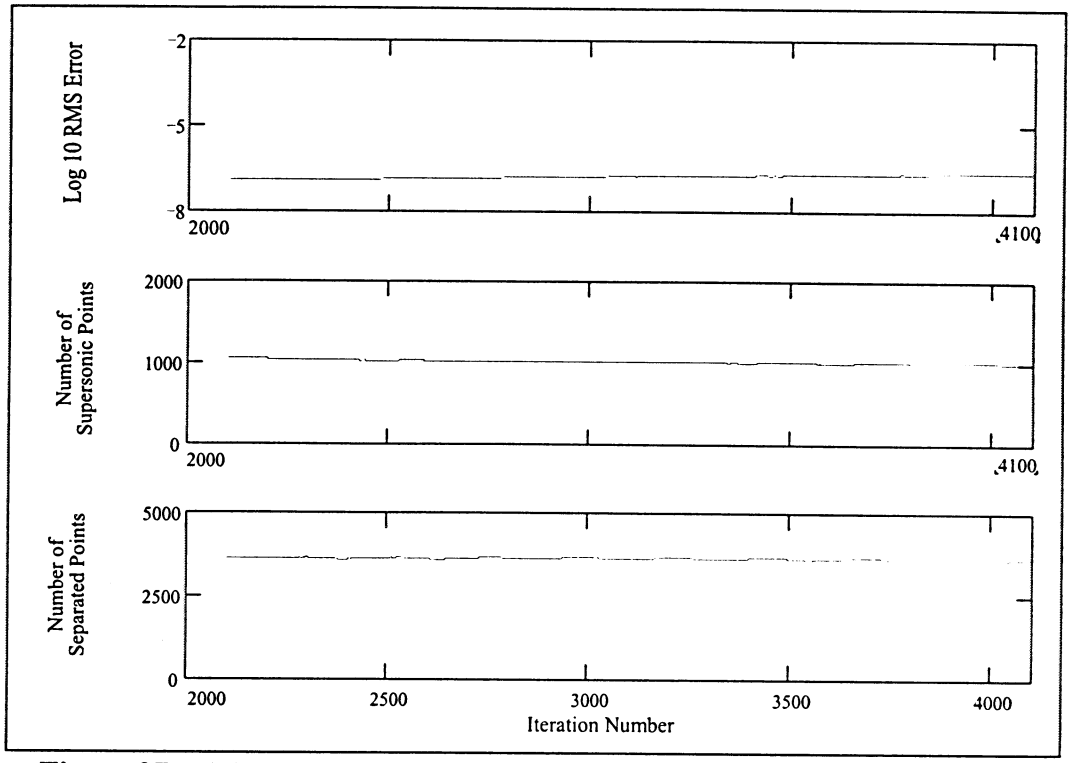

Figure 97: ADPAC Convergence History, Re = 60,000 M = 0.75 α = 6.01°

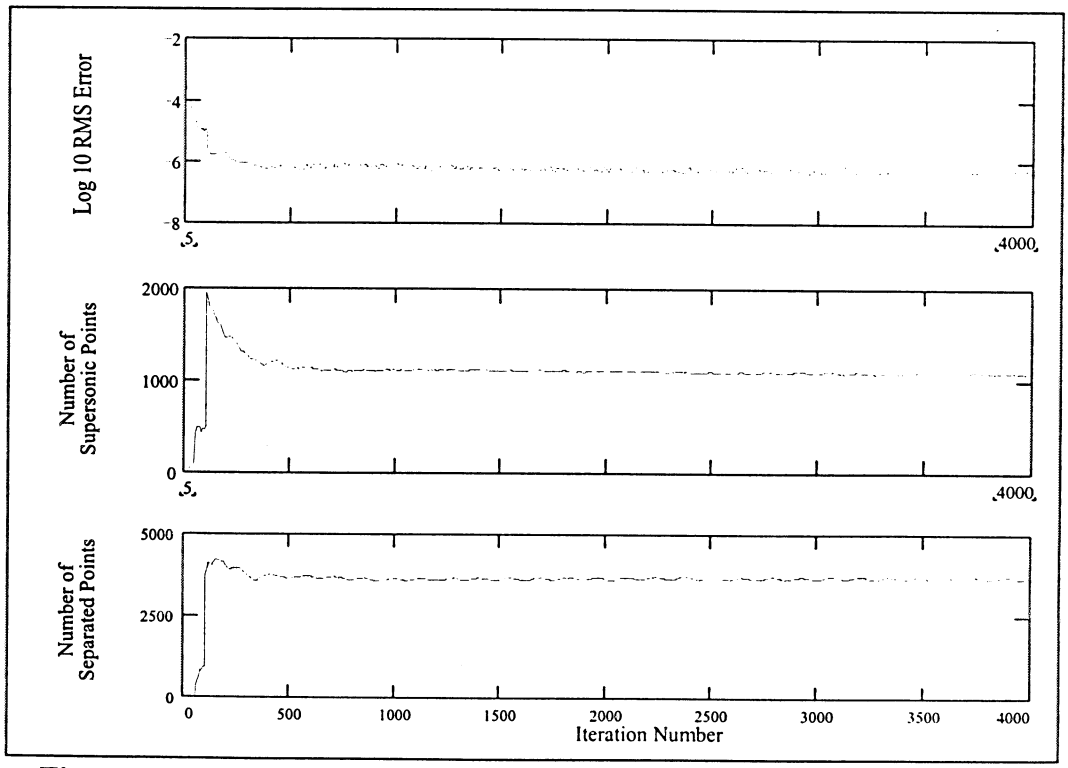

Figure 98: ADPAC Convergence History, Re = 60,000 M = 0.75 α = 7.00°

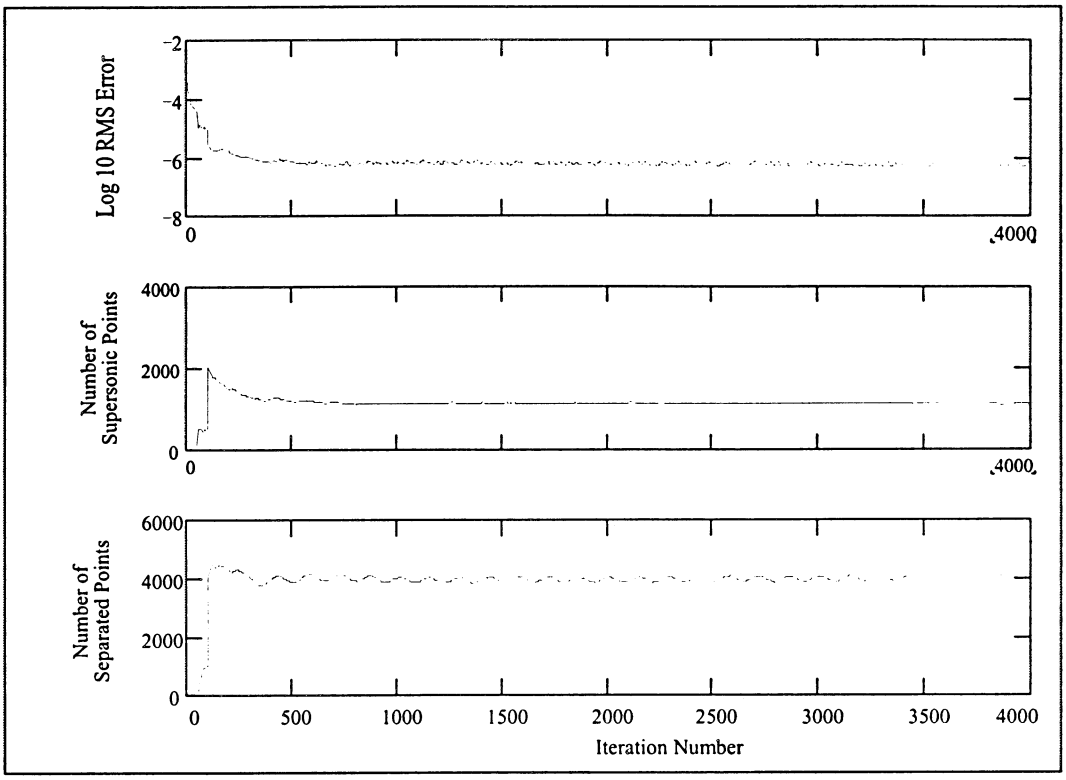

Figure 99: 1ADPAC Convergence History, Re = 60,000 M = 0.75 α = 8.01°

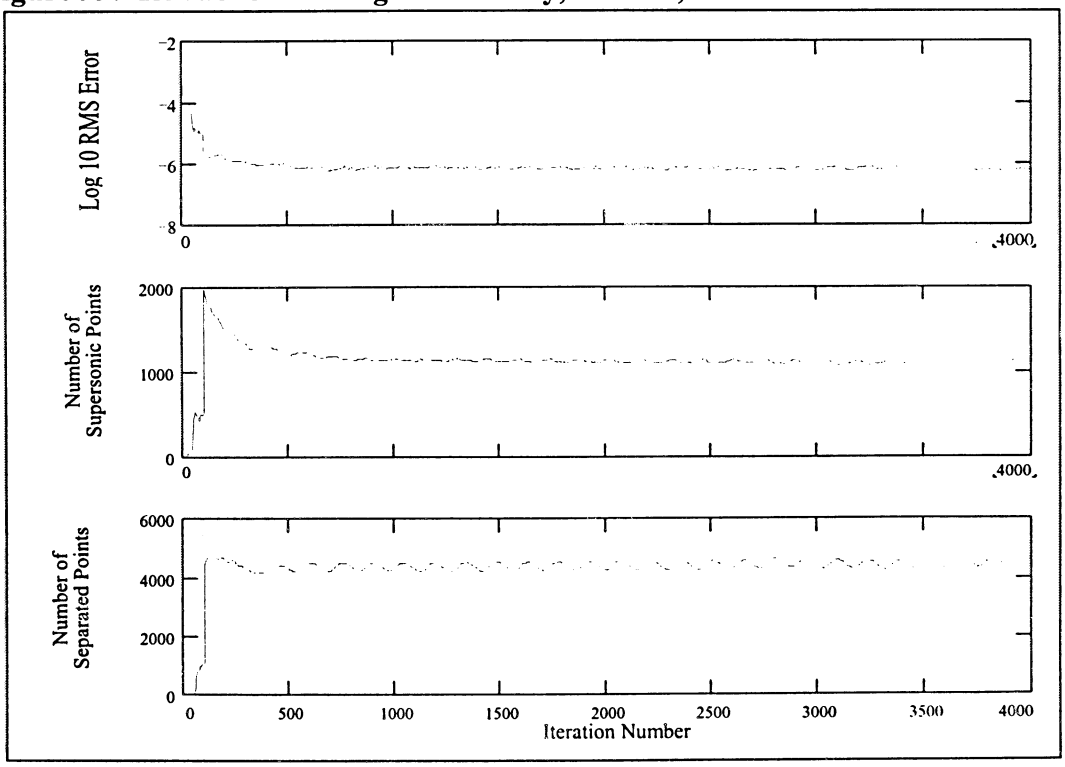

Figure 100: ADPAC Convergence History, Re = 60,000 M = 0.75 α = 9.00°

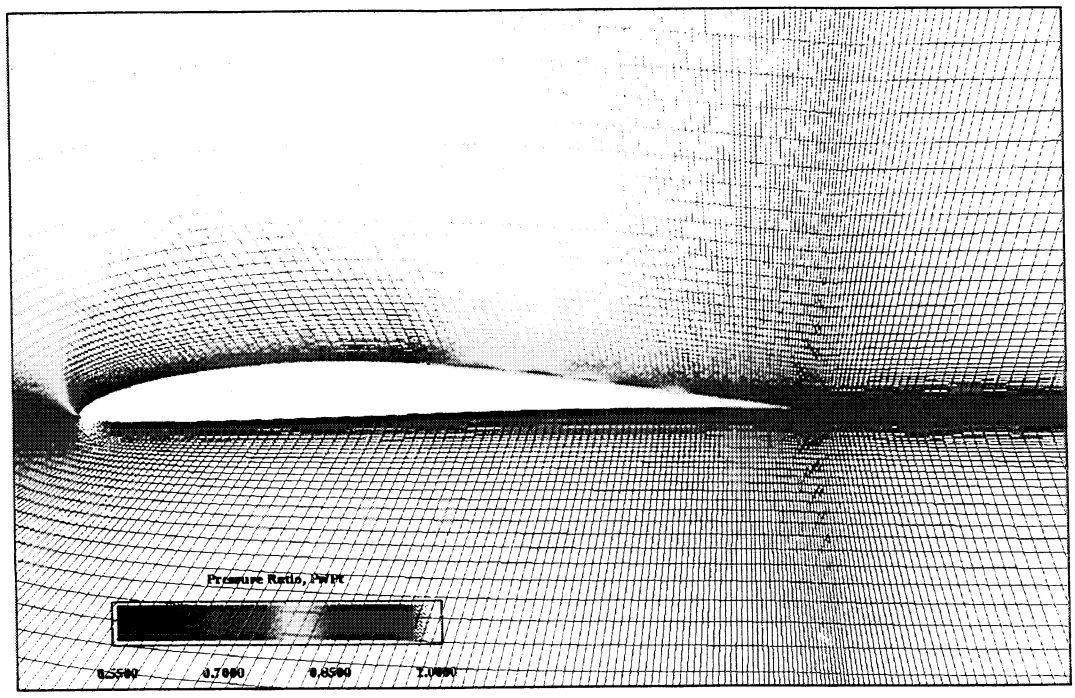

Figure 101: Pressure Distribution for Re = 60,000 M = 0.45 α= 8.01°

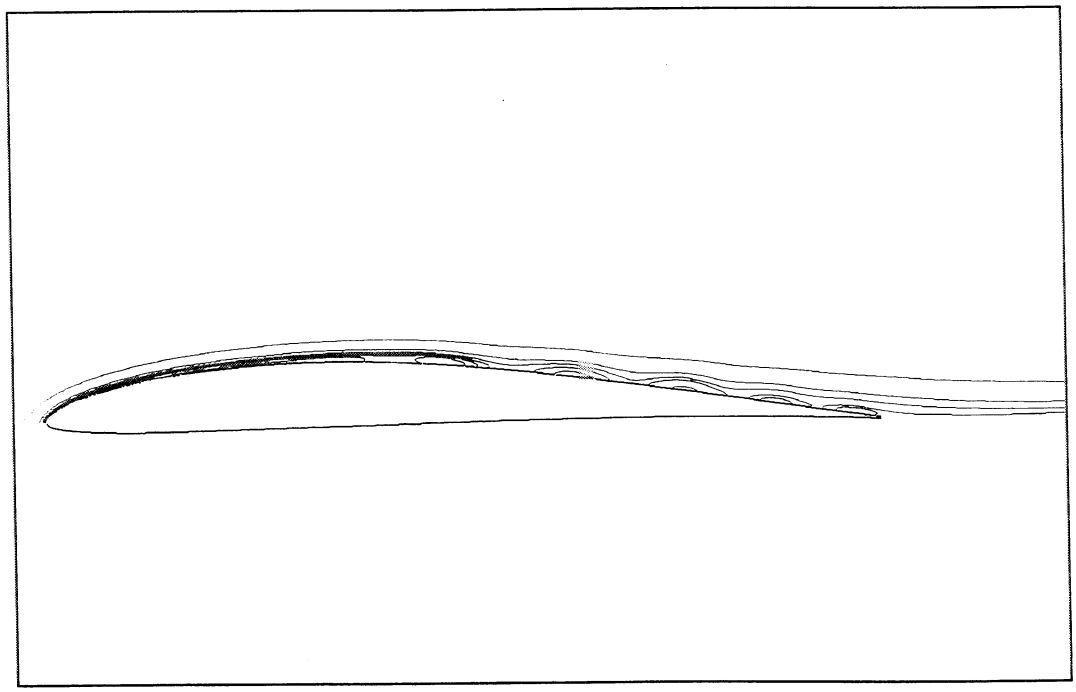

Figure 102: Streamlines Over the Suction Surface of the Airfoil, Re = 60,000 M = 0.45, α= 8.01°

CHAPTER 6

Propeller Design and Analysis Using Two-Dimensional ADPAC Predictions

The designs in Chapter 4 using only the low speed Langley data neglected the effects of compressibility. Even the Prandtl-Glauert compressibility corrections are inadequate for the tip sections. To account for the compressibility effects, the resulting lift and drag curves for each of the conditions listed in Table 3 were incorporated into the strip theory design and analysis programs (Figures 49 through 52). Again, simple conditional statements were used to apply these predicted values along the length of the blade.

The first design exercise was to see what effect elevated Mach numbers would have on the propellers designed using only the Langley experimental data. Keeping the number of blades, diameter, and Reynolds number distribution the same as was used for the initial designs, new designs were made. The new twist, chord, and lift coefficient distributions can be found in Figures 103 through 105.

Examination of the twist distribution still show a 'hook' near the tip. In these designs, though, this 'hook' results from the degradation in performance as Mach number is increased, rather than from the laminar stall found in the Langley data at low angles of attack. Efficiencies of the three and four-bladed propellers using the ADPAC predictions were 80.3% and 76.4%. These values are roughly 5% less than the efficiencies predicted for the low speed designs using the low speed Langley data alone.

To optimize the design, a lift coefficient distribution asymptotically reaching the average maximum lift-to-drag ratio point along the blade was specified (Fig. 106). This was done to increase the chordlengths of the inboard sections, as was seen to be necessary in Chapter 4. The resulting propeller twist, chord, Reynolds number, and relative Mach number distributions can be found in figures 107 through 110. Efficiency for this propeller at design point was 85.1%. This propeller was considered to be the final design.

The strip-theory analysis program was used to generate off-design propeller performance predictions for the final design. Input to the analysis program includes the propeller geometry, advance ratio, pitch angle, cruise Mach number, and altitude. The program iterates to find the induced velocities and induced angle of attack. From this information, the lift coefficient distribution along the blade can be found and propeller thrust, power, and torque coefficients as well as efficiency can be calculated. Among the many tests of programming integrity, performance calculated by the design program should and did exactly match that calculated by the analysis program at design point.

The off-design performance maps were created by changing the advance ratio and pitch angle of the propeller. Variations of the propeller efficiency, thrust, power, and torque coefficients for a range of pitch angles are shown in figures 111 through 114. At design point, the value of the advance ratio is 1.814 and the blade twist angle at the 75% radial position is 42.52°.

Examination of the off-design performance curves for the propellers indicates that there may be some merit to operating the propeller at a slightly higher pitch angle than that at the design point. While maintaining the design advance ratio of 1.814, increasing the pitch angle so that the angle at the 75% radial position is 45°, a 25% increase in thrust can be realized for a penalty of 5% in efficiency. Operating at this point may be desirable if sufficient engine power is available. Increasing the pitch setting past this point may not be recommended since the blade begins to stall when the angle at the 75% radial station reaches 50° as shown in Figure 115. To decrease the advance ratio while maintaining a constant cruise velocity may not yield the predicted increase in thrust since as tip speeds increase, shock waves will affect a larger portion of the blade degrading performance. A comparison of the design point conditions and those for this high thrust case can be found in Table 4. Actual performance for both cases will vary from the predicted values as the blades twist in operation. A structural analysis would need to be conducted to understand the propeller's performance more fully.

Table 4. Comparison of the Design Point and Maximum Thrust Point

	Design Point Pitch Angle at 75%R = 42.52°	Maximum Thrust Point Pitch Angle at 75%R = 45.00°
Efficiency	0.8509	0.8107
Thrust Coefficient	0.1411	0.1780
Power Coefficient	0.3007	0.3983
Torque Coefficient	0.0479	0.0634
Thrust	450.9 N (101.3 lbs)	569.0 N (127.9 lbs)
Power	63.4 kW (85 hp)	83.9 kW (112.6 hp)
Torque	703.7 N-m (519.0 ft-lbs)	932.1 N-m (687.5 ft-lbs)
Advance Ratio	1.814	1.814

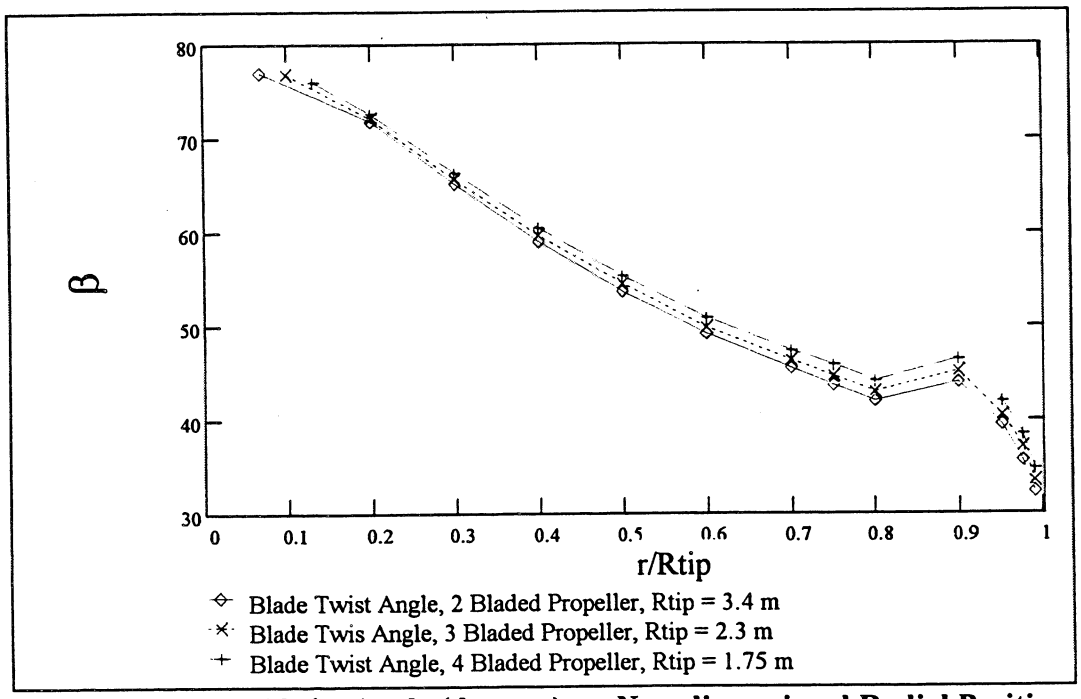

Figure 103: Blade Twist Angle (degrees) vs. Non-dimensional Radial Position, Designed Using ADPAC Predicted Values Only

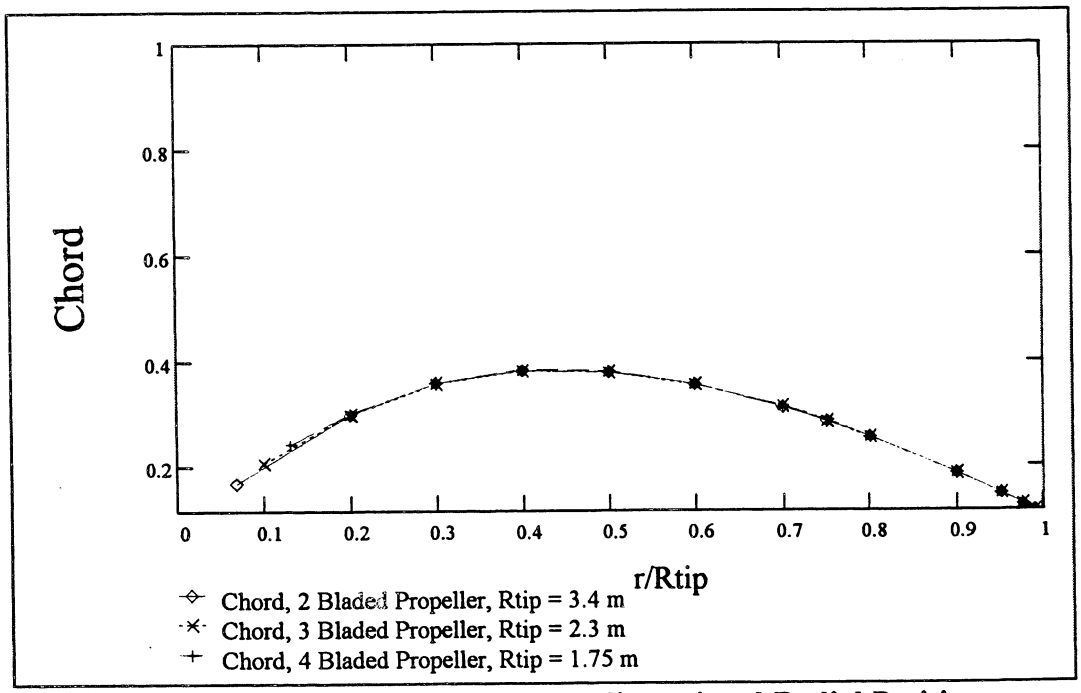

Figure 104: Chord (meters) vs. Non-dimensional Radial Position, Designed Using ADPAC Predicted Values Only

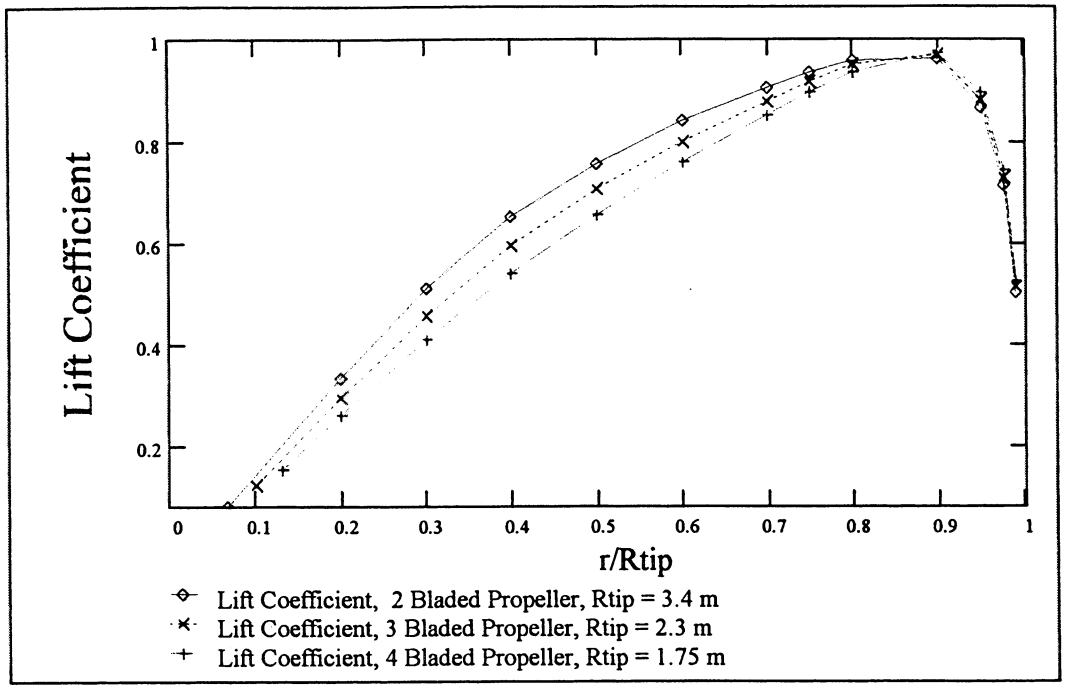

Figure 105:Lift Coefficients vs Non-dimensional Radial Position

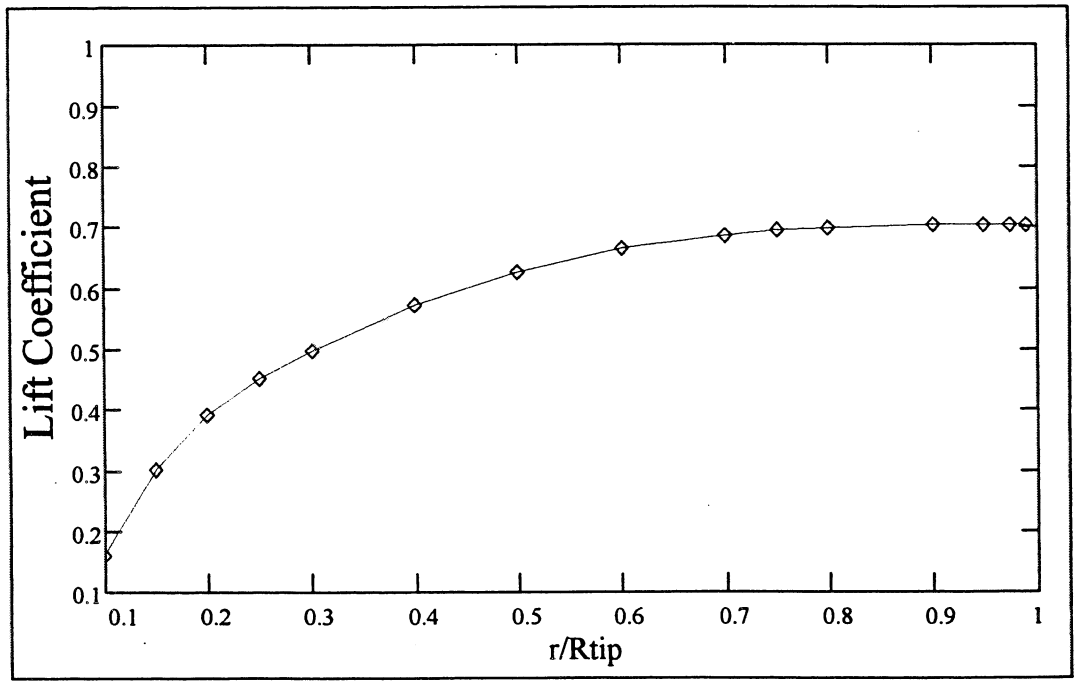

Figure 106: Lift Coefficient vs. Non-dimensional Radial Position, ADPAC Predicted Values Only

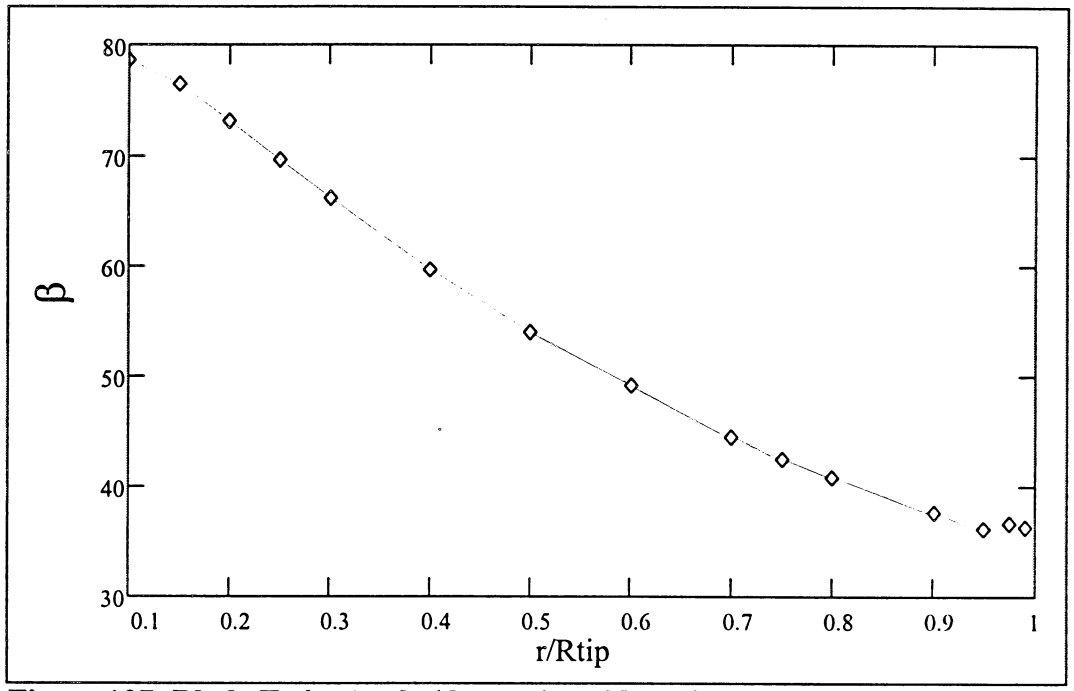

Figure 107: Blade Twist Angle (degrees) vs. Non-dimensional Radial Position, Designed Using ADPAC Predicted Values Only

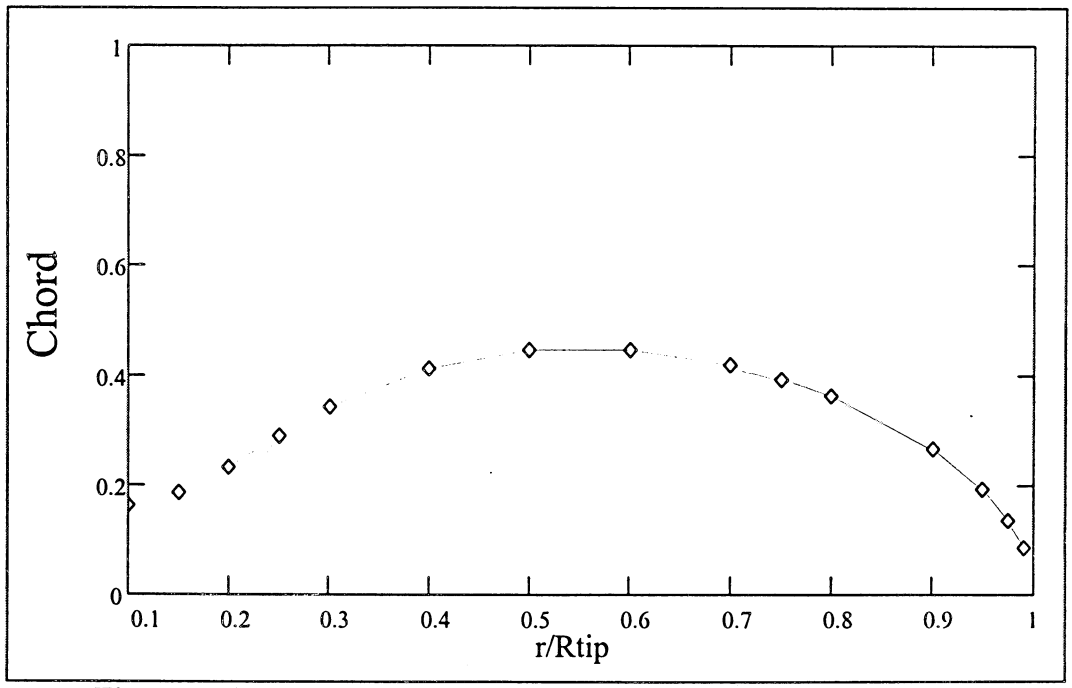

Figure 108: Chord (meters) vs. Non-dimensional Radial Position, Designed Using ADPAC Predicted Values Only

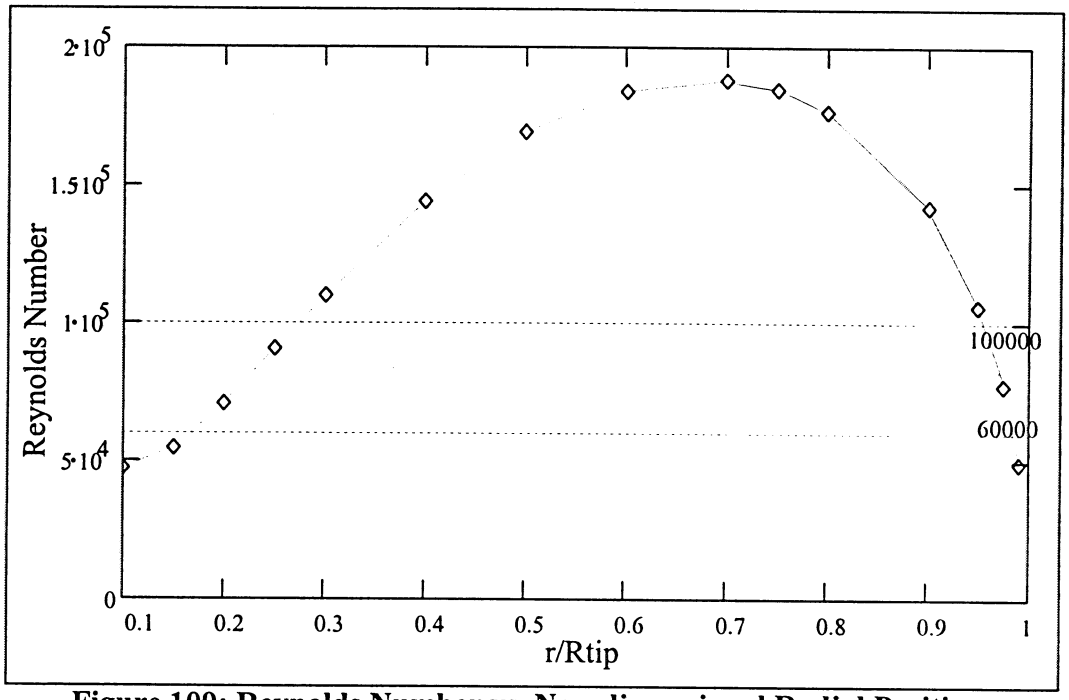

Figure 109: Reynolds Number vs. Non-dimensional Radial Position, Designed Using ADPAC Predicted Values Only

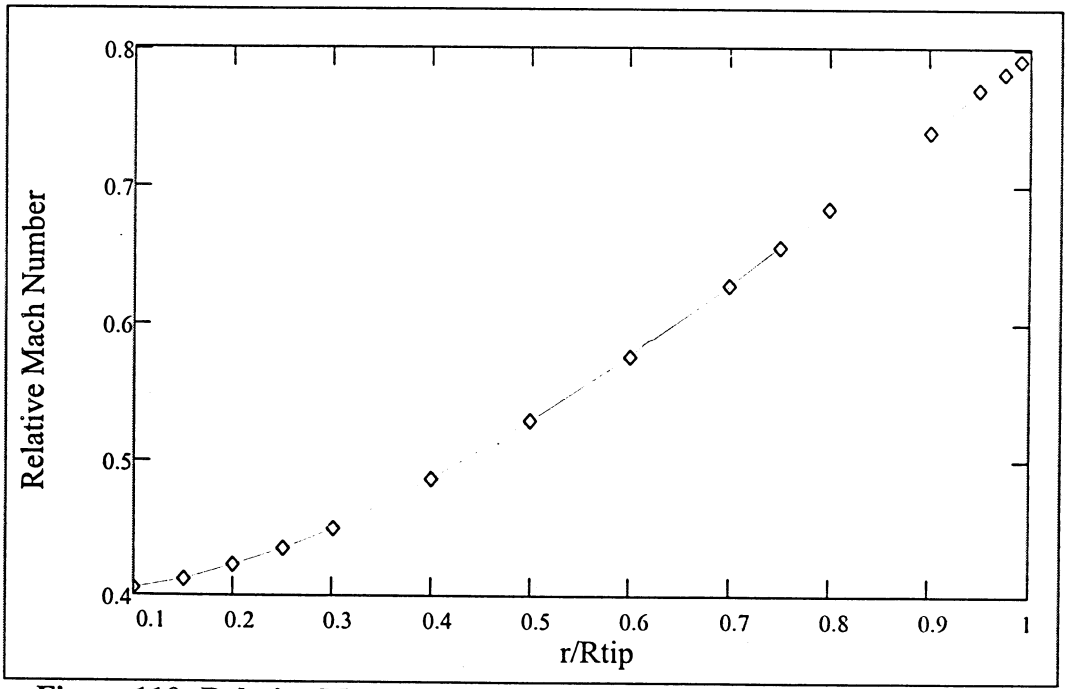

Figure 110: Relative Mach Number vs. Non-dimensional Radial Position, Designed Using ADPAC Predicted Values Only

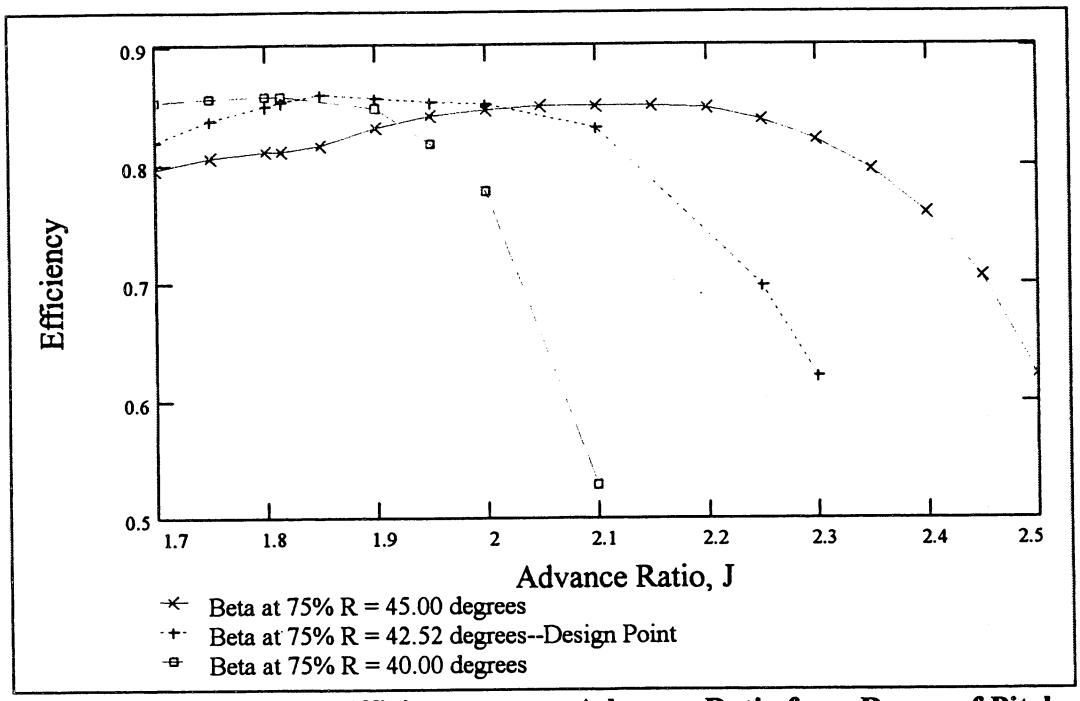

Figure 111: Propeller Efficiency versus Advance Ratio for a Range of Pitch Angles

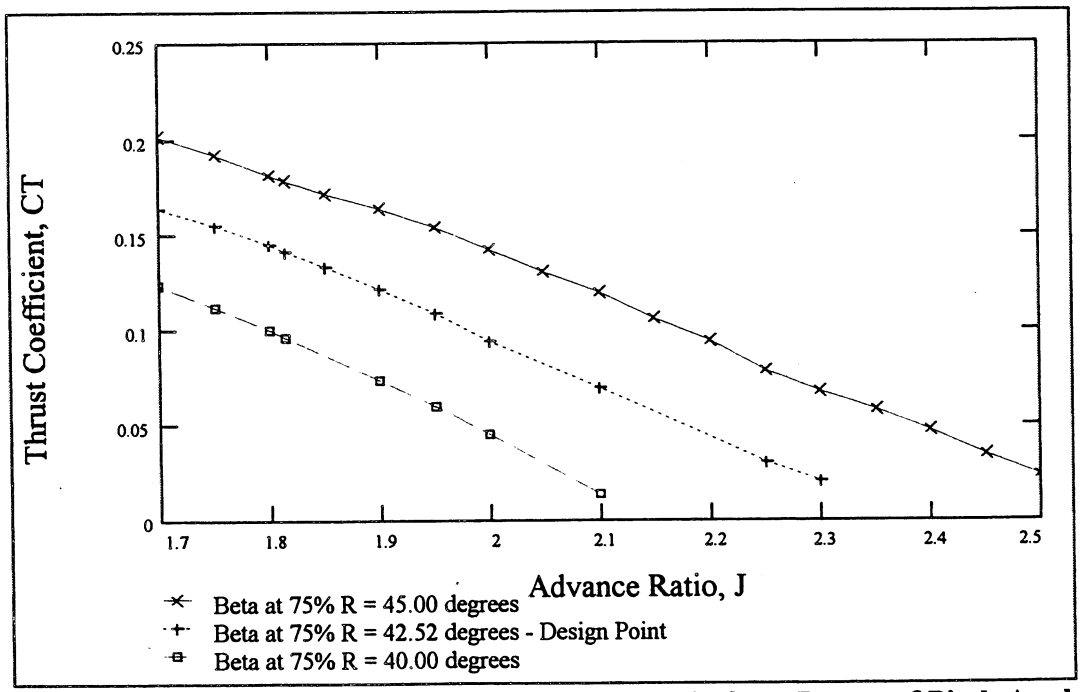

Figure 112: Thrust Coefficient versus Advance Ratio for a Range of Pitch Angles

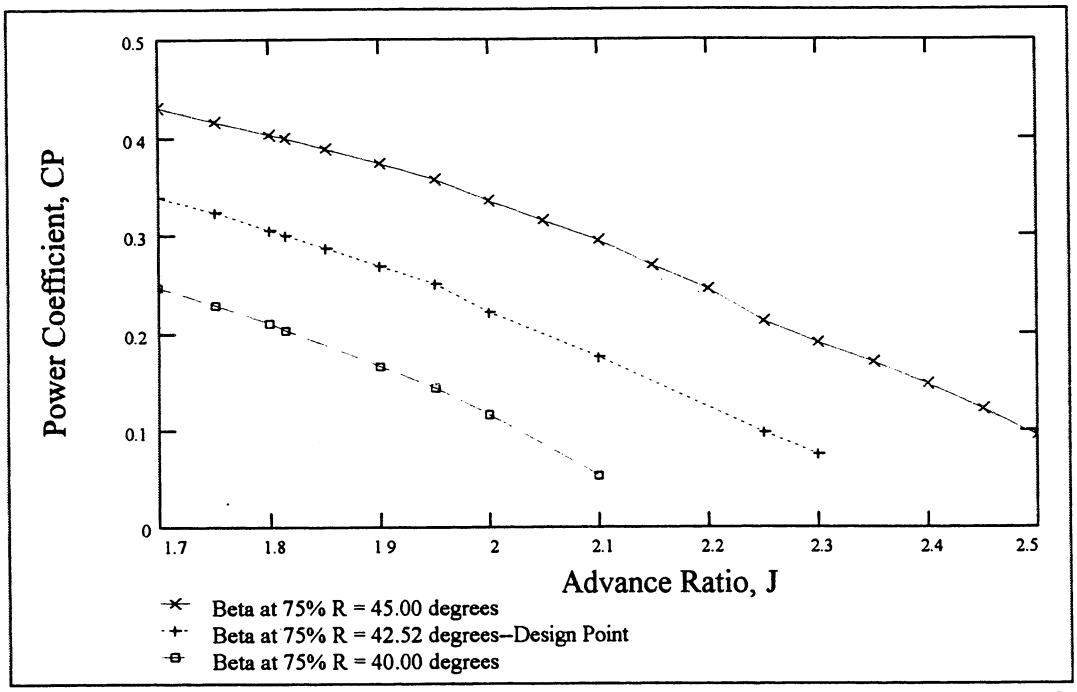

Figure 113: Power Coefficient versus Advance Ratio for a Range of Pitch Angles

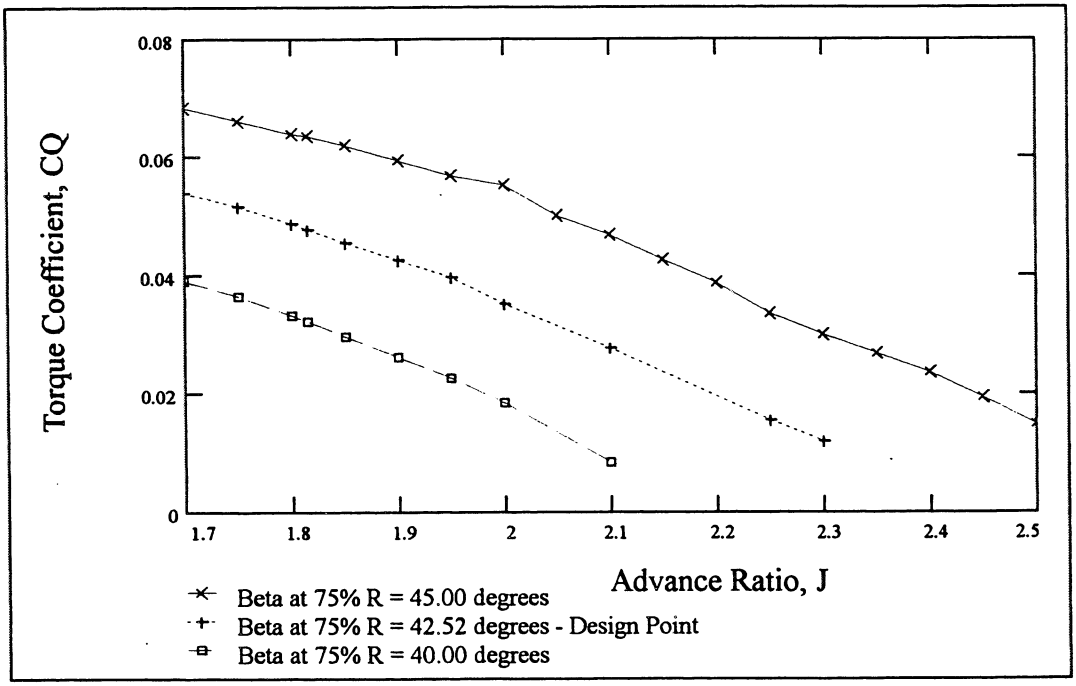

Figure 114: Torque Coefficient versus Advance Ratio for a Range of Pitch Angles

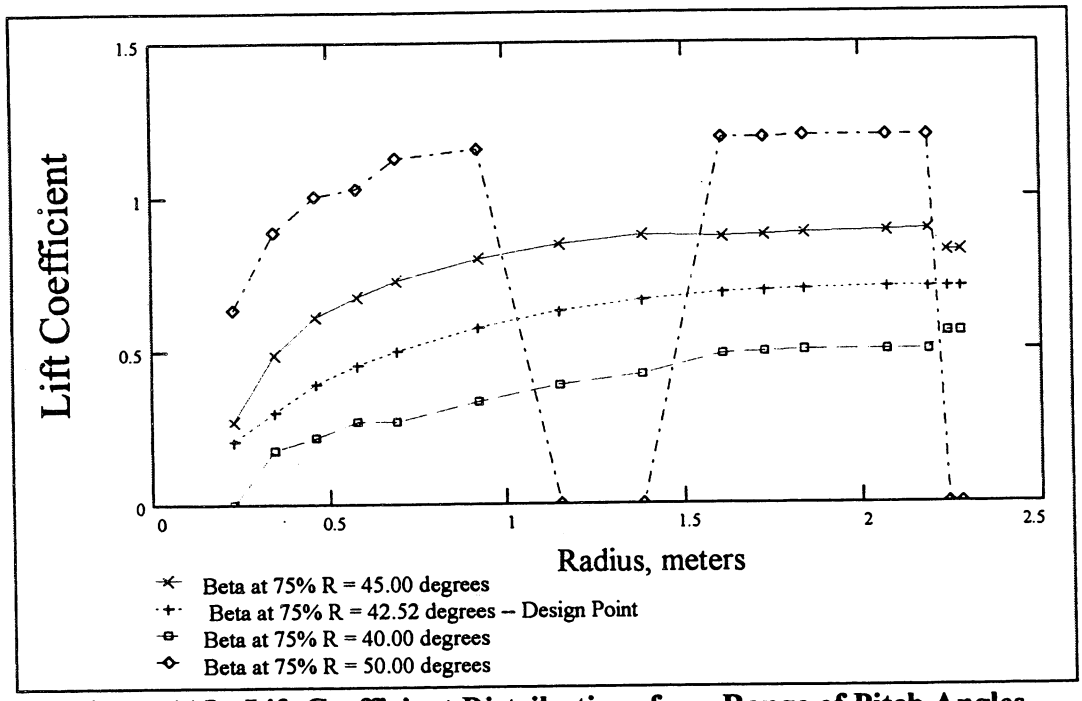

Figure 115: Lift Coefficient Distributions for a Range of Pitch Angles

CHAPTER 7

ADPAC Three-Dimensional Performance Calculations

A three-dimensional model of the propeller was made from the twist and chord distributions (Fig. 107-108) calculated using Adkins' and Liebeck's strip theory design methods (Ref. 5). Views of the propeller's solid surfaces can be seen in Figures 116 and 117. The computational mesh of the flowfield around the propeller extends one radius upstream of the propeller, one radius downstream, and one radius radially outward from the blade tip. The entire mesh contains 4,157,138 grid points. The hub surface was modelled as a simple cylinder. The blade suction and pressure surfaces were established as "no-slip" surfaces while the cylindrical hub was established as a "slip" surface. Total temperature and total pressure were fixed on the vertical inlet plane, and freestream static pressure was fixed at the vertical exit plane. The freestream Mach number was fixed on the cylindrical outer boundary of the computational grid.

A program called TCGRID written by Roderick V. Chima (Ref. 14) was used to create a fine "C" grid around one propeller blade as well as a somewhat coarser "H" grid farther upstream of the blade. Since TCGRID was originally intended to generate meshes for turbomachinery blading, it was a challenge to create an appropriate mesh for such a large blade with this program. The two grid blocks made with TCGRID were modified so that the final mesh consisted of ten separate grid blocks. As shown in Figure 118, the fine "C" grid block was broken into four

separate blocks (Blocks 1-4), and the coarse inlet block is shown in yellow as Block 5. The fine mesh was retained for Block 1 closest to the blade, while the mesh was coarsened by eliminating every other grid line from the original fine mesh to yield Blocks 2 through 4. The coarse mesh was broken at the corners of the "C" grid to avoid possible problems within ADPAC concerning stretching ratios, or the relative size of neighboring computational cells. Figure 119 is a view forward looking aft of the computational domain surrounding one of the three propeller blades. Figures 120 through 122 show the portion of the computational mesh near the inlet block region, near the blade hub, and near the exit region, respectively. Separate FORTRAN programs were written to extend the mesh radially outwards creating Blocks 6 through 10 (Fig. 123).

There are many features which are desired of a computational mesh—some for physical reasons and some to comply with the ADPAC program format. Physically, there again should be enough grid points packed close to the blade surface so that the boundary layer can be resolved. The grid should also extend well into the free stream ahead of the blade, behind the blade, and radially outward. It is also recommended that the gridlines follow the trailing edge angle of the blade sections so that separation and any vortices that may be shed can be seen. The challenge when creating a mesh is meeting all these requirements while keeping the number of grid points to a minimum to reduce computational time. Practically, the upstream and downstream extents of the mesh were sacrificed in order to add grid points closer to

the blade surface. Even so, the three-dimensional mesh is much coarser than the two-dimensional meshes seen earlier. Values for y^+ of the first grid line above the blade surface at approximately the quarter chord location were 2.266 for the section at r/Rtip = 0.406, 2.692 for the section at r/Rtip = 0.666, and 3.671 at r/Rtip = 0.905.

For a mesh to be suitable for an ADPAC three-dimensional calculation, stretching ratios for the cells should be around 1.3. TCGRID did not contain input parameters to vary stretching ratios directly, so this requirement was met by adding grid points until the stretching ratios near the tip were within acceptable bounds. ADPAC uses a multigrid method to speed convergence. This technique generates intermediate solutions by coarsening the mesh by eliminating grid points. Three levels of multigrid are recommended and can be achieved if the number of cells in each direction for each block are divisible by four. Coordinates for the leading edge and trailing edge of the blade must also meet this criterion if the multigrid technique is to be used. If an "H" grid is used for an inlet block, the upstream edge of the "C" grid must be square and must not overlap the inlet block cells. Finally, coordinates of all grid blocks must be ordered to form a left-handed coordinate system.

ADPAC was used to calculate the steady state viscous flow over the rotating propeller blade at the design conditions. The convergence history plots are shown in Figure 124. After over 2500 iterations, the solution was considered to be converged because the RMS error had decreased by three orders of magnitude and the number of separated points was constant. Figure 125 shows three blade sections near the hub,

midspan, and tip of the blade where the pressure and Mach number contours are shown in Figures 126 through 131. The ADPAC solution at the design point indicated no separation bubbles that had been seen in the low Reynolds number low Mach number two-dimensional cases studied earlier. Full separation near the trailing edge was seen, along with a shock wave along approximately one quarter of the blade near the tip. The area of supersonic flow is more clearly seen in Figures 132 and 133. Efficiency, as well as thrust, power, and torque coefficients were calculated and compared to results obtained from strip theory calculations. The comparisons can be in Table 5 or graphically in Figures 134 through 137.

Table 5. Comparison of Strip Theory and ADPAC Results at Design Point

	Strip Theory Result at the Design Point	**ADPAC Result at the Design Point**
Efficiency	0.8509	0.8624
Thrust Coefficient	0.1411	0.1355
Power Coefficient	0.3007	0.2850
Torque Coefficient	0.04785	0.04536
Thrust	450.9 N (101.3 lbs)	433.0 N (97.3 lbs)
Power	63.4 kW (85 hp)	60.1 kW (80.6 hp)
Torque	703.7 N-m (519.0 ft-lbs)	667.0 N-m (491.9 ft-lbs)

power, and torque coefficients were approximately 5% lower. This difference can be attributed to several factors. First, because of the simplistic application of the two-dimensional low Reynolds number transonic predictions, the strip theory design did not account for the shock from r/Rtip of approximately 0.75 to 0.90. Secondly, the three-dimensional mesh was considerably less dense than the two-dimensional meshes and may be below the value for which the solution is independent of the number of grid points. Finally, the tip vortices as shown in Figure 138, were not taken into account in the strip theory design and analysis programs. The tip vortex from one blade and the blade wake can also be seen in the Mach number distribution at the exit of the computational domain shown in Figure 139.

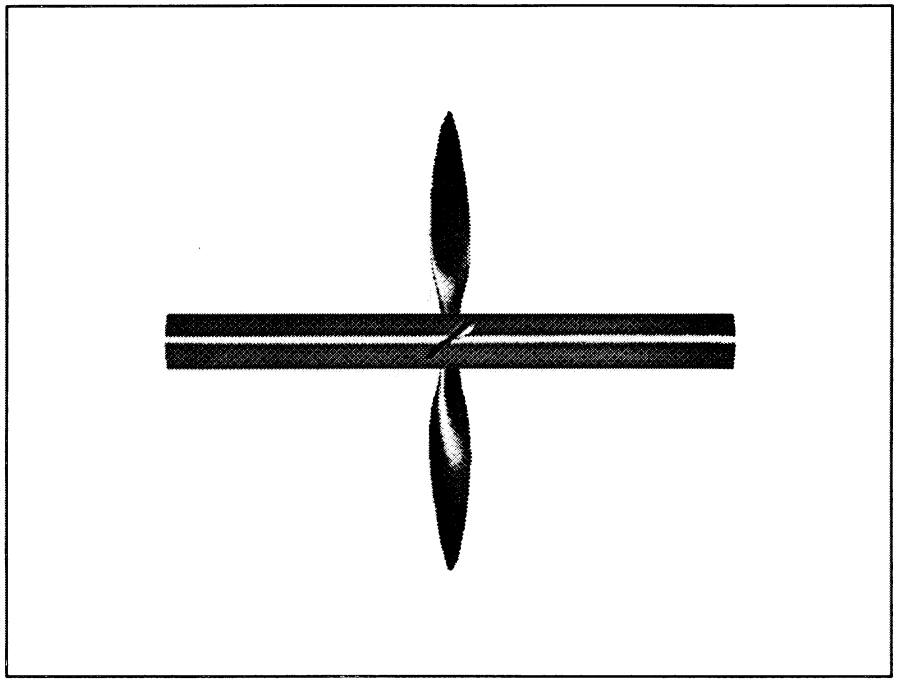

Figure 116: The Three-Bladed Propeller and Extended Hub Surface, Side View

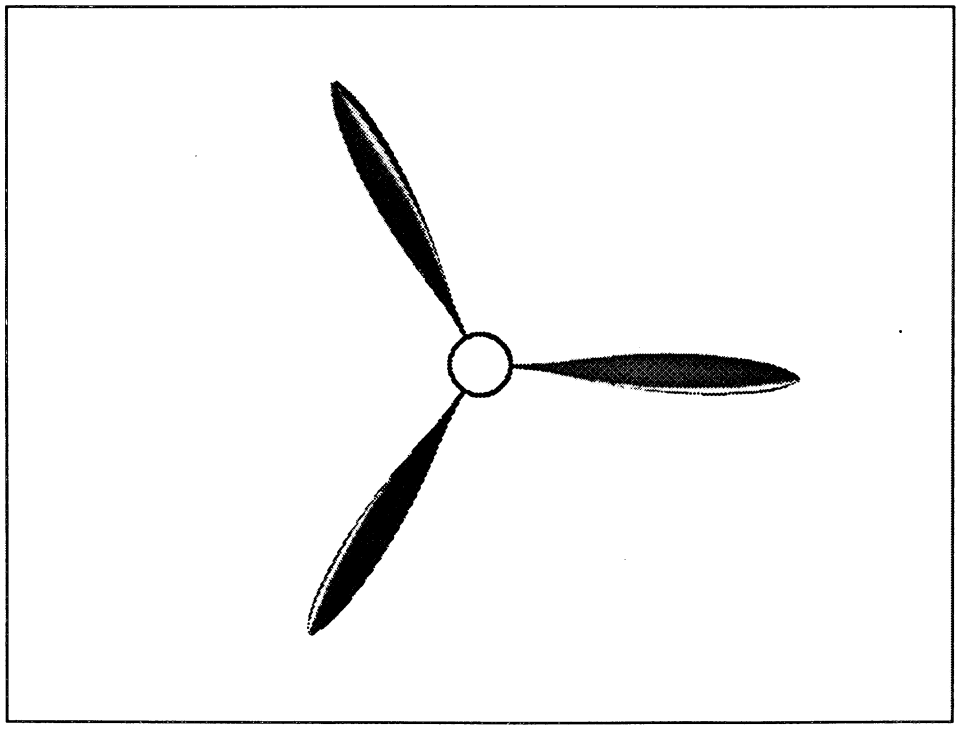

Figure 117: Front View of Three-Bladed Propeller

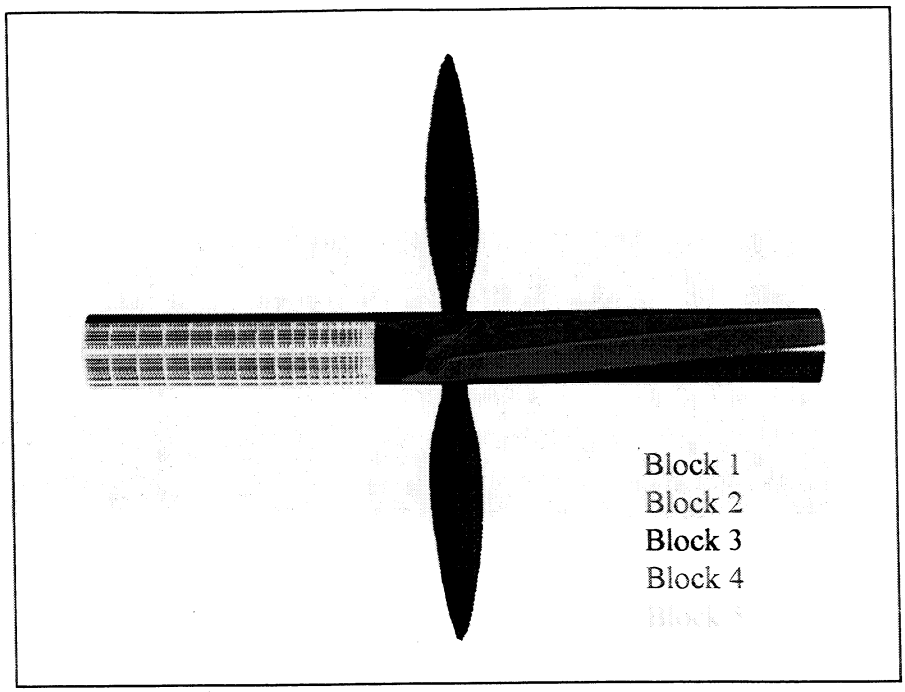

Figure 118: Computational Mesh Blocks and Solid Surfaces, Axial View

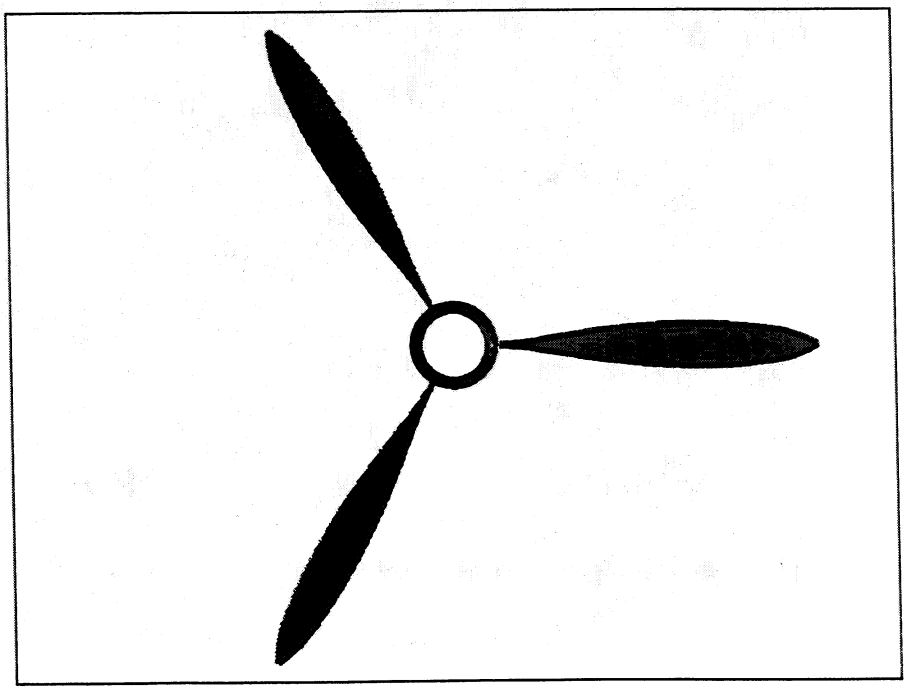

Figure 119: Forward Looking Aft View of Propeller Blade and Computational Mesh Blocks

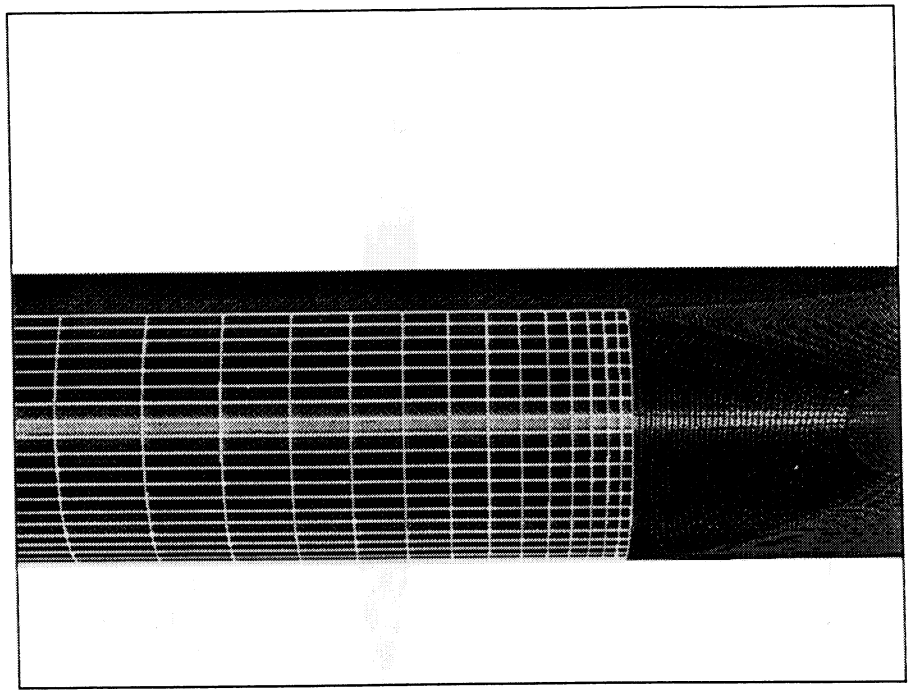

Figure 120: Magnified View of Inlet Block Region

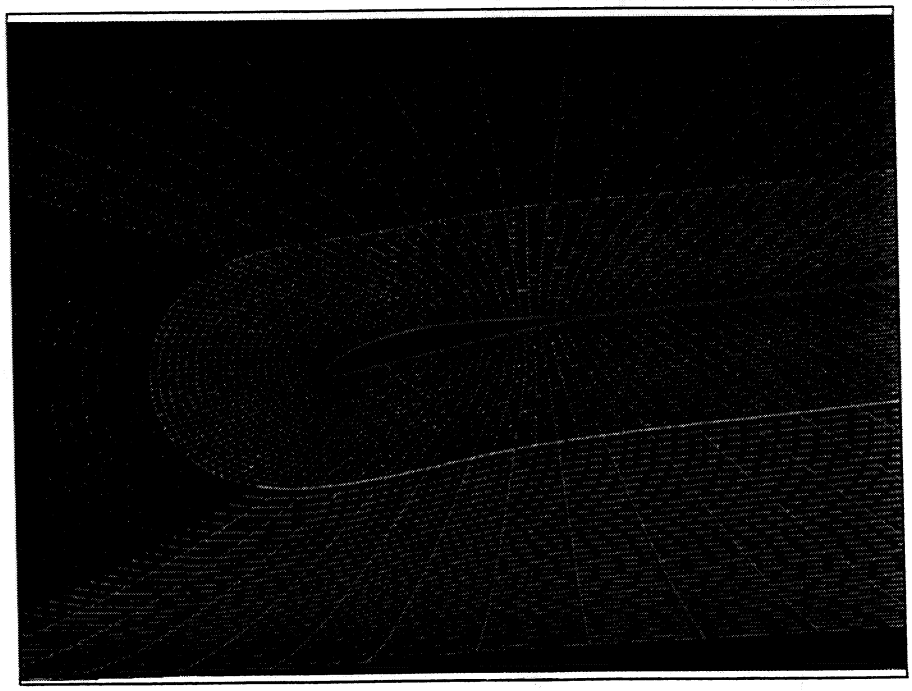

Figure 121: Magnified View of Blade Region

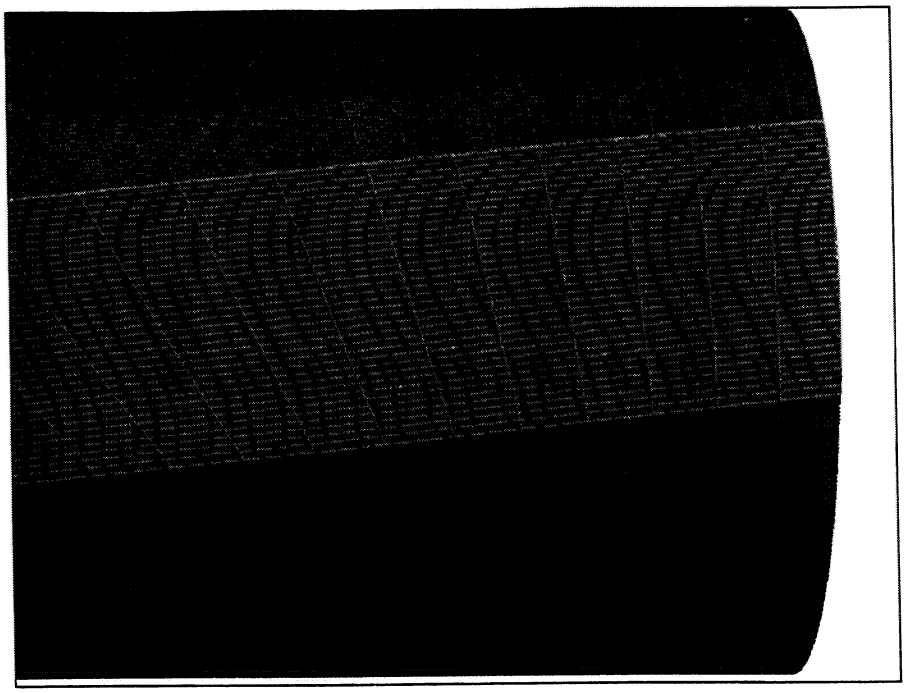

Figure 122: Magnified View of Trailing Edge Region

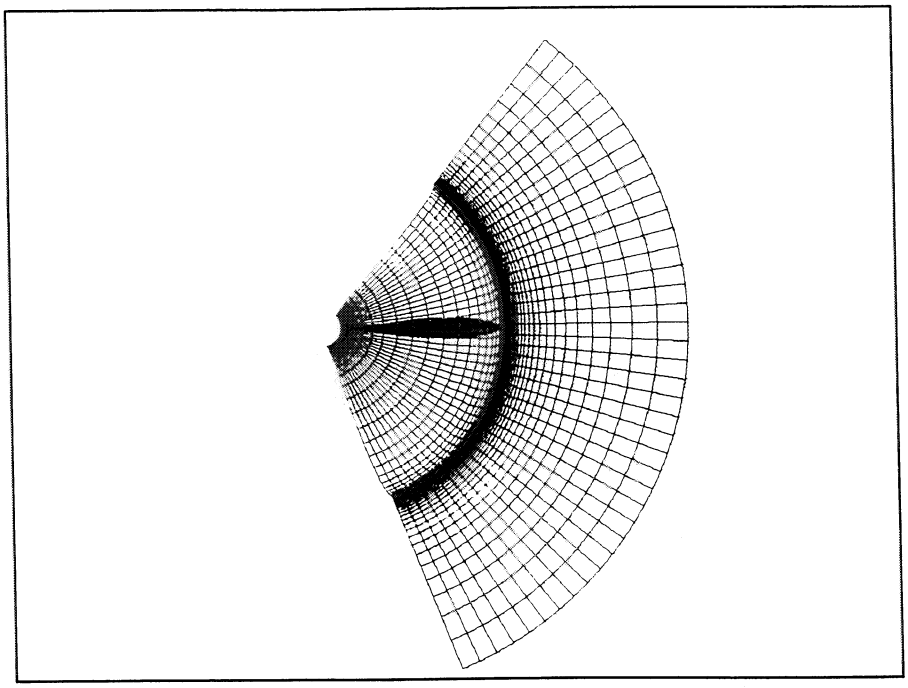

Figure 123: View of Computational Mesh Upstream and Above the Blade Tip—Forward Looking Aft

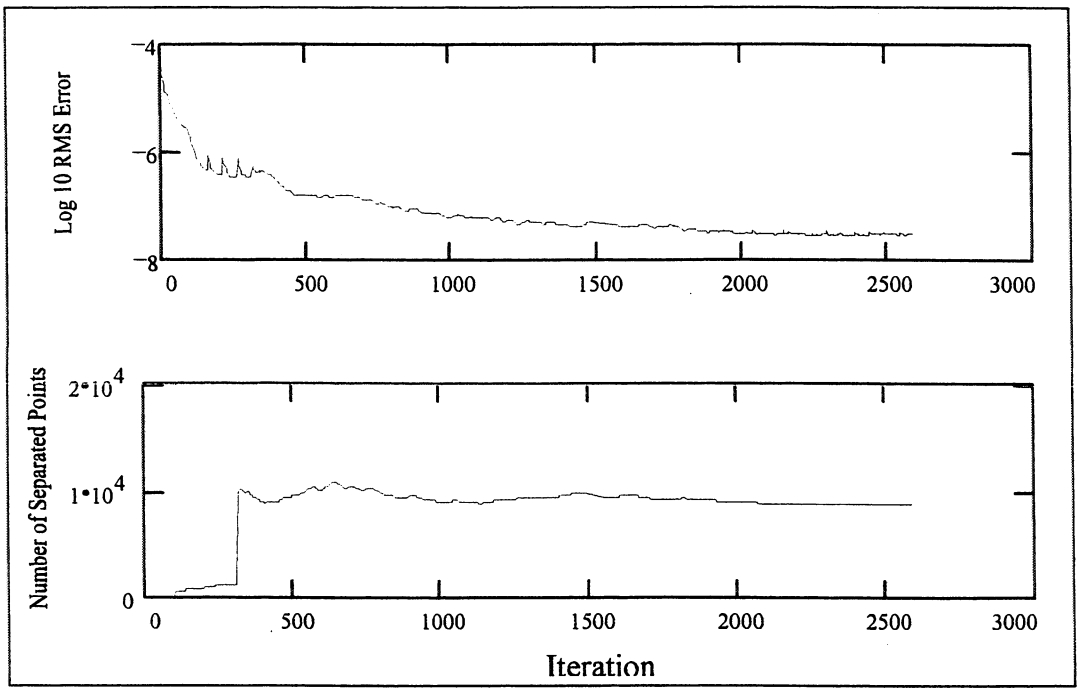

Figure 124: Convergence History for the Three-Dimensional ADPAC Calculation

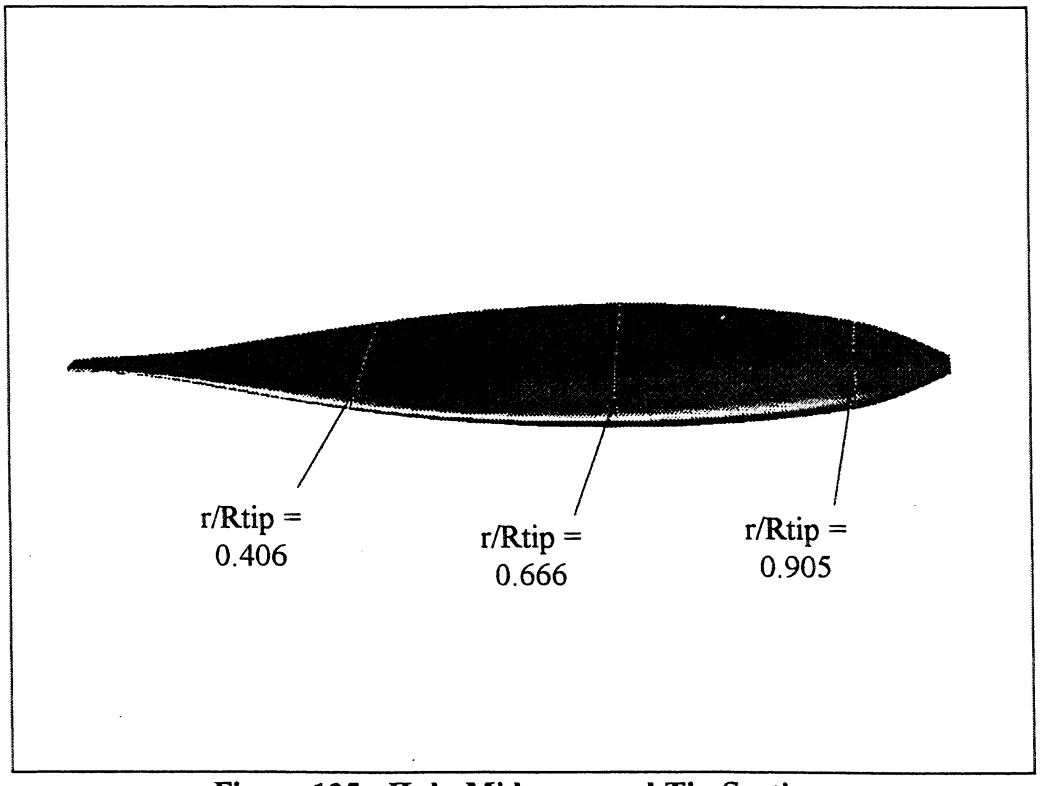

Figure 125: Hub, Midspan, and Tip Sections

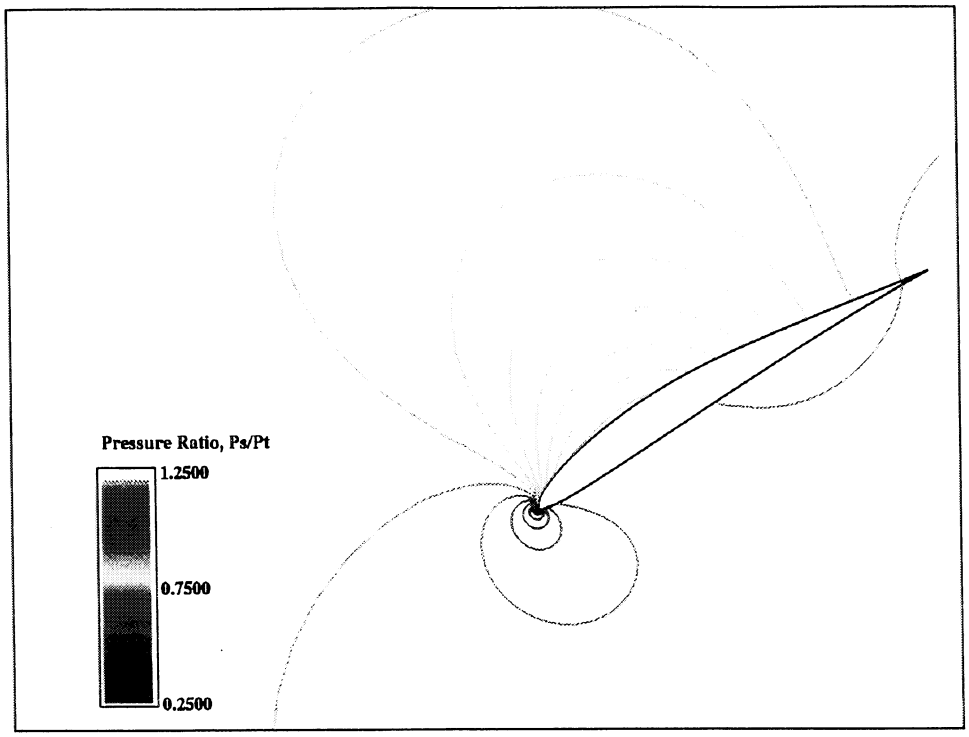

Figure 126: Pressure Ratio Contours for r/Rtip = 0.406

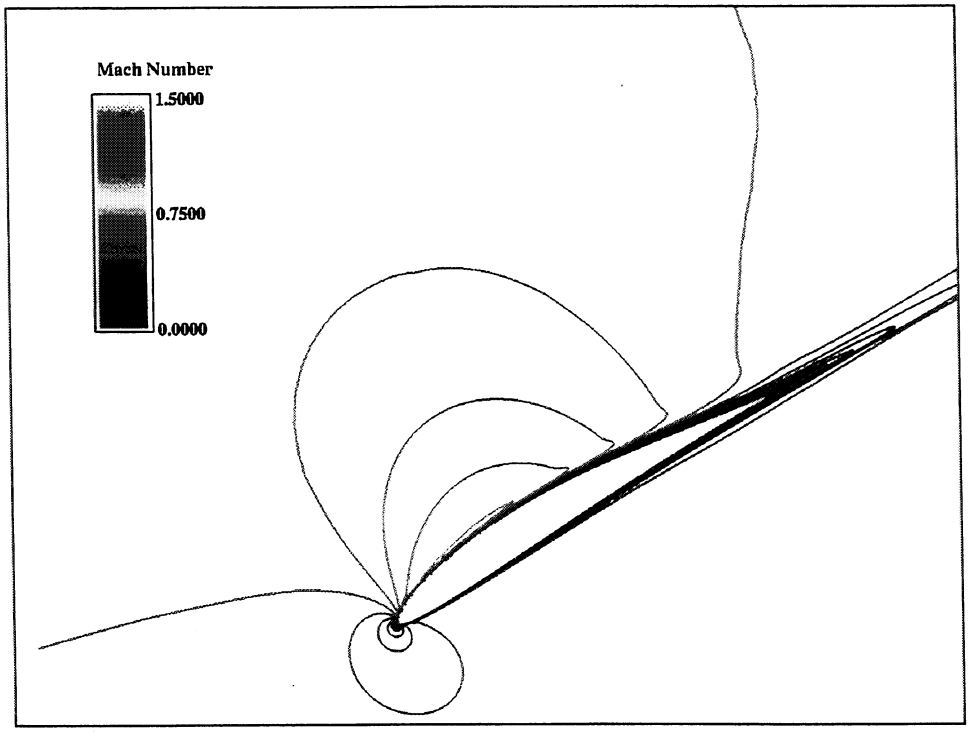

Figure 127: Mach Number Contours for r/Rtip = 0.0406

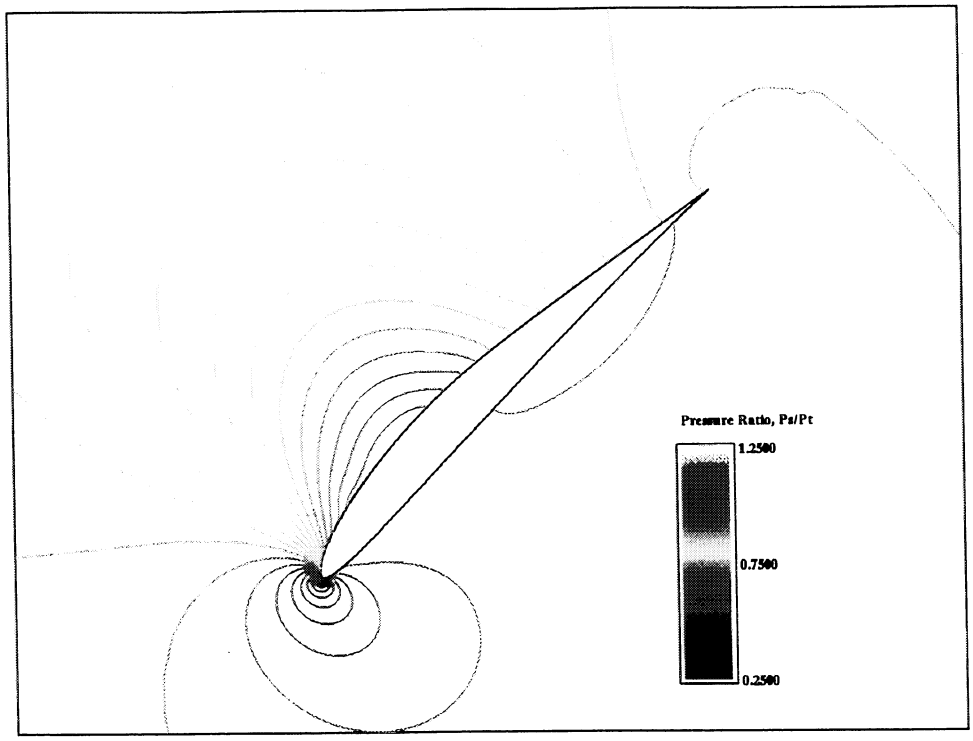

Figure 128: Pressure Ratio Contours for r/Rtip = 0.666

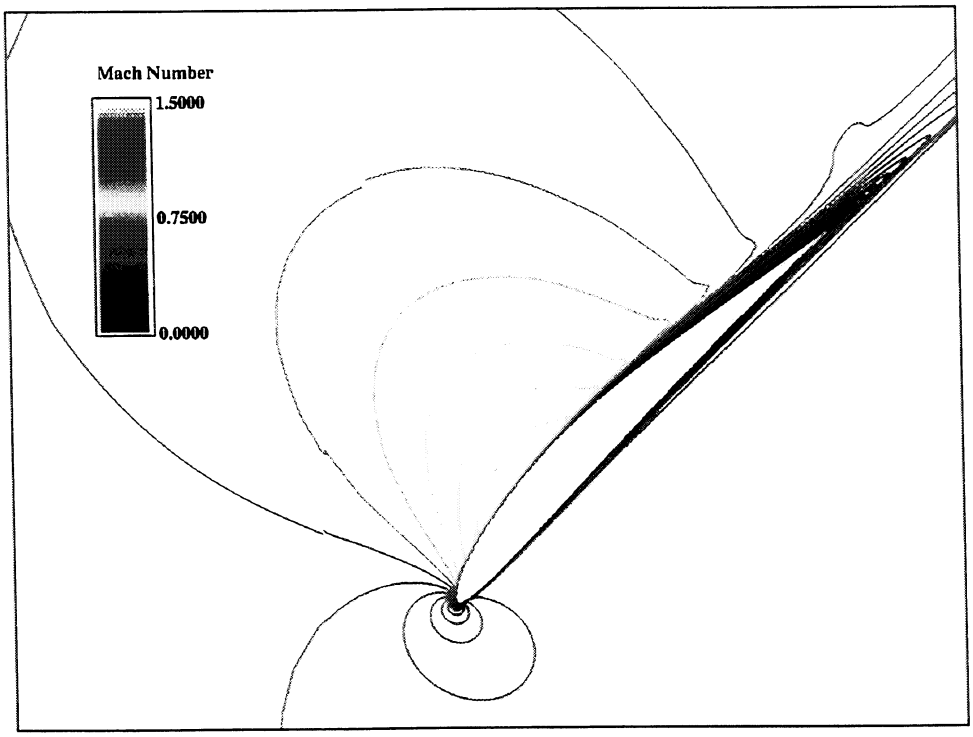

Figure 129: Mach Number Contours for r/Rtip = 0.666

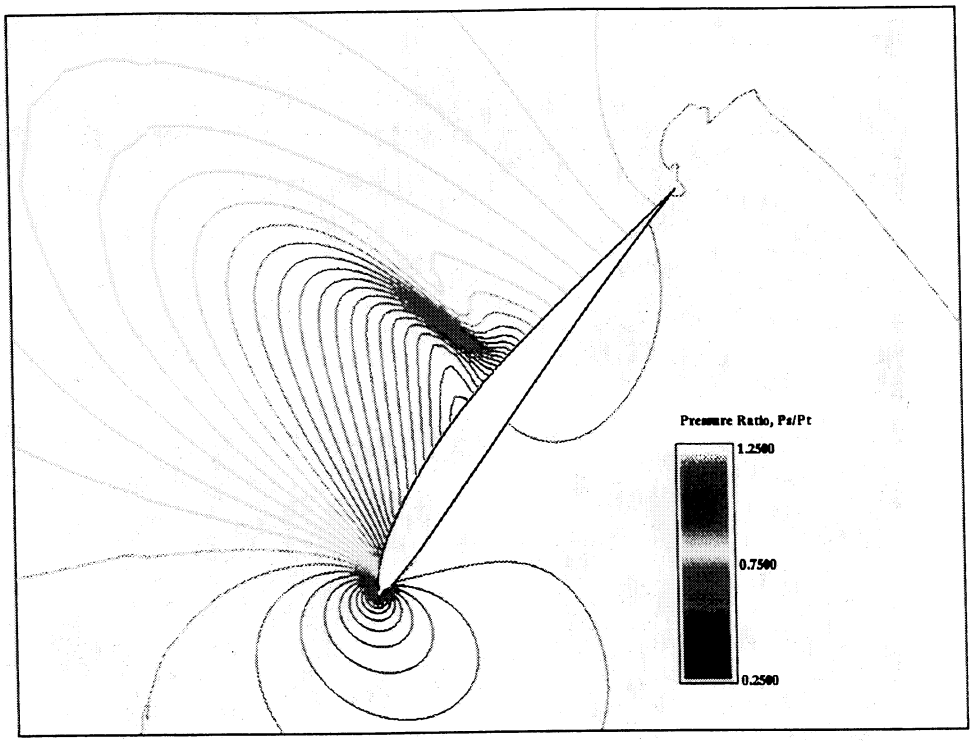

Figure 130: Pressure Ratio Contours for r/Rtip = 0.905

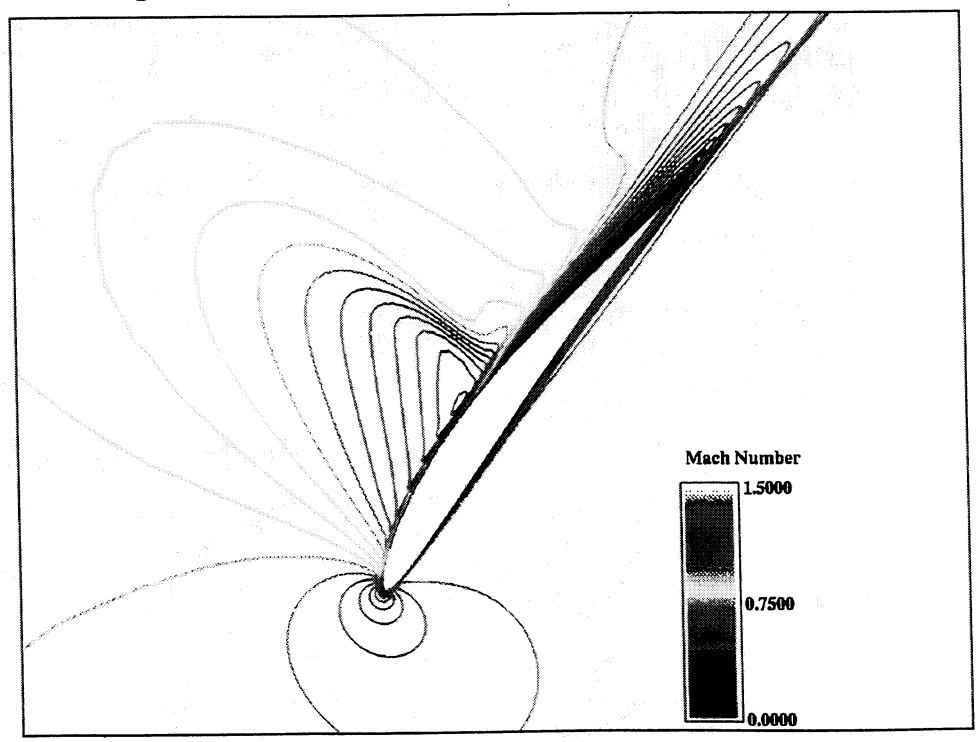

Figure 131: Mach Number Contours for r/Rip = 0.905

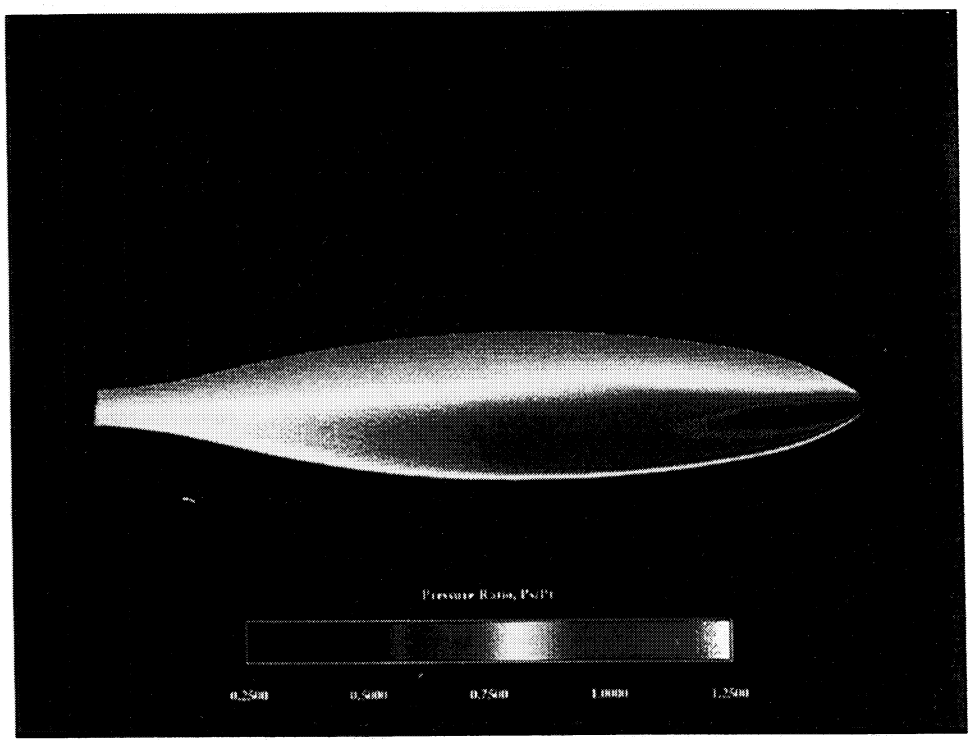

Figure 132: Suction Surface Pressure Distribution

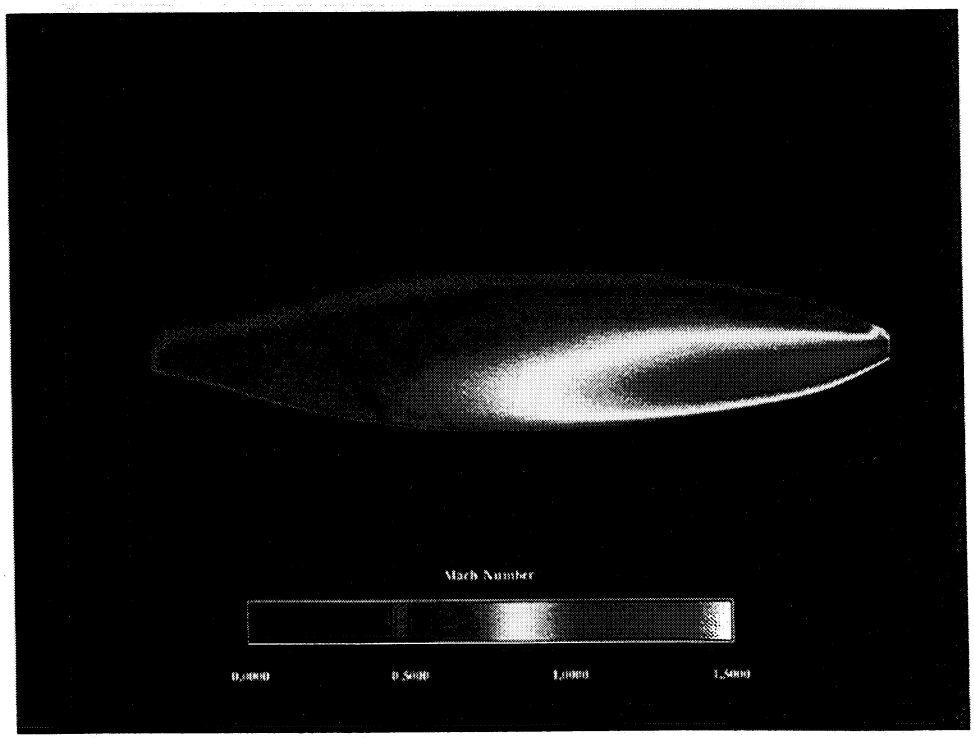

Figure 133: Mach Number Distribution Over the Suction Side of the Blade

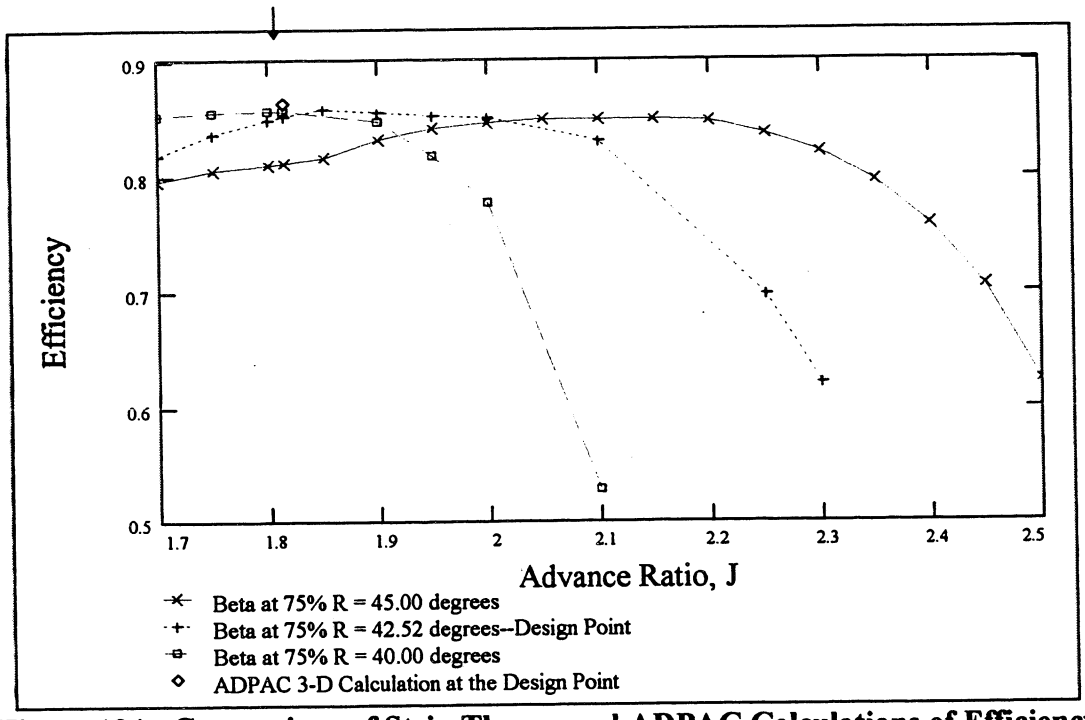

Figure 134: Comparison of Strip Theory and ADPAC Calculations of Efficiency

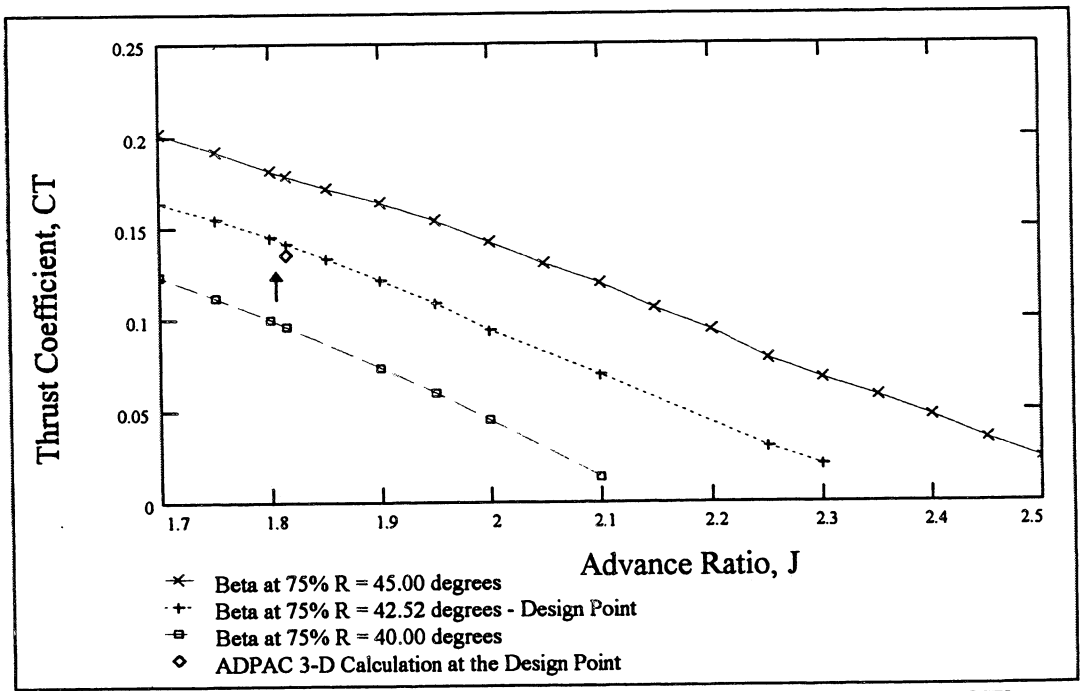

Figure 135: Comparison of Strip Theory and ADPAC Calculations of Thrust Coefficient

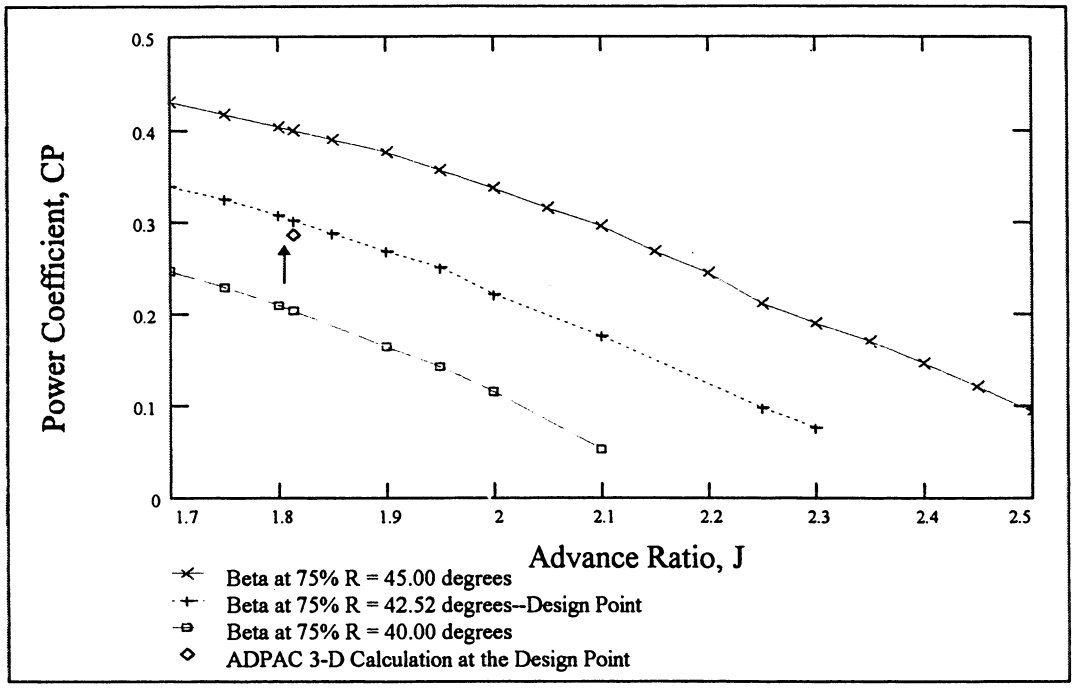

Figure 136: Comparison of Strip Theory and ADPAC Calculations of Power Coefficient

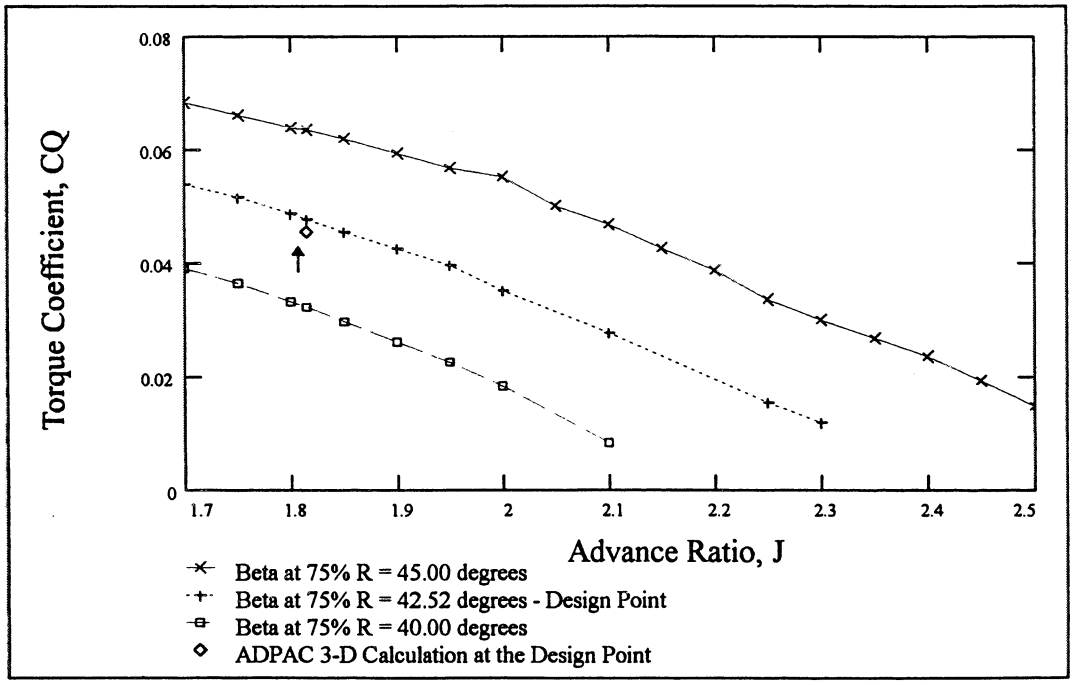

Figure 137: Comparison of Strip Theory and ADPAC Calculations of Torque Coefficient

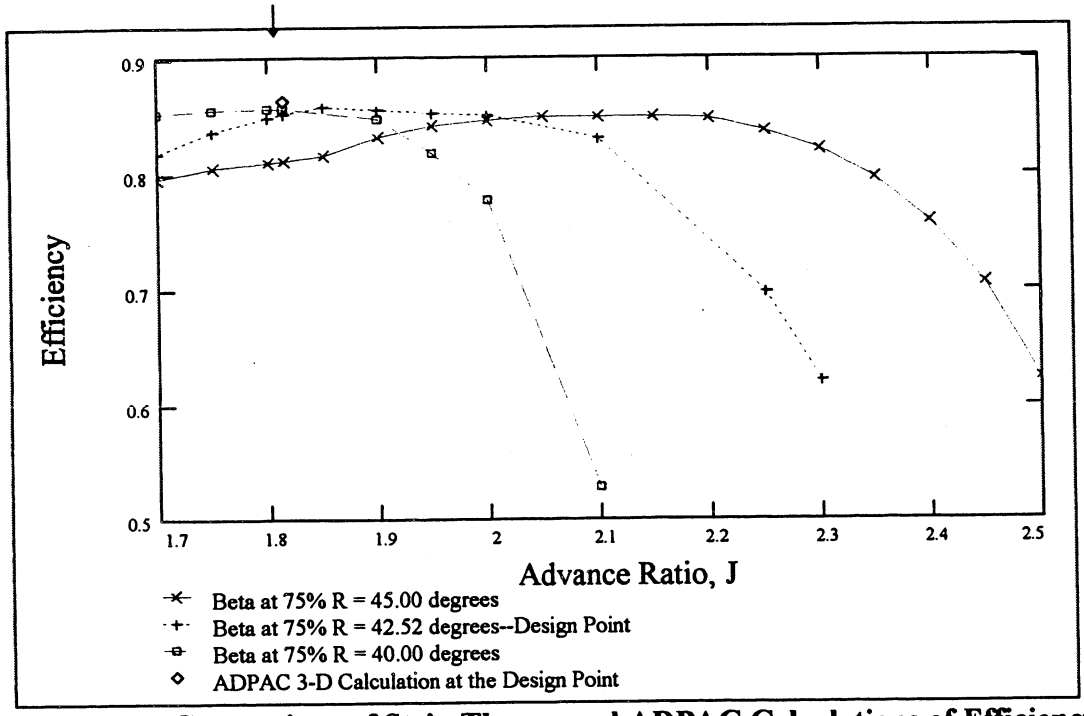

Figure 134: Comparison of Strip Theory and ADPAC Calculations of Efficiency

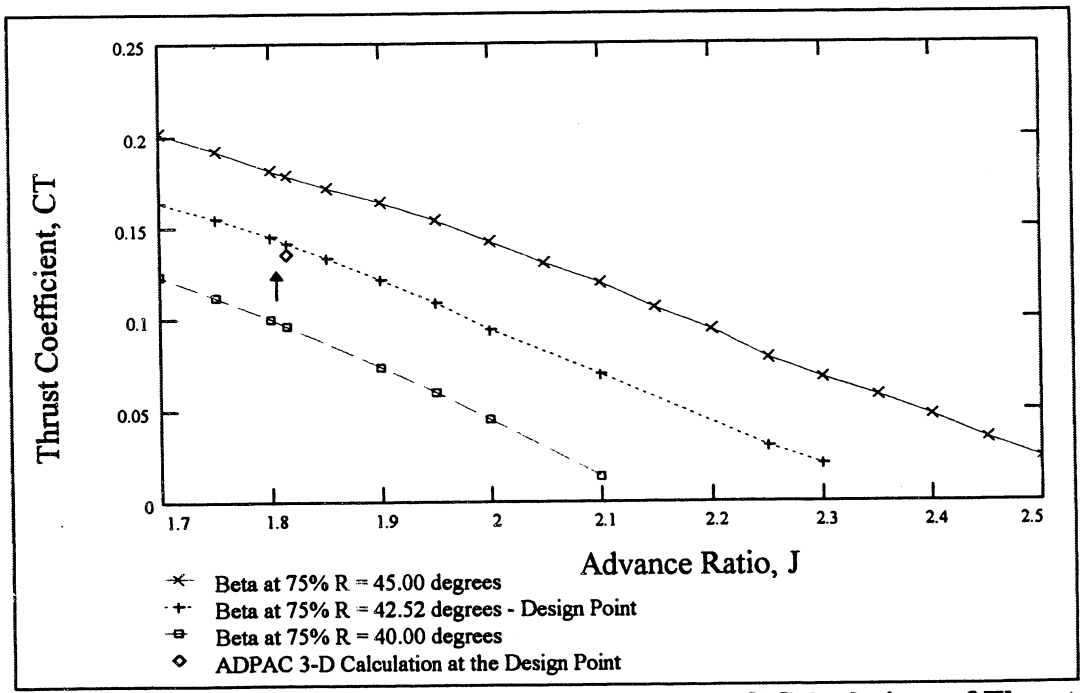

Figure 135: Comparison of Strip Theory and ADPAC Calculations of Thrust Coefficient

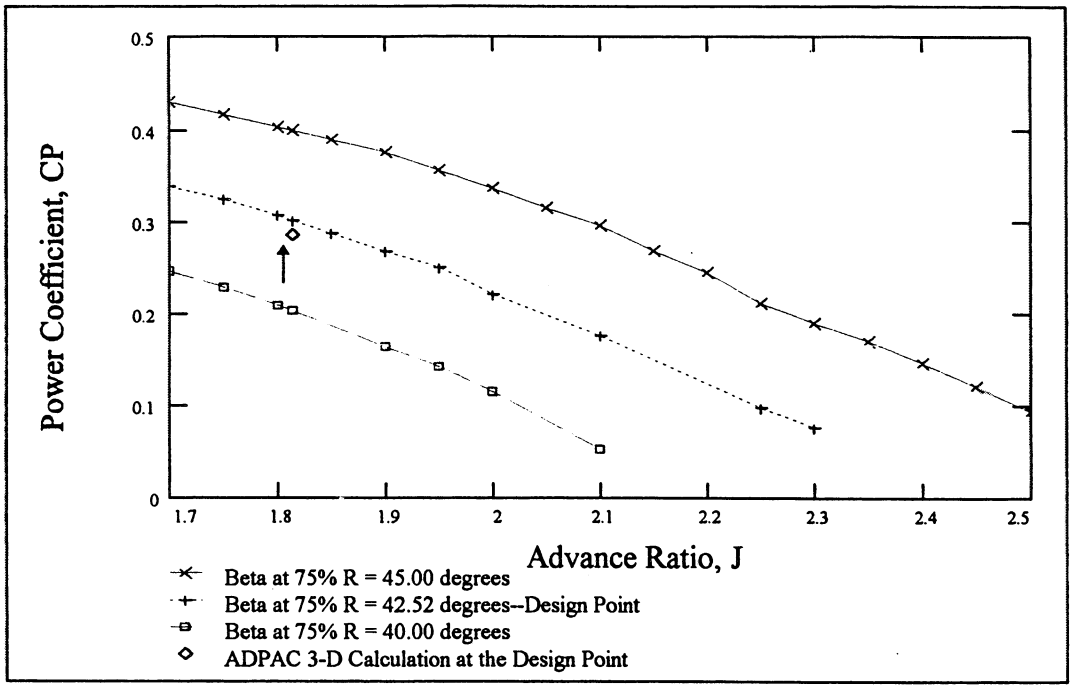

Figure 136: Comparison of Strip Theory and ADPAC Calculations of Power Coefficient

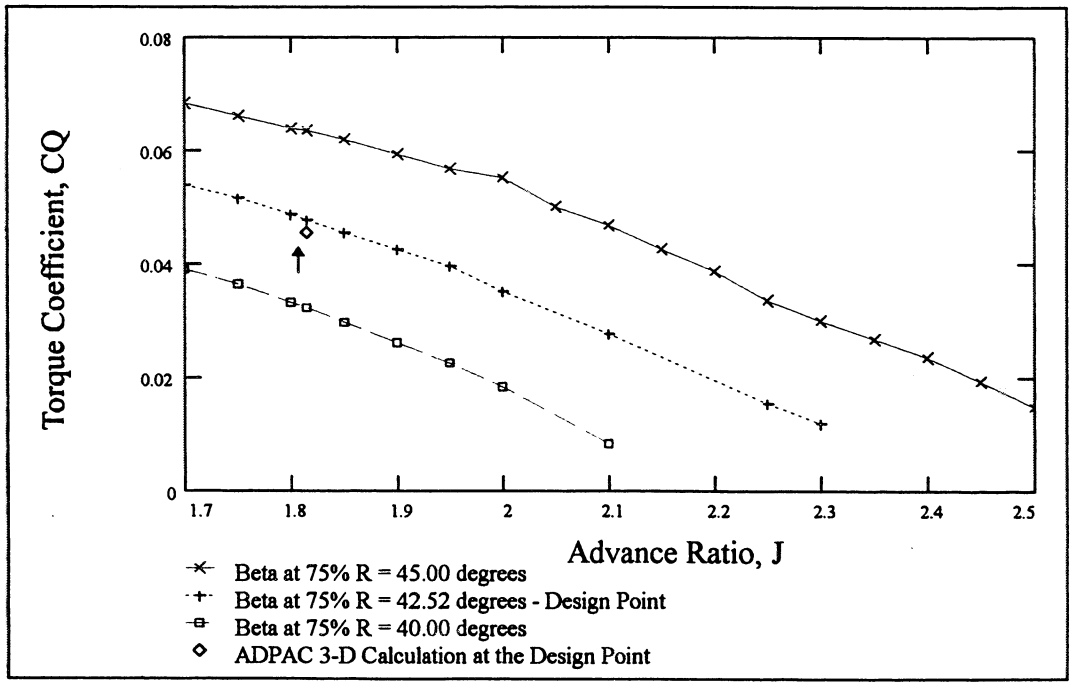

Figure 137: Comparison of Strip Theory and ADPAC Calculations of Torque Coefficient

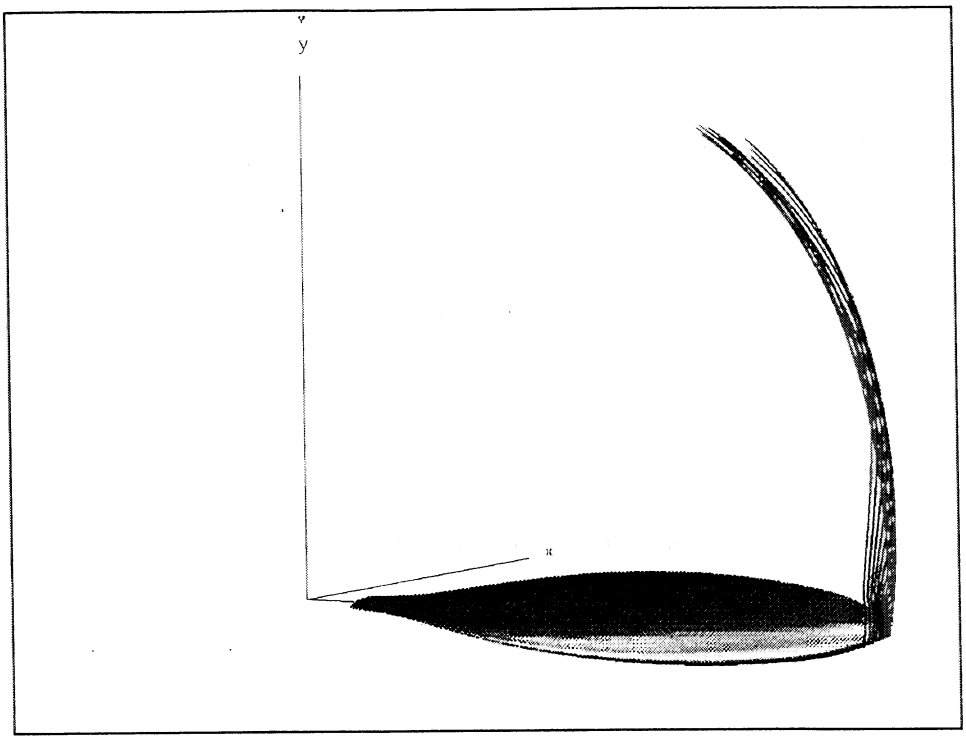

Figure 138: Tip Vortex Streamlines

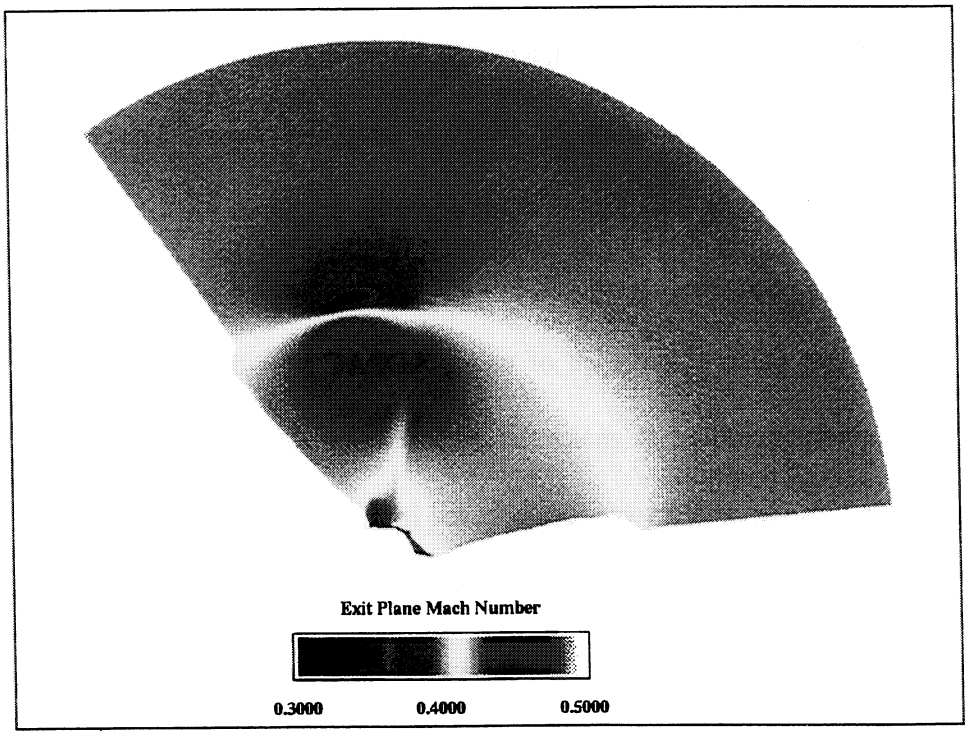

Figure 139: Pressure Distribution at the Exit Plane of the Computational Domain

CHAPTER 8--CONCLUSION

Comparison of the strip theory design and analysis results with those from ADPAC, a numerical Navier-Stokes analysis code, sheds light on the strengths and weaknesses of both techniques. Propeller efficiency predicted by ADPAC was within 1.5% of that calculated with the strip theory methods at the design point while ADPAC predictions of thrust, power, and torque coefficients were approximately 5% lower than the strip theory results.

The main advantage to the strip theory design and analysis methods is speed. Since design is an iterative process, the designer must be able to change conditions easily and determine the propeller's geometry quickly and Adkins' and Liebeck's procedures prove to be a useful tool. Results from strip theory analyses can be obtained quickly as well, a necessity when calculating performance at many off-design conditions in order to create a propeller map. Despite the simplifying assumptions made, reasonable accuracy was achieved with Adkins' and Liebeck's strip theory methods.

The main advantages of using ADPAC was the elimination of simplifying assumptions required to make the performance calculation and the visualization of results. Shocks and tip vortices ignored in the strip theory analysis were clearly seen in viewing the ADPAC results. However, the improvement in the analysis required a substantial amount of time to learn how to run the code, to create appropriate meshes, and to post-process the output files. This time is in addition to that required to

actually run the calculation. The three-dimensional mesh consumed a great amount of time since approximately 22 hours were needed to complete 100 iterations on a dedicated workstation with an R8000 processor.

In conclusion, the fusion of two dimensional strip theory design and analysis methods with ADPAC, a three-dimensional Navier-Stokes yielded a good first-generation propeller design for a vehicle capable of subsonic flight in Earth's stratosphere. Lift and drag coefficients for the Eppler 387 at low Reynolds number transonic conditions were generated with ADPAC since experimental results were unavailable for this regime. Examination of the three-dimensional results showed that the Eppler 387 was not a suitable airfoil for at least the tip sections of the propeller because of the shock waves seen on the suction surface of the relatively thick outboard sections. Improvements can be made to this design by combining two-dimensional airfoil ADPAC results for other airfoils into the strip theory design and analysis methods (if experimental data is unavailable), making a full three-dimensional prediction only after several design iterations are made.

REFERENCES

[1] ERAST Leadership Team. 1996. A Review of Remotely Piloted Aircraft (RPA) Technology Required for High Altitude Civil Sciences Missions. Washington, D.C.: NASA, Office of Aeronautics (Code R), Office of Mission to Planet Earth (Code Y). Photocopied.

[2] Adkins, C.N. and R.H. Liebeck. 1983. *Design of Optimum Propellers*. New York: American Instintue of Aeronautics and Astronautics. AIAA-83-0190.

[3] Mueller, T. J. 1985. *Low Reynolds Number Vehicles*. Neuilly-Sur-Seine, France: Advisory Group for Aerospace Research and Development. NTIS, AGARDograph No. 288.

[4] Pauley, L.L. and P. Moin and W.C. Reynolds. 1989. The Instability of Two-Dimensional Laminar Separation. In *Low Reynolds Number Aerodynamics: Proceedings of the Conference* in Notre Dame, Indiana. June 5-7, 1989 by Springer-Verlag, 82-92. New York: Springer-Verlag.

[5] McGhee, R.J. and B.J. Walker and B.F. Millard. 1988. *Experimental Results for the Eppler 387 Airfoil at Low Reynolds Numbers in the Langley Low-Turbulence Pressure Tunnel*. Washington, D.C. NASA TM-4062.

[6] Drela, M.1989. XFOIL: An Analysis and Desing System for Low Reynolds Number Airfoils. In *Low Reynolds Number Aerodynamics: Proceedings of the Conference* in Notre Dame, Indiana, June 5-7. 1989. By Springer-Verlag.1-12. New York: Springer-Verlag

[7] Drela, M. 1992. *Transonic Low-Reyonlds Number Airfoils*. Journal of Aircraft. Vol. 29 No. 6 (Nov.-Dec.): 1106-1113.

[8] Coiro, D.P. and C.deNicola. 1989. Prediction of Aerodynamic Performance of Airfoils in Low Reynolds Number Flows. *In Low Reynolds Number Aerodynamics: Proceedings of the Conference* in Notre Dame, Indiana. June 5-7, 1989. By Springer-Verlag. 13-23, New York: Springer-Verlag.

[9] Hall, E.J. and D.A. Top and R.A. Delaney. *Task 7-ADPAC Users Manual*.Cleveland: NASA Lewis Research Center, NASA CR-195472.

[10] Schlichting, H. 1960. *Boundary Layer Theory*. New York: McGraw-Hill.

[11] Glauert, H. 1926. *The Elements of Aerofoil and Airscrew Theory*, Cambridge: The University Press.

[12] McCormick, B.W. 1979. *Aerodynamics, Aeronautics, and Flight Mechanics, New York*: John Wiley and Sons.

[13] Anderson, J.D. 1989. *Introduction to Flight*. New York: McGraw-Hill Book Company.

[14] Chima, R.V. 1990. *TCGRID*. Cleveland: NASA Lewis Research Center.

REPORT DOCUMENTATION PAGE

Form Approved
OMB No. 0704-0188

1. AGENCY USE ONLY (*Leave blank*)	2. REPORT DATE	3. REPORT TYPE AND DATES COVERED
	February 1998	Technical Memorandum

4. TITLE AND SUBTITLE

Design and Performance Calculations of a Propeller for Very High Altitude Flight

5. FUNDING NUMBERS

WU–529–10–13–00

6. AUTHOR(S)

L. Danielle Koch

7. PERFORMING ORGANIZATION NAME(S) AND ADDRESS(ES)

National Aeronautics and Space Administration
Lewis Research Center
Cleveland, Ohio 44135–3191

8. PERFORMING ORGANIZATION REPORT NUMBER

E–11102

9. SPONSORING/MONITORING AGENCY NAME(S) AND ADDRESS(ES)

National Aeronautics and Space Administration
Washington, DC 20546–0001

10. SPONSORING/MONITORING AGENCY REPORT NUMBER

NASA TM—1998-206637

11. SUPPLEMENTARY NOTES

This report was submitted as a thesis in partial fulfillment of the requirements for the degree of Masters of Science in Engineering to Case Western Reserve University, Cleveland, Ohio, January 1998. Responsible person, L. Danielle Koch, organization code 7565, (216) 433–5656.

12a. DISTRIBUTION/AVAILABILITY STATEMENT

Unclassified - Unlimited
Subject Categories: 02 and 07 Distribution: Nonstandard

This publication is available from the NASA Center for AeroSpace Information, (301) 621–0390.

12b. DISTRIBUTION CODE

13. ABSTRACT ***(Maximum 200 words)***

Reported here is a design study of a propeller for a vehicle capable of subsonic flight in Earth's stratosphere. All propellers presented were required to absorb 63.4 kW (85 hp) at 25.9 km (85,000 ft) while aircraft cruise velocity was maintained at Mach 0.40. To produce the final design, classic momentum and blade-element theories were combined with two and three-dimensional results from the Advanced Ducted Propfan Analysis Code (ADPAC), a numerical Navier-Stokes analysis code. The Eppler 387 airfoil was used for each of the constant section propeller designs compared. Experimental data from the Langley Low-Turbulence Pressure Tunnel was used in the strip theory design and analysis programs written. The experimental data was also used to validate ADPAC at a Reynolds numbers of 60,000 and a Mach number of 0.20. Experimental and calculated surface pressure coefficients are compared for a range of angles of attack. Since low Reynolds number transonic experimental data was unavailable, ADPAC was used to generate two-dimensional section performance predictions for Reynolds numbers of 60,000 and 100,000 and Mach numbers ranging from 0.45 to 0.75. Surface pressure coefficients are presented for selected angles of attack, in addition to the variation of lift and drag coefficients at each flow condition. A three-dimensional model of the final design was made which ADPAC used to calculated propeller performance. ADPAC performance predictions were compared with strip-theory calculations at design point. Propeller efficiency predicted by ADPAC was within 1.5% of that calculated by strip theory methods, although ADPAC predictions of thrust, power, and torque coefficients were approximately 5% lower than the strip theory results. Simplifying assumptions made in the strip theory account for the differences seen.

14. SUBJECT TERMS	15. NUMBER OF PAGES
Propeller; High-altitude; Low Reynolds number aerodynamics; ADPAC	130
	16. PRICE CODE: A07

17. SECURITY CLASSIFICATION OF REPORT	18. SECURITY CLASSIFICATION OF THIS PAGE	19. SECURITY CLASSIFICATION OF ABSTRACT	20. LIMITATION OF ABSTRACT
Unclassified	Unclassified	Unclassified	